SAND76-0131

Unlimited Release

UC-60

Wind Tunnel Performance Data for Two- and Three-Bucket Savonius Rotors

Ben F. Blackwell, Robert E. Sheldahl, Louis V. Feltz

Prepared by Sandia Laboratories, Albuquerque, New Mexico 87115
and Livermore, California 94550 for the United States Energy Research
and Development Administration under Contract AT(29–1)-789

Printed July 1977

Issued by Sandia Laboratories, operated for the United States Energy Research & Development Administration by Sandia Corporation.

NOTICE

Printed in the United States of America

Available from
National Technical Information Service
U. S. Department of Commerce
5285 Port Royal Road
Springfield, VA 22161
Price: Printed Copy $5.50 ; Microfiche $3.00

SAND76-0131
Unlimited Release
Printed July 1977

Distribution
Category UC-60

WIND TUNNEL PERFORMANCE DATA FOR TWO- AND THREE-BUCKET SAVONIUS ROTORS

Ben F. Blackwell
Robert E. Sheldahl
Aerothermodynamics Division, 1333

Louis V. Feltz
Mechanical Design Division, 1324
Sandia Laboratories
Albuquerque, NM 87115

ABSTRACT

Fifteen configurations of a Savonius rotor wind turbine were tested in the Vought Corporation Systems Division 4.9- x 6.1-m Low Speed Wind Tunnel to determine aerodynamic performance. The range of values of the varied parameters was

Number of Buckets	2 and 3
Nominal Freestream Velocity	7 and 14 m/s
Reynolds Number per Metre	4.32×10^5 and 8.67×10^5
Rotor Height	1 and 1.5 m
Rotor Diameter (nominal)	1 m
Bucket Overlap	0.0-0.1 m

The measured test variables were torque, rotational speed, and tunnel conditions. The data presented are in the form of power and torque coefficients as a function of speed ratio (or angular position for static starting torques). It is concluded that increasing Reynolds number and/or aspect ratio improves performance. The recommended configuration consists of two sets of two-bucket rotors, rotated 90° apart, with each rotor having a dimensionless gap width of 0.1-0.15.

ACKNOWLEDGMENTS

D. F. McNeill (Division 1324) handled the hardware design and procurement. David Powers (Division 1334) and Donald MacKenzie (1334) were instrumental in recording and reducing data. Melvin R. Baer (1333) assisted with several aspects of the data analysis. Bob White and the Low Speed Wind Tunnel staff of the Vought Corporation provided exceptional cooperation in conducting these tests.

CONTENTS

FIGURES

FIGURES (cont)

FIGURES (cont)

FIGURES (cont)

NOMENCLATURE

A_s		turbine swept area
C_P		power coefficient, $\frac{Q\Omega}{q_\infty V_\infty A_s}$
C_P^*	$=$	$\frac{Q\Omega}{q_\infty V_\infty (4rH)}$
C_Q		torque coefficient, $\frac{Q}{q_\infty R A_s}$
C_Q^*	$=$	$\frac{Q}{q_\infty (4rH)(2r)}$
d		bucket diameter, 2 r
H		rotor height
N		number of buckets
P_∞		freestream static pressure
P_{bar}		barometric pressure
P_g		gage pressure in tunnel
Q		turbine torque
Q_f		friction (tare) torque
q_∞		freestream dynamic pressure, $1/2\rho_\infty V_\infty^2$
R		rotor radius of rotation (see Figures 5 and 6)
Re_∞		Reynolds number per unit length, $\frac{\rho_\infty V_\infty}{\mu_\infty}$
r		bucket radius (see Figures 5 and 6)
s		bucket gap width (see Figures 5 and 6)
s/d		gap width ratio

NOMENCLATURE (cont)

T_∞	freestream temperature
V_∞	freestream velocity, $V_{\infty_u} (1 + \epsilon)$
X_∞	turbine speed ratio, $\frac{R\Omega}{V_\infty}$
X_∞^*	$= \frac{2r\Omega}{V_\infty}$
δ	uncertainty
ϵ	wind tunnel blockage factor
θ	bucket angular position (see Figures 5 and 6)
μ_∞	freestream viscosity
ρ_∞	freestream density
Ω	turbine rotational speed

Subscripts

u	uncorrected for blockage

I. INTRODUCTION

The Savonius rotor is a novel fluid mechanical device that has been studied by numerous investigators since the 1920s. Applications for the Savonius rotor have included pumping water, driving an electrical generator, providing ventilation (attic and vehicular applications), and providing water agitation to keep stock ponds ice-free during the winter. It is also commonly used as an ocean current meter.

Savonius rotors generally cannot compete with either a propeller-type or a Darrieus wind turbine on an aerodynamic performance basis. However, because the technology required to fabricate a Savonius rotor is considerably less than that required for more sophisticated types of wind turbines, Savonius rotors may find more applications in developing countries as well as in do-it-yourself projects.

Another application for the Savonius rotor is as a passive starter system for the Darrieus rotor. The Darrieus rotor is not self-starting; however, the Savonius rotor has very good starting torque characteristics. It is this application that motivated the present experimental investigation of the Savonius rotor performance characteristics.

Numerous experimental studies of the Savonius rotor have been reported in the literature.[1-15] A number of the references cited included wind tunnel tests of the Savonius rotor. However, most of them had severe tunnel blockage problems: the model occupied a significant fraction of the tunnel cross section. The scarcity and questionable reliability of the available test data gave rise to an independent Savonius rotor wind tunnel test program.[16, 17] The test program was conducted during May 1975 at the Vought Systems Division Low Speed Wind Tunnel.[18] The varying geometrical parameters consisted of:

Number of Buckets (N):	2, 3
Gap Spacing (s/d):	0.0, 0.1, 0.15, 0.20
Rotor Height (H):	1, 1.5 m

The diameter of each bucket was 0.5 m. The torque characteristics as a function of rotational speed (including zero rotational speed) were determined for each geometrical configuration. Each configuration was tested at nominal freestream velocities of 7 m/s and/or 14 m/s, corresponding to nominal Re/m of 4.32×10^5 and 8.67×10^5, respectively.

II. TEST MODELS AND INSTRUMENTATION

Representative three- and two-bucket test models are shown in Figures 1 and 2, respectively. The rotor consists of the rotating components (buckets and endplates) held by bearings in the upper collar and in the lower support structure. Four outrigger trusses are attached to the upper collar. Guy cables extend from the outrigger trusses to the wind tunnel floor. The lower support structure is mounted to the I-beams* shown on the floor of the tunnel.

A schematic of the model, instrumentation, load, and control system is shown in Figure 3. The precision torque meter, rotational speed transducer, indexing mechanism, and sliding vane air motor are shown in greater detail in Figure 4.

The rotor buckets and endplates were fabricated from aluminum alloy, Type 6061 T6. Each pair of endplates accommodated several bucket configurations. The rotor bucket segments were attached to the endplates with machine screws. The testing sequence was such that a rotor configuration (buckets and endplates) could be assembled while the previous configuration was being tested in the tunnel. Model changes in the tunnel required about a half-hour.

The index plate, shown in Figure 4, is affixed to the lower shaft extension of the torque transducer. This plate included detents for sequential rotational positioning of the rotor for obtaining the static, or nonrotating, torque as a function of bucket position relative to the flow. A pneumatically actuated piston plunger engaged the index plate at the desired rotational position. The indexer could be operated both from the turbine location and remotely from the control room. Only 180° of indexing was required, as this range covered a complete cycle of the two-bucket configurations.

---

*These heavy I-beams are required for locating the rotor in the center of the test section while avoiding damage to the moving ground plane apparatus located on the tunnel floor at this location.

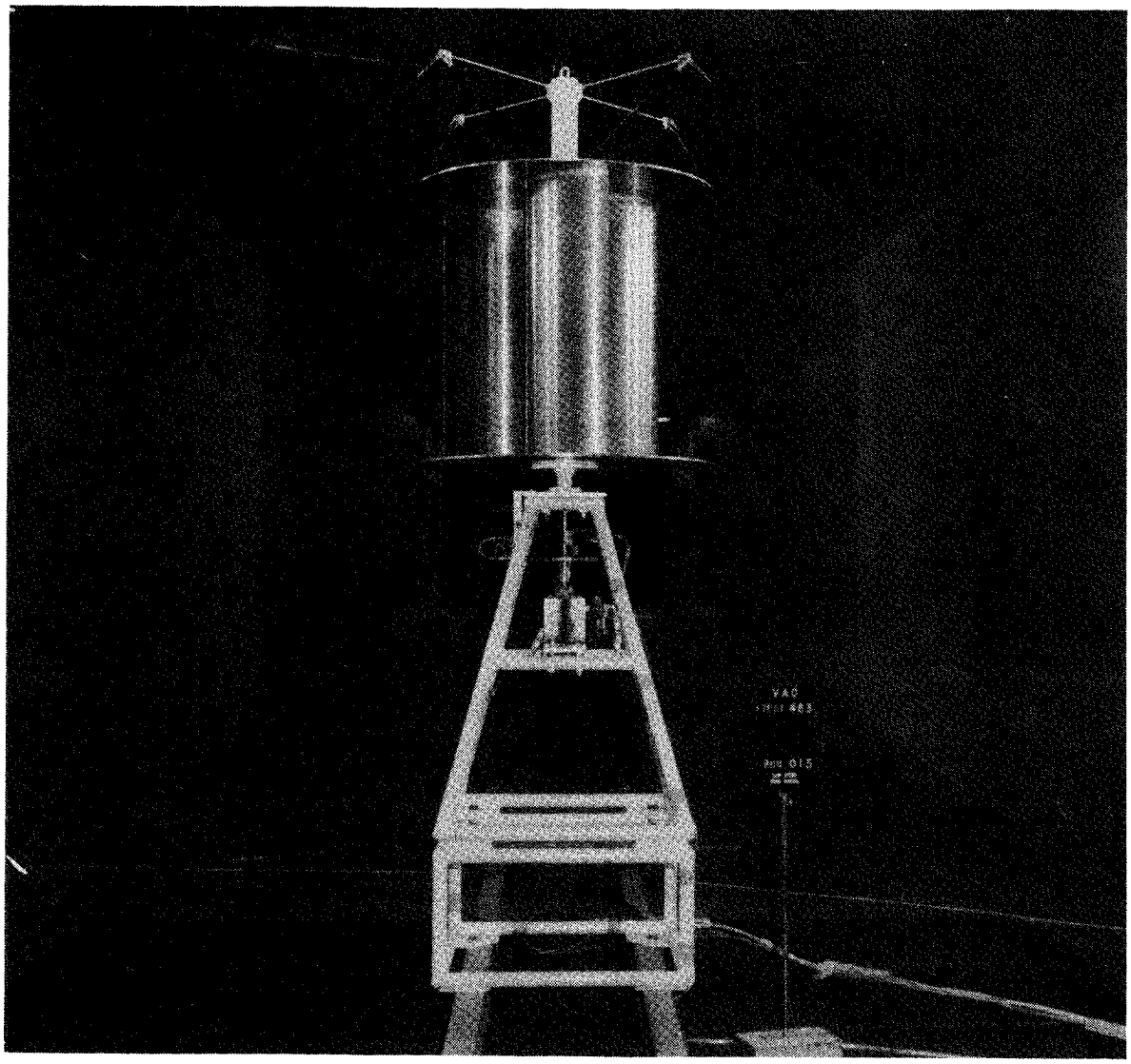

Figure 1. Savonius rotor wind turbine model (1-metre) in the Vought Corporation Low Speed Wind Tunnel (looking downstream).

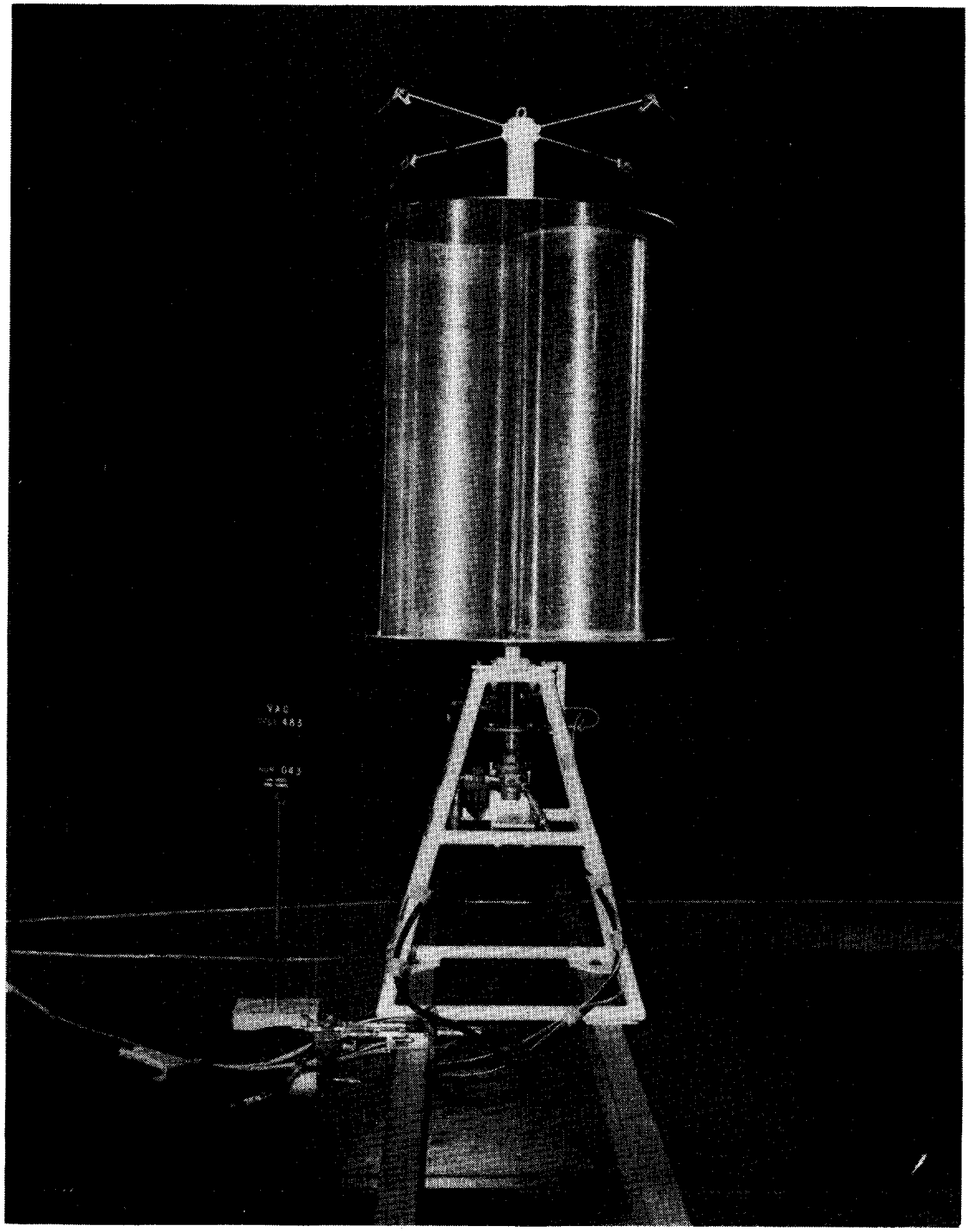

Figure 2. Savonius rotor wind turbine model (1-1/2-metre) in the Vought Corporation Low Speed Wind Tunnel (looking upstream).

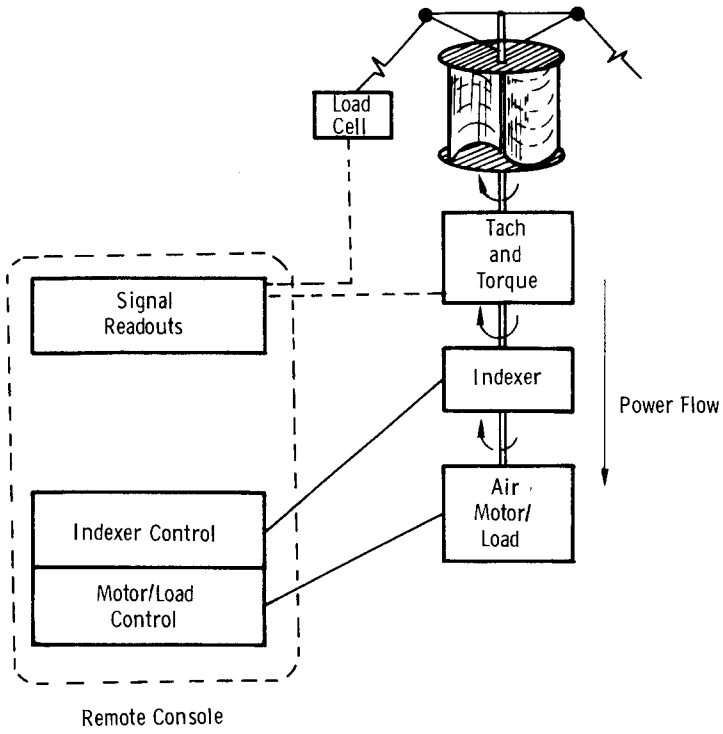

Figure 3. Schematic of the Savonius rotor/instrumentation load system.

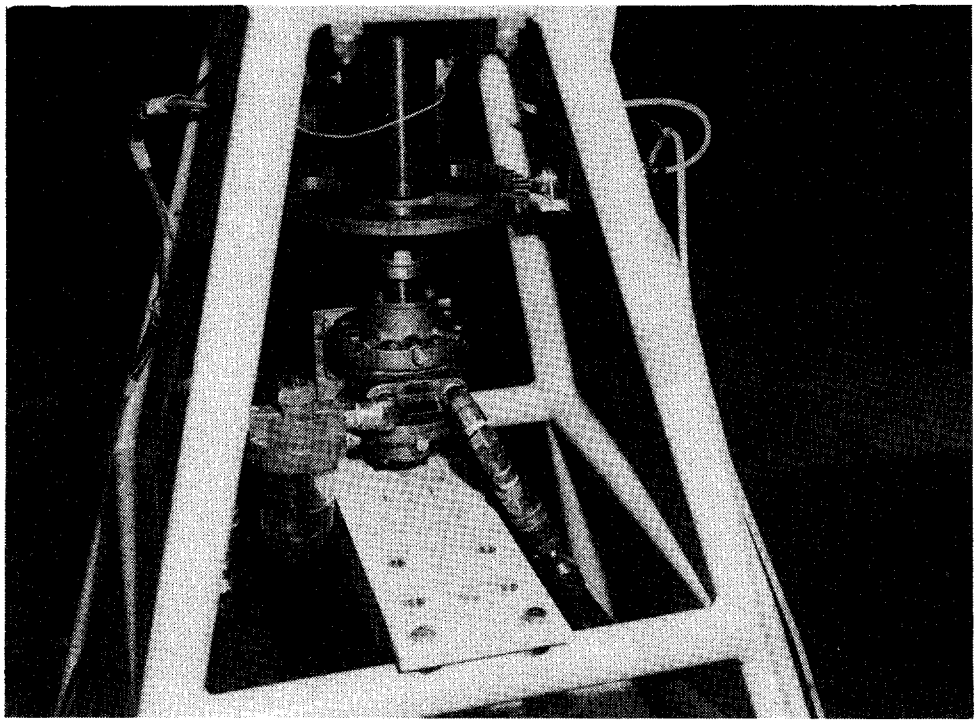

Figure 4. Savonius rotor stand showing the torque and rotational speed transducer, indexer, and air motor.

The bearings for the turbine included one double-row self-aligning ball bearing at the lower location and a set of two single-row radial-contact ball bearings in the upper collar. Because of the importance of precise determination of torques, bearing selection and loading are critical. Turbine torque and rotational speed were measured through a LeBow Torque Sensor Model 1404-200* and its associated signal conditioning equipment. This device incorporates a two-channel (from strain gage bridge legs) rotary transformer to extract the bridge signal from the rotating shaft without mechanical contact. The bridge signal is indicative of the torque, which is proportional to the shaft windup. The device is closely compensated for temperature variation and is advertised as having a total nonlinearity of only ±0. 1 percent of full scale.

The "full scale" recommended torque of the device selected was 200 in-lbf but, because overloading is allowed, the transducer was calibrated to 300 in-lbf. The alternate approach of selecting a transducer rated at an initially higher "full scale" (the next increment was 500 in-lbf) would have seriously degraded the torque resolution in the lower ranges, particularly in the determination of the tare torques of the turbine. The transducer was shaft mounted between the turbine and the load, and its housing was restrained from rotating by a strap attached to the lower structure. The transducer performed exceptionally well, even in the "overrated" application, and except for a shortcoming in mechanically protecting a transformer component, the entire system design is considered to be superior for this application.

The turbine load was a Gast Model 8 AM Air Motor.† This device, which is a radially sliding vane motor, includes eight vanes (in contrast to the usual four for this model). This was required to achieve the degree of load control desired. The device was operated both as a motor and as a compressor by adjusting input and/or output flow or pressure. These adjustments were made remotely in the wind tunnel control room. Note from Figure 2 that the air motor was mounted with the rotation axis vertical. This orientation required special lubrication considerations. Air line lubricators were supplied to both ports of the vane motor. One of these is visible to the immediate lower left of the motor in Figure 4. For extended operation, it is required that a very large quantity of moderate pressure air (100 psi) is available for this device when it is operated at rated capacity.

---

*LeBow Associates, 1728 Maple Lawn Road, Troy, Michigan 48084.

†Available from Gast Manufacturing Corp., P.O. Box 9, Benton Harbor, Michigan 49022.

The lower support structure consisted of several modular components so that a selected combination would position either the 1.0- or 1.5-m-high rotors at the wind tunnel centerline. The tiedown cables included strain gage load cells so that the bearing loads produced by the cable tensions would be consistent from one run to the next.

A schematic of the bucket orientation for the two-bucket configuration is shown in Figure 5. The buckets, which were hemicircular, contained a full 180° arc with a radius, r, of 0.25 m. The gap width, s, separating the inside edges of the buckets was one of the variables for the tests. The dimensionless gap width, s/d, where d is the bucket diameter, was varied from 0.0 to 0.20. The radius of rotation, R, was measured from the axis of rotation to the outer edge of the buckets. The bucket height, a second variable, was either 1 or 1.5 m.

The buckets for all the three-bucket rotors (Figure 6), with the exception of Configuration 21, were constructed with a 150° arc and a radius, r, of 0.25 m. The buckets for Configuration 21 were the same as those used for the two-bucket configurations. For practical design considerations, the arc of the buckets was shortened by 20° on the outer edge and 10° on the inner edge.* The gap distance is defined as for a two-bucket configuration; i.e., the gap distance, s/2, is the distance from the axis of rotation to the end of the bucket arc, assuming the arc is carried to the full hemicircle (Figure 6).

*If a three-bucket Savonius configuration is to be used to start a three-blade Darrieus configuration, there will be a mechanical interference between the Darrieus and Savonius blades unless the arc is shortened.

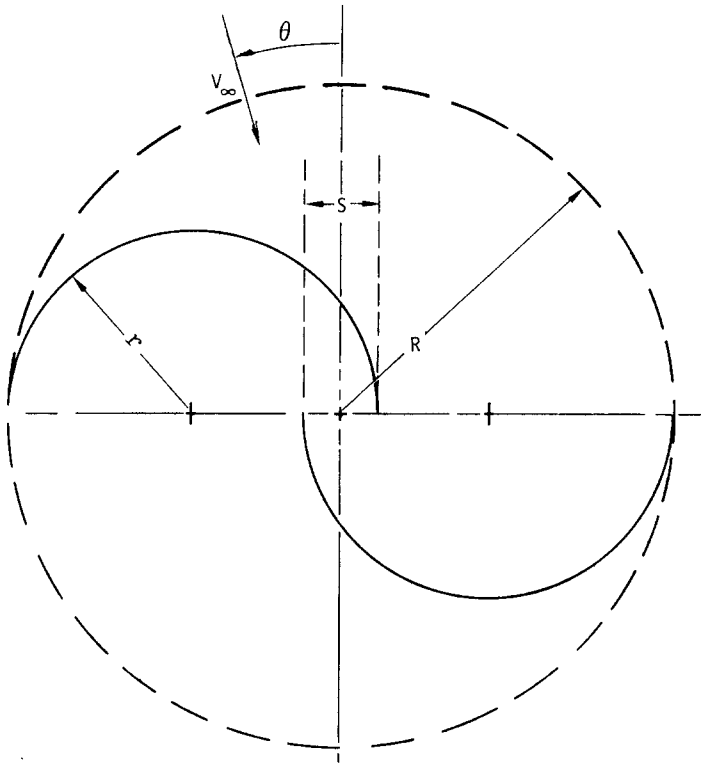

Figure 5. Schematic of the two-bucket Savonius rotor with 180° buckets.

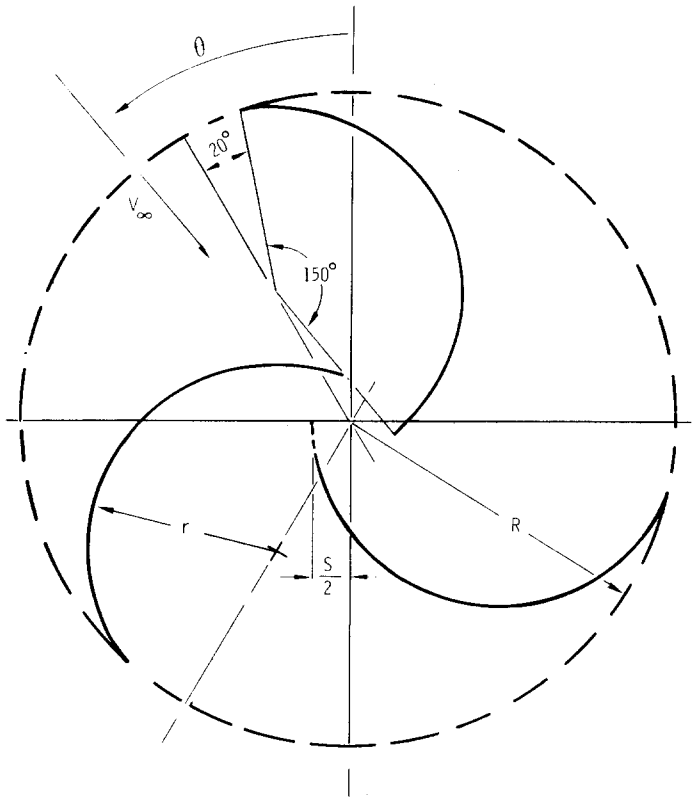

Figure 6. Schematic of the three-bucket Savonius rotor with 150° buckets.

III. TEST FACILITY

The Vought Systems Division Low Speed Wind Tunnel[18] is a horizontal single-return, tandem-test-section, closed-circuit facility. The facility contains a rectangular 2.1- x 3.0-m (7- x 10-foot) test section with a rectangular 4.6- x 6.1-m (15- x 20-foot) test section 11.9 m long located upstream of the 2.1- x 3.0-m section. This section has a windspeed range of 3 to 23 m/s. It was chosen as the test facility because of its size and speed range. Figure 1 shows the wind turbine in the (4.6- x 6.1-m) section. The photograph was taken looking downstream into the contraction section of the 2.1- x 3.0-m test section. The wind tunnel control room is located behind the windows shown on the right side of the photograph. The wind turbine instrumentation and the controls for the operation of the wind turbine, as well as the facility controls, were operated from that station. The windows permitted visual observation of the turbine and also allowed cine and television camera coverage.

All instrumentation pertaining to the operation of the facility and wind tunnel flow conditions were provided by Vought. Sandia provided the instrumentation associated with obtaining turbine torque, Q, and turbine rotational speed, Ω. The torque and turbine speed data were recorded by Vought along with their data for dynamic pressure, q_∞. The data were recorded on punched cards for later computer data reduction.

IV. TEST PROCEDURE

The Savonius rotor wind turbine, complete with support cables, was installed in the wind tunnel as shown in Figure 1. The tension of the support cables from the floor to the top of the turbine was monitored by load cells. It was checked before each run in order to provide a consistent load on the tower bearings.

Before each configuration was tested, the rotor was rotated by the air motor at a very low, but constant, rotational speed to obtain the tare torque of the system caused by the friction in the bearings. These values, of the order of 6 in-lbf, were recorded for each configuration and used in the data reduction.

The test matrix for the wind turbine tests is shown in Table I. Two types of tests were performed with the models for all fifteen configurations. The first type consisted of static tests, where the turbine rotor was locked at a particular angle relative to the flow. The static torque produced by the turbine was recorded. The rotor position was then changed by 10°, and a new value of static torque was obtained. This was done with the aid of the 19-position indexer, previously identified in Figure 3. These tests were conducted at nominal tunnel speeds of 7 and 14 m/s. In three cases with 1.5-m-high buckets and a nominal 14-m/s speed, the static torque exceeded the capacity of the torque transducer and data were not obtained.

In the second type of test, the dynamic tests, the model was rotated and a load was provided by the Gast Air Motor, as explained in section II. The turbine rotational speed was varied from runaway* down to a rotational speed where the torque exceeded the capability of the air motor. Typically for a test run, the wind tunnel speed was brought to a steady-state value, nominally 7 or 14 m/s, and the turbine, with a predetermined load provided by the air motor, was allowed to rotate. When steady-state

*Runaway is the high-speed condition where the output torque is equal to the friction torque of the system and no power is produced.

rotation was achieved, a data point was taken. A slight change in the load then caused the turbine to come to a new rotational speed. When the rotational speed was stabilized, another data point was taken.

In some cases, the air motor was used to drive the turbine at a speed in excess of the runaway speed to obtain information on the torque required to operate the device in a powered mode of operation.

TABLE I. Savonius Rotor Tests

Fig. No.	No. of Buckets	Gap (s/d)	Height, H (m)	V_∞ (m/s)	Test Condition	A_S (m^2)	R (m)	Test Reynolds No. (Re_∞/m)	Config[a] No.	Run No.
7	2	0.0	1.0	7	Static	1.0023	0.5012	4.32×10^5	7	12
7	2	0.0	1.0	14	Static	1.0023	0.5012	8.64×10^5	7	13
8	2	0.1	1.0	7	Static	0.9523	0.4762	4.32×10^5	11	27
8	2	0.1	1.0	14	Static	0.9523	0.4762	8.64×10^5	11	28
9	2	0.15	1.0	7	Static	0.9273	0.4637	4.32×10^5	9	19
9	2	0.15	1.0	14	Static	0.9273	0.4637	8.64×10^5	9	20
10	2	0.2	1.0	7	Static	0.9023	0.4512	4.32×10^5	13	35
10	2	0.2	1.0	14	Static	0.9023	0.4512	8.64×10^5	13	36
11	2	0.0	1.5	7	Static	1.5035	0.5012	4.33×10^5	15	43
12	2	0.1	1.5	7	Static	1.4285	0.4762	4.33×10^5	19	56
13	2	0.15	1.5	7	Static	1.3910	0.4637	4.33×10^5	17	49
14	2	0.0	1.0	7	Dynamic	1.0023	0.5012	4.32×10^5	7	14
15	2	0.1	1.0	7	Dynamic	0.9523	0.4762	4.32×10^5	11	29
15	2	0.1	1.0	14	Dynamic	0.9523	0.4762	8.64×10^5	11	30
16	2	0.15	1.0	7	Dynamic	0.9273	0.4637	4.32×10^5	9	21
16	2	0.15	1.0	14	Dynamic	0.9273	0.4637	8.64×10^5	9	22
17	2	0.2	1.0	7	Dynamic	0.9023	0.4512	4.32×10^5	13	37
17	2	0.2	1.0	14	Dynamic	0.9023	0.4512	8.64×10^5	13	38
18	2	0.0	1.5	7	Dynamic	1.5035	0.5012	4.33×10^5	15	44
19	2	0.1	1.5	7	Dynamic	1.4285	0.4762	4.33×10^5	19	57
19	2	0.1	1.5	14	Dynamic	1.4285	0.4762	8.67×10^5	19	58
20	2	0.15	1.5	7	Dynamic	1.3910	0.4637	4.33×10^5	17	50
20	2	0.15	1.5	.14	Dynamic	1.3910	0.4637	8.67×10^5	17	51
21	3	0.0	1.0	7	Static	0.9871	0.4936	4.32×10^5	12	31
21	3	0.0	1.0	14	Static	0.9871	0.4936	8.64×10^5	12	32
22	3	0.1	1.0	7	Static	0.9380	0.4690	4.32×10^5	8	15
22	3	0.1	1.0	14	Static	0.9380	0.4690	8.64×10^5	8	16
23	3	0.15	1.0	7	Static	0.9134	0.4567	4.32×10^5	14	39
23	3	0.15	1.0	14	Static	0.9134	0.4567	8.64×10^5	14	40
24	3	0.2	1.0	7	Static	0.8888	0.4444	4.32×10^5	10	23
24	3	0.2	1.0	14	Static	0.8888	0.4444	8.64×10^5	10	24
25	3	0.0	1.5	7	Static	1.4807	0.4936	4.33×10^5	20	59
25	3	0.0	1.5	14	Static	1.4807	0.4936	8.67×10^5	20	60
26	3	0.1	1.5	7	Static	1.4070	0.4690	4.33×10^5	16	45
26	3	0.1	1.5	14	Static	1.4070	0.4690	8.67×10^5	16	46
27	3	0.2	1.5	7	Static	1.3333	0.4444	4.33×10^5	18	52
27	3	0.2	1.5	14	Static	1.3333	0.4444	8.67×10^5	18	53
28	3	0.2	1.5	7	Static	1.3535	0.4512	4.33×10^5	21[b]	63
28	3	0.2	1.5	14	Static	1.3535	0.4512	8.67×10^5	21[b]	64
29	3	0.0	1.0	7	Dynamic	0.9871	0.4936	4.32×10^5	12	33
29	3	0.0	1.0	14	Dynamic	0.9871	0.4936	8.64×10^5	12	34
30	3	0.1	1.0	7	Dynamic	0.9380	0.4690	4.32×10^5	8	17
30	3	0.1	1.0	14	Dynamic	0.9380	0.4690	8.64×10^5	8	18
31	3	0.15	1.0	7	Dynamic	0.9134	0.4567	4.32×10^5	14	41
31	3	0.15	1.0	14	Dynamic	0.9134	0.4567	8.64×10^5	14	42
32	3	0.2	1.0	7	Dynamic	0.9134	0.4567	4.32×10^5	10	25
32	3	0.2	1.0	14	Dynamic	0.8888	0.4444	8.64×10^5	10	26
33	3	0.0	1.5	7	Dynamic	1.4807	0.4936	4.33×10^5	20	61
33	3	0.0	1.5	14	Dynamic	1.4807	0.4936	8.67×10^5	20	62
34	3	0.1	1.5	14	Dynamic	1.4070	0.4690	4.33×10^5	16	47
34	3	0.1	1.5	14	Dynamic	1.4070	0.4690	8.67×10^5	16	48
35	3	0.2	1.5	14	Dynamic	1.3333	0.4444	4.33×10^5	18	54
35	3	0.2	1.5	14	Dynamic	1.3333	0.4444	8.67×10^5	18	55
36	3	0.2	1.5	7	Dynamic	1.3535	0.4512	4.33×10^5	21[b]	65
36	3	0.2	1.5	14	Dynamic	1.3535	0.4512	8.67×10^5	21[b]	66

[a] Note that the configuration numbers do not run chronologically from 1 to 15. Other tests, outside the interest of this report, were conducted simultaneously.

[b] Configuration 21 had 180° buckets.

V. DATA REDUCTION

The wind tunnel turbulence factor for the 15- x 20-foot section[18] is quite high: 1.4 at a velocity of 20 m/s. Since this turbulence factor is determined by a stationary turbulence sphere and the wind turbine buckets are moving at a speed other than the windspeed, the use of a turbulence factor to correct to an effective Reynolds number was not attempted. Repeating: no Reynolds numbers stated in this report are corrected for the wind tunnel turbulence factor.

When an object is placed in a wind tunnel, the object produces some "tunnel blockage," which causes an increase in the local wind velocity in the test section. This increase has to be accounted for by the determination of a tunnel blockage factor, ϵ, sometimes called the velocity increment. The total factor is the sum of the velocity increment caused by wake blockage and solid blockage. The determination of these two blockage corrections is very difficult when an unusual shape, such as the Savonius rotor test models, is tested in a wind tunnel. Pope and Harper[19] suggest that the total tunnel blockage correction be determined by the following equation:

$$\epsilon = \frac{1}{4}\frac{\text{Model Frontal Area}}{\text{Test Section Area}} \qquad (1)$$

The model frontal area was taken to be the turbine-swept-area, A_s, plus the frontal area of the stand and related hardware. This gave a value for ϵ of 0.0125 for the 1-m-high Savonius rotor and of 0.0162 for the 1-1/2-m-high rotor.

Recent analytical studies,[20] along with unpublished data of the authors, indicate that the Savonius rotor experiences side forces that are of the same order of magnitude as the downwind (drag) force. For this case, one should question the validity of the blockage given by Eq. (1). At present, however, there are no proved blockage correction factors for Savonius rotors; hence, it is felt that Eq. (1) should be applied.

For the uncertainty analysis presented in the Appendix, it was assumed that the uncertainty in ϵ was 50 percent. Despite this large uncertainty, the uncertainty in ϵ was not the major contributor to the overall uncertainty in power coefficient, torque coefficient, and speed ratio.

The above values for the blockage factor were used to correct the freestream velocity and dynamic pressure as shown, where the subscript u refers to uncorrected values:

$$V_\infty = V_{\infty_u} (1 + \epsilon) \tag{2}$$

$$q_\infty = q_{\infty_u} (1 + \epsilon)^2 \quad . \tag{3}$$

The data taken by Vought consisted of q_∞, Ω, P_∞, T_∞, which were automatically punched on computer cards. The freestream density, ρ_∞, was calculated by using the ideal gas equation of state with the measured values of P_∞ and T_∞. Knowing ρ_∞, one can determine the freestream velocity by

$$V_\infty = \sqrt{\frac{2q_\infty}{\rho_\infty}} \quad , \tag{4}$$

where q_∞ has been corrected by the blockage factor. The Reynolds number per unit length for each test condition is computed by

$$Re_\infty = \frac{\rho_\infty V_\infty}{\mu_\infty} \quad . \tag{5}$$

The computation of the performance data proceeds as follows:

$$X_\infty = \frac{R\Omega}{V_\infty} \tag{6}$$

$$C_Q = \frac{Q + Q_f}{1/2\rho_\infty V_\infty^2 R A_s} \quad , \tag{7}$$

$$C_P = \frac{(Q + Q_f)\,\Omega}{1/2\rho_\infty V_\infty^3 A_s} \quad . \tag{8}$$

The data for torque and power coefficients are plotted as a function of the turbine speed ratio. Static torque coefficients are plotted as a function of rotor angular position. All data are corrected for tunnel blockage and tare torque.

VI. TEST RESULTS

The test conditions, run numbers, and geometrical information for each configuration are listed in Table I. For a given number of buckets and a given bucket height the runs are ordered with increasing gap width. The run number is the sequence in which each configuration was tested. The basic data for all configurations tested are presented in Figures 7 through 36b, where the ordering of the basic data plots corresponds to the ordering in Table I. For each configuration there are plots of static torque coefficients as a function of angular position and torque and power coefficients as a function of speed ratio. In most cases, there are data for two Reynolds numbers. Where data are presented for only one Reynolds number, the data for the other Reynolds number were not obtainable for any of three reasons: the torque was outside the transducer calibration, the torque was outside the capability of the Gast air motor, or a problem with rotor vibration was encountered. The tabulated Reynolds numbers are for a length scale of 1 m; however, the turbines are nominally 1 m in diameter and the Reynolds numbers are therefore the approximate Reynolds number based on turbine diameter. The reason the Reynolds number is presented as a per-metre value is that there is no universally accepted length scale with which to calculate a Reynolds number for a Savonius rotor. Sufficient information is given in Table I that the reader may calculate a Reynolds number based on a dimension of his own choosing, be it the turbine diameter, turbine radius, bucket diameter, bucket radius, or whatever.

Figures 7 through 13 present the static torque coefficient data as a function of angular position for the two-bucket configurations. Figure 5 gives the origin of the angular position coordinate system. With the exception of the zero gap configuration ($s/d = 0$, Figure 7), the torque coefficient is positive for all angular positions. There is, however, a wide variation in the static torque coefficient with angular position. In order to ensure that a Savonius rotor will start from any initial angular position, the static aerodynamic torque must exceed the combined load and friction torques. This constraint implies that the minimum value of the static torque coefficient may control the required size of a Savonius starter. The data in Figures 7 through 13 suggest that a two-bucket Savonius rotor might be a poor choice for a starter system

because the minimum C_Q is quite small in many cases. This problem can be circumvented, however, by utilizing two sets of Savonius rotors, with one set being rotated 90° from the other. The resulting torque coefficient curve for a typical hypothetical rotation of 90° is shown in Figure 8. The minimum torque coefficient is increased by a factor of approximately 5.

The Reynolds number has an effect on the static torque coefficients, as is evidenced by the data in Figures 7 through 10. A shift in the C_Q curve is apparently caused by delayed separation around the buckets with increased Reynolds number.

The power and torque coefficient data for the two-bucket configurations are presented as a function of turbine speed ratio in Figures 14a through 20b. The values of torque coefficient plotted at the speed ratio of zero were obtained by averaging the static torque coefficients over one cycle (0 to 180°) of the rotor. The power coefficients for all configurations peak near the speed ratio of 0.9 with the exception of the configurations with no gap (7 and 15), where the power coefficient peaks near a speed ratio of 0.8. The peak value of power coefficient for the two-bucket configurations ranges from 0.22 to 0.26. The maximum torque coefficient occurs at a lower speed ratio, generally in the vicinity of 0.4 for all the configurations with two buckets. Although there is a noticeable increase in power and torque coefficient with increased Reynolds number, this increase is generally within the data uncertainty (see Appendix).

The plots of static torque coefficient as a function of angular position for the three-bucket configurations are shown in Figures 21 through 28. The angular orientation for the three-bucket rotor is shown in Figure 6. Note that the bucket tips do not lie on the 0°, 120°, and 240° rays; they are off because of the 20° shortening of the bucket arc. Although most of the data plots are for 180° rotation, because that option was available on the indexer, a full cycle for a three-bucket configuration is 120°. With the three-bucket configurations, there is no angular position where the static torque coefficient is negative. The three-bucket configurations exhibit a smaller variation in static torque coefficient than do the two-bucket configurations. the average torque coefficient for one cycle is normally in the range of 0.3 to 0.4 for the three-bucket configurations and is similar to that for the two-bucket configurations. Also, as with the two-bucket configurations, the angular position at which stall occurs is a function of Reynolds number.

The power and torque coefficients as a function of turbine speed ratio are given in Figures 29a through 36b for the three-bucket configurations for two Reynolds numbers. Generally there is a slight improvement in performance with increased Reynolds number. This is not true for all the data; the exact reason for these anomalies in the data in which the lower Reynolds number data has better performance is not known. These results can be seen in Figure 32 (Configuration 10) and Figure 34 (Configuration 16). Again, the difference due to Reynolds number lies within the data uncertainty.

Figure 37 compares the performance of typical two- and three-bucket configurations. From a performance viewpoint, the two-bucket configuration is superior in most respects. The maximum power coefficient of the two-bucket configuration is approximately 1.5 times that for the three-bucket configuration. The speed ratio where C_p is a maximum increases when the number of buckets goes from three to two. It appears that the only performance advantage a three-bucket configuration has over a two-bucket configuration is that the minimum static torque is greater. However, this advantage can be removed by staggering two sets of two-bucket rotors. The remaining discussion will center on the characteristics of the two-bucket rotors.

The effect of rotor height is examined in Figure 38 for a two-blade configuration with $s/d = 0.15$. The fact that the power and torque coefficients increase slightly with increasing bucket height indicates that the endplates did provide a reduction in end losses. In general, the data trends for the 1.5-m-high buckets were similar to the 1-m-high buckets.

The effect of gap width on rotor performance is presented in Figures 39 and 40. The low Reynolds number test data in Figure 39 indicate superior performance for a gap width of $s/d = 0.1$-0.15. Both larger and smaller gaps show a decrease in performance. The performance difference is the most noticeable at the higher speed ratios. A similar trend is shown in Figure 40 for the high Reynolds number test data. Although the uncertainty analysis in the Appendix indicates that the uncertainty bands for the various gap widths will overlap, the data seem to indicate that the gap width s/d should be in the range of 0.1 to 0.15.

A very simple means of fabricating a Savonius rotor is to cut an oil drum in half, invert one half, and weld the two pieces together. For this type of configuration where the bucket size is fixed, it would be desirable to know what gap width will produce maximum power, $P = Q\Omega$, and torque, Q. Figure 41a presents power, $Q\Omega$, normalized by a factor that is constant for all configurations ($1/2\ \rho V_\infty^3\ 4\ r\ H$) as a function of turbine rotational velocity, Ω, multiplied by the value $2r/V_\infty$. All three smaller gap widths, which appear to reach approximately the same maximum power, are better than the $s/d = 0.2$ curve. At the low rotational speeds, the $s/d = 0$ curve appears best but shows poorer performance at high rotational speeds. Figure 41b presents the dimensionless torque as a function of dimensionless rotational speed. Again, the zero gap width exhibits the maximum torque but has poorer performance at the higher rotational speeds. The largest gap width configuration exhibits the worst performance at low-to-intermediate rotational speeds. The general conclusion to be drawn from the data in Figure 41 is that some gap is desirable, but it should not be so great that it will cause considerable reduction in the rotor-swept area and radius of rotation.

Figure 42 compares one data set of this report with data from Shankar.[15] The agreement between the two data sets is quite good at the high speed ratios but is relatively poor at low speed ratios. No satisfactory explanation has been found for this discrepancy. Data for a three-bucket configuration were not compared because of model geometrical differences between this study and Shankar.

VII. SUMMARY AND CONCLUSIONS

Tests of 15 configurations of a Savonius rotor included such parameters as number of buckets, freestream velocity, rotor height, and bucket overlap or gap width. The following general conclusions were drawn from the test data:

1. The static torque coefficient is much more variable with angular position for a two-bucket configuration than for a three-bucket configuration.
2. The two-bucket configurations have better aerodynamic performance than the three-bucket configurations, with the exception of starting torque.
3. Increasing the test Reynolds number generally improves aerodynamic performance.
4. Performance increases slightly with increasing height-to-diameter ratio.
5. A dimensionless gap width of $s/d = 0.1\text{-}0.15$ appears to yield optimum performance.
6. For a fixed bucket size (as with oil drums), the recommended gap width is $s/d = 0.1\text{-}0.15$.
7. The recommended configuration is two sets of two-bucket rotors, rotated 90° apart, with each rotor having a gap width of $s/d = 0.1\text{-}0.15$.

The data presented here, along with the data of Shankar,[15] should provide a significant data base for the study and use of Savonius rotors.

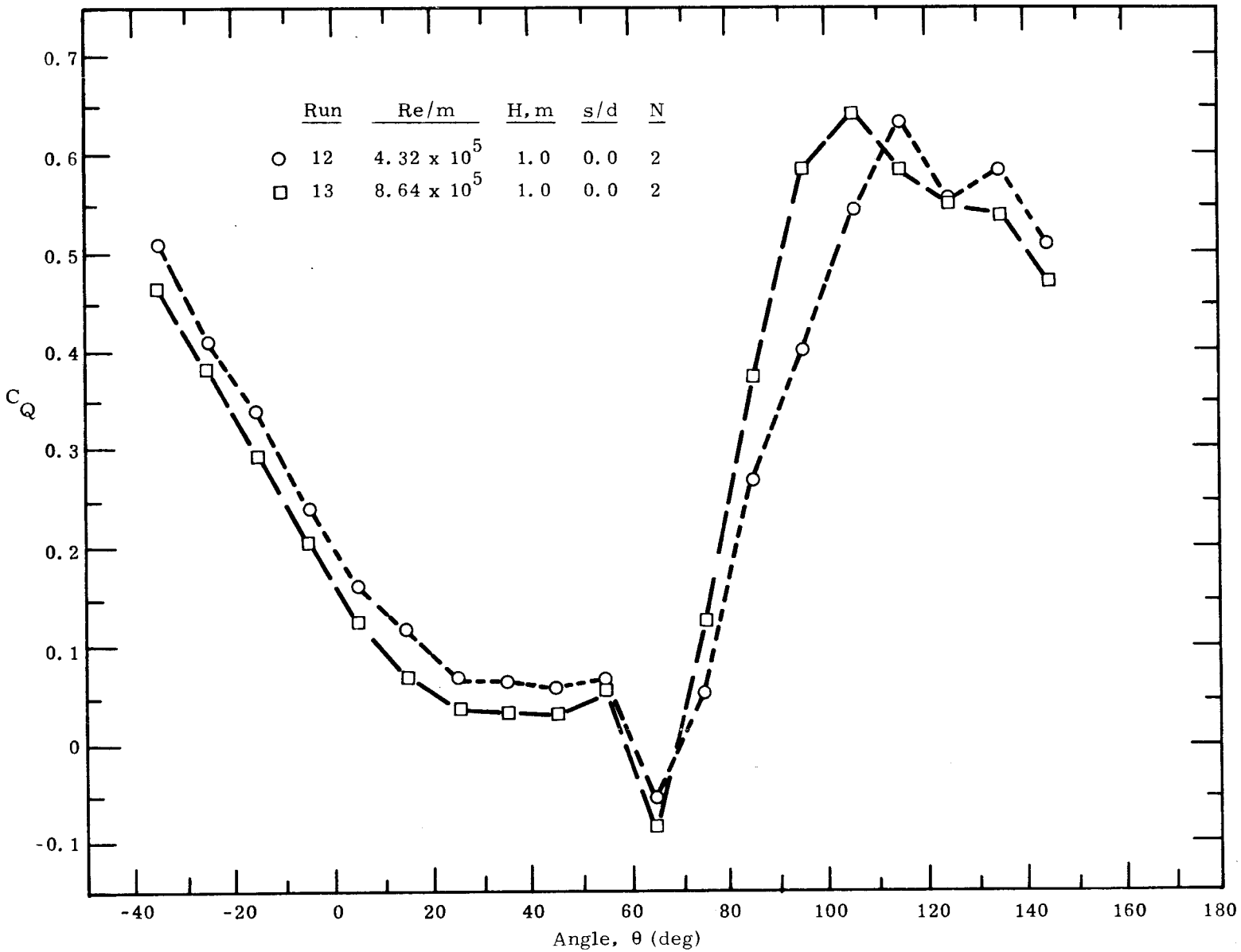

Figure 7. The static torque coefficient as a function of angular position for a two-bucket Savonius rotor (Configuration 7) with a gap width ratio of 0.0 for Re/m of 4.32×10^5 and 8.64×10^5.

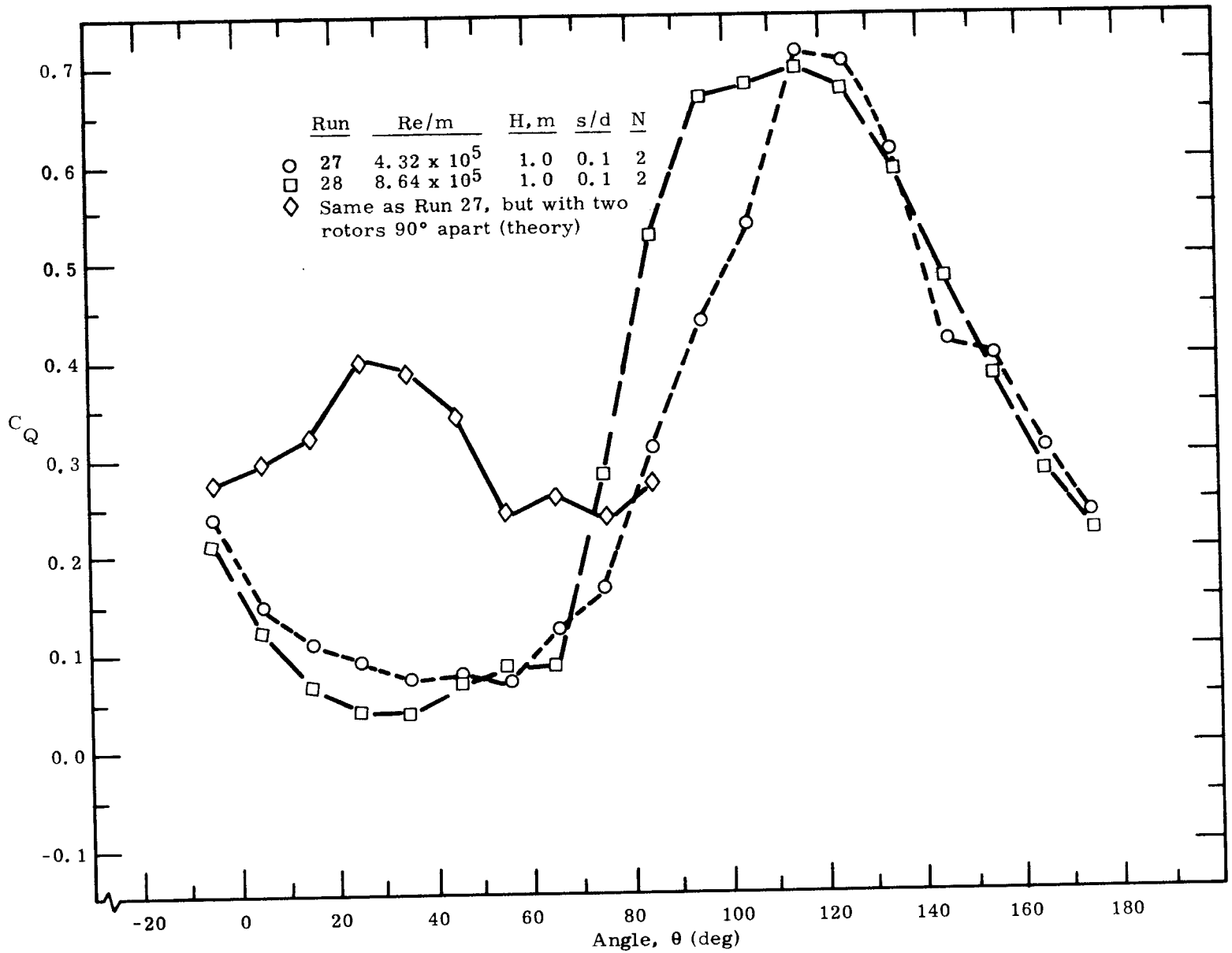

Figure 8. The static torque coefficient as a function of angular position for a two-bucket Savonius rotor (Configuration 11) with a gap width ratio of 0.10 for Re/m of 4.32×10^5 and 8.64×10^5.

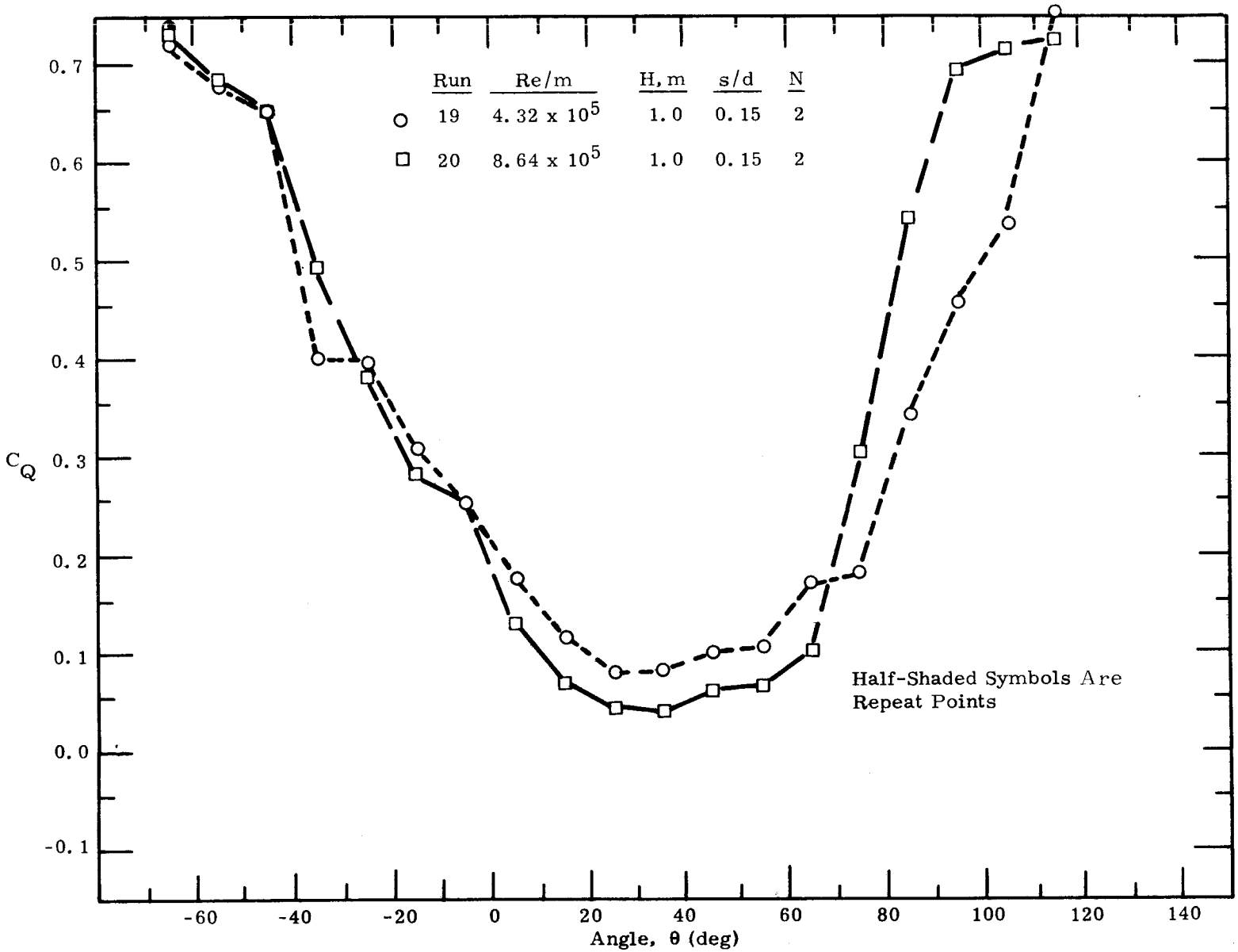

Figure 9. The static torque coefficient as a function of angular position for a two-bucket Savonius rotor (Configuration 9) with a gap width ratio of 0.15 for Re/m of 4.32×10^5 and 8.64×10^5.

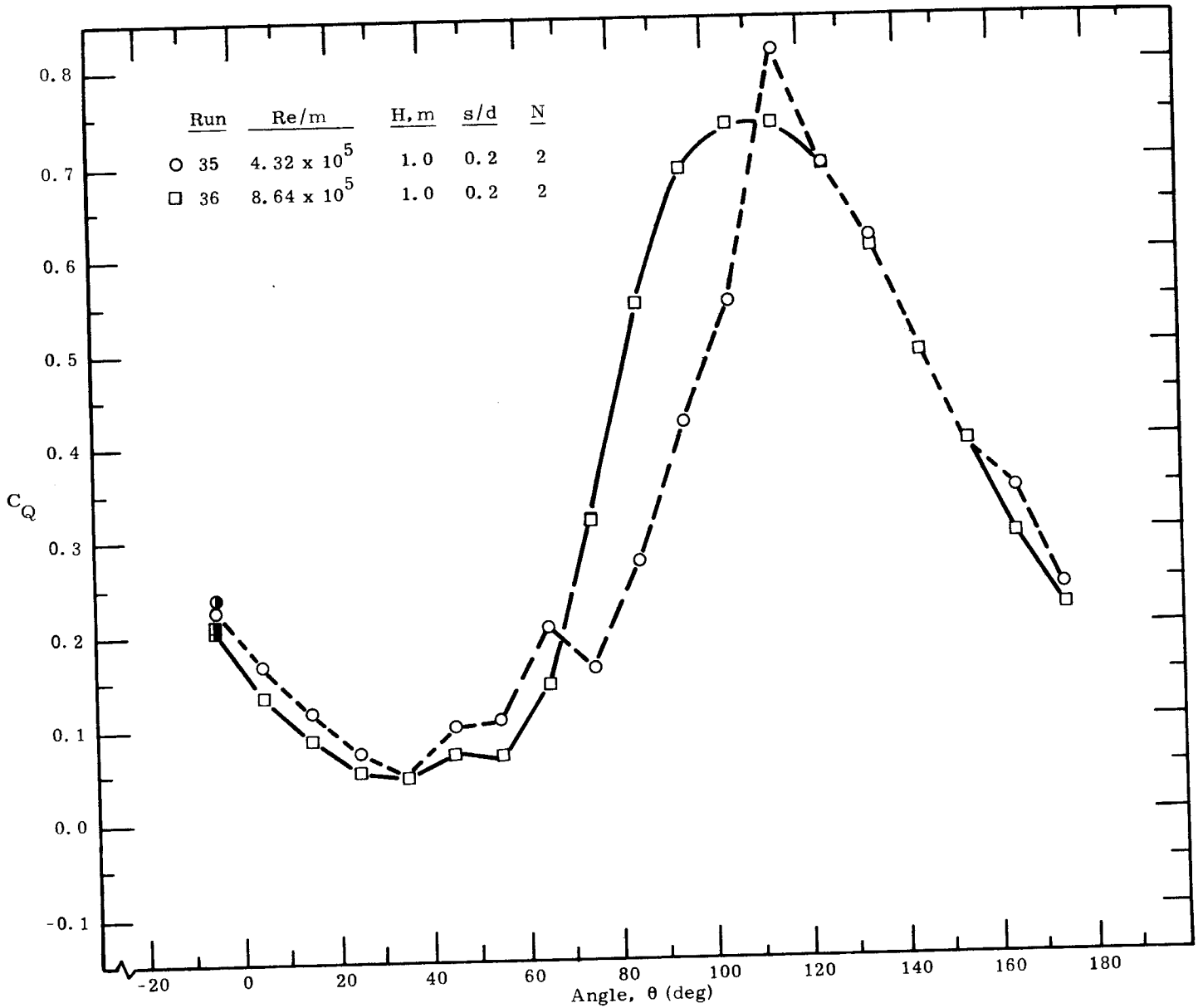

Figure 10. The static torque coefficient as a function of angular position for a two-bucket Savonius rotor (Configuration 13) with a gap width ratio of 0.20 for Re/m of 4.32×10^5 and 8.64×10^5.

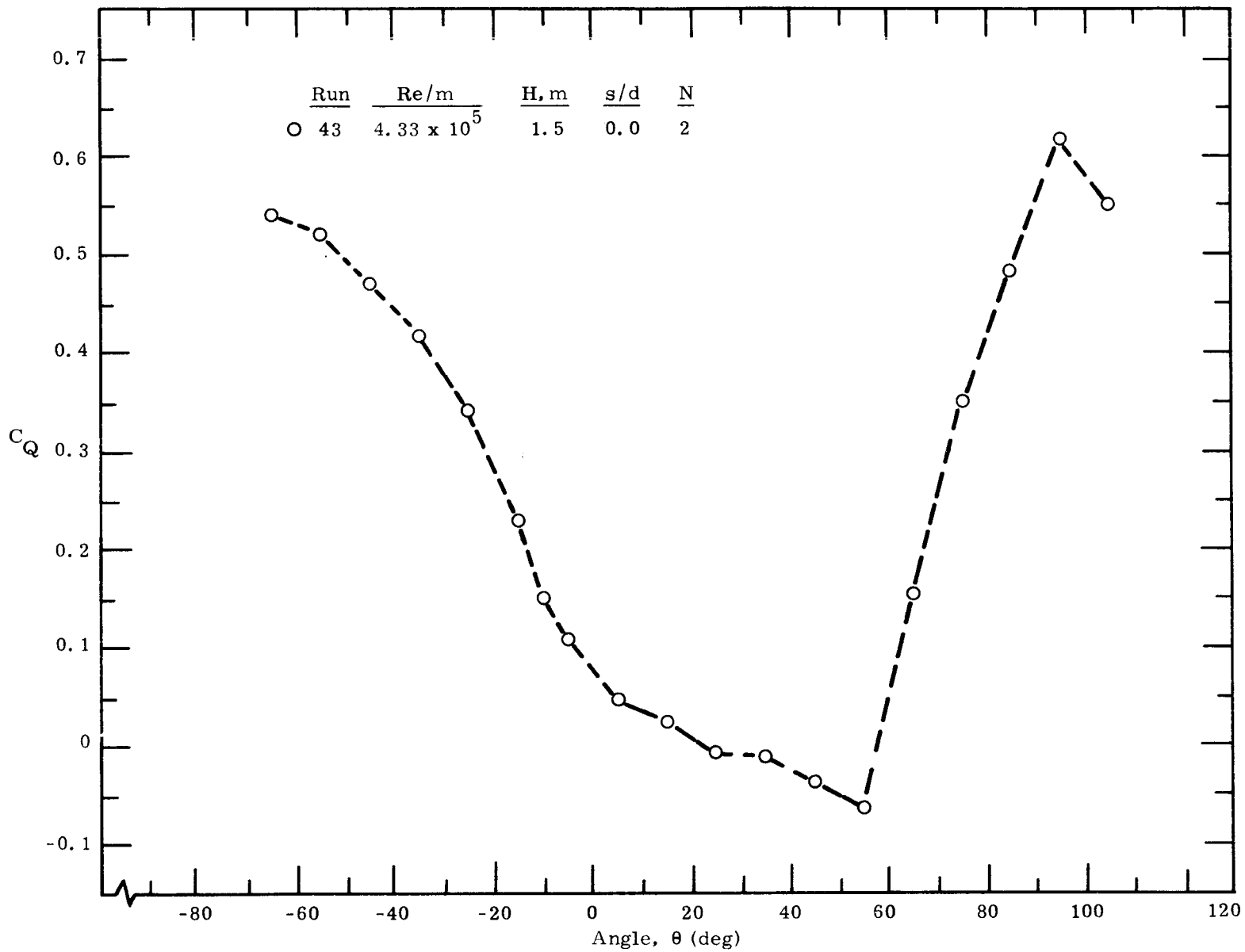

Figure 11. The static torque coefficient as a function of angular position for a two-bucket Savonius rotor (Configuration 15) with a gap width ratio of 0.0 for Re/m of 4.33×10^5.

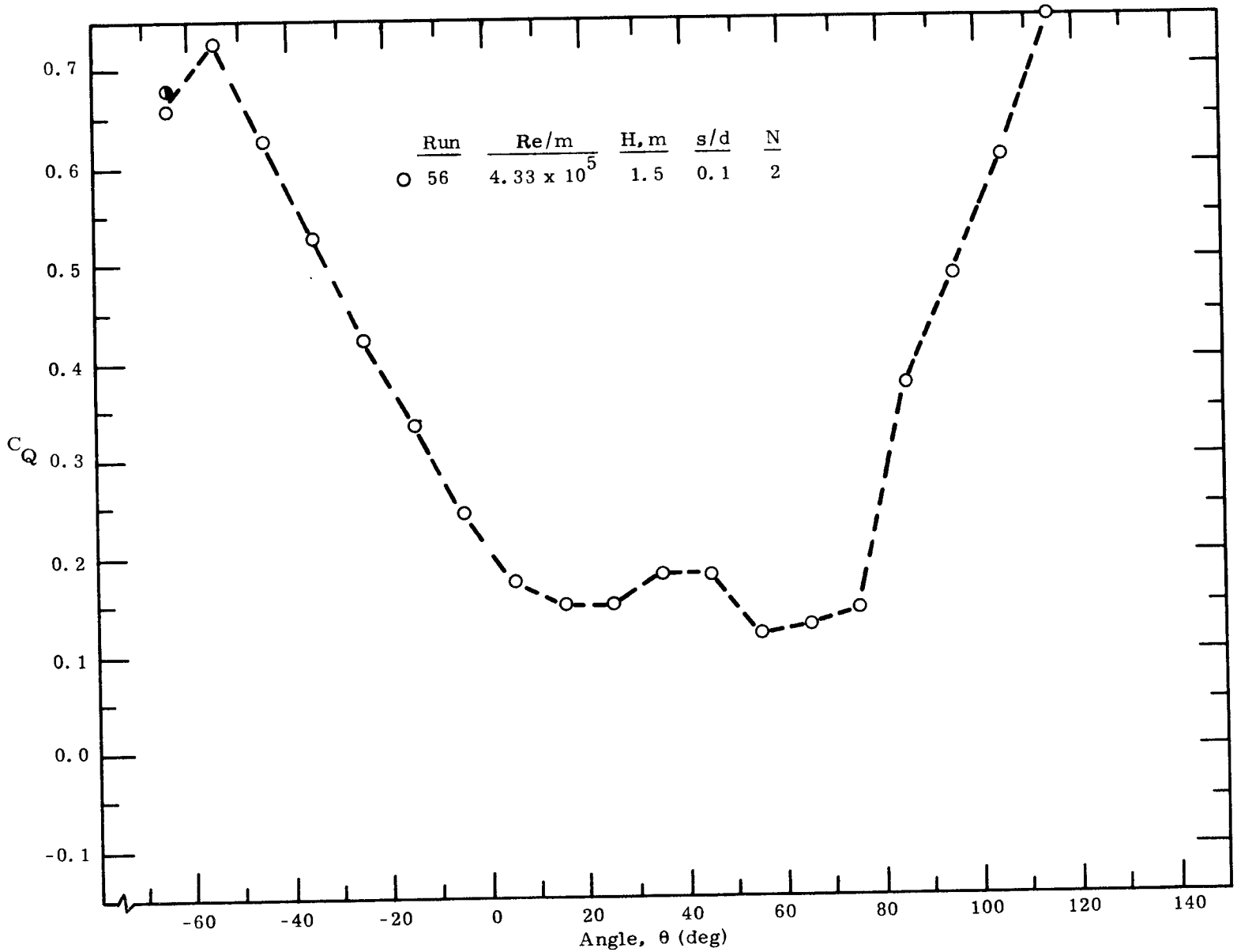

Figure 12. The static torque coefficient as a function of angular position for a two-bucket Savonius rotor (Configuration 19) with a gap width ratio of 0.10 for Re/m of 4.33×10^5.

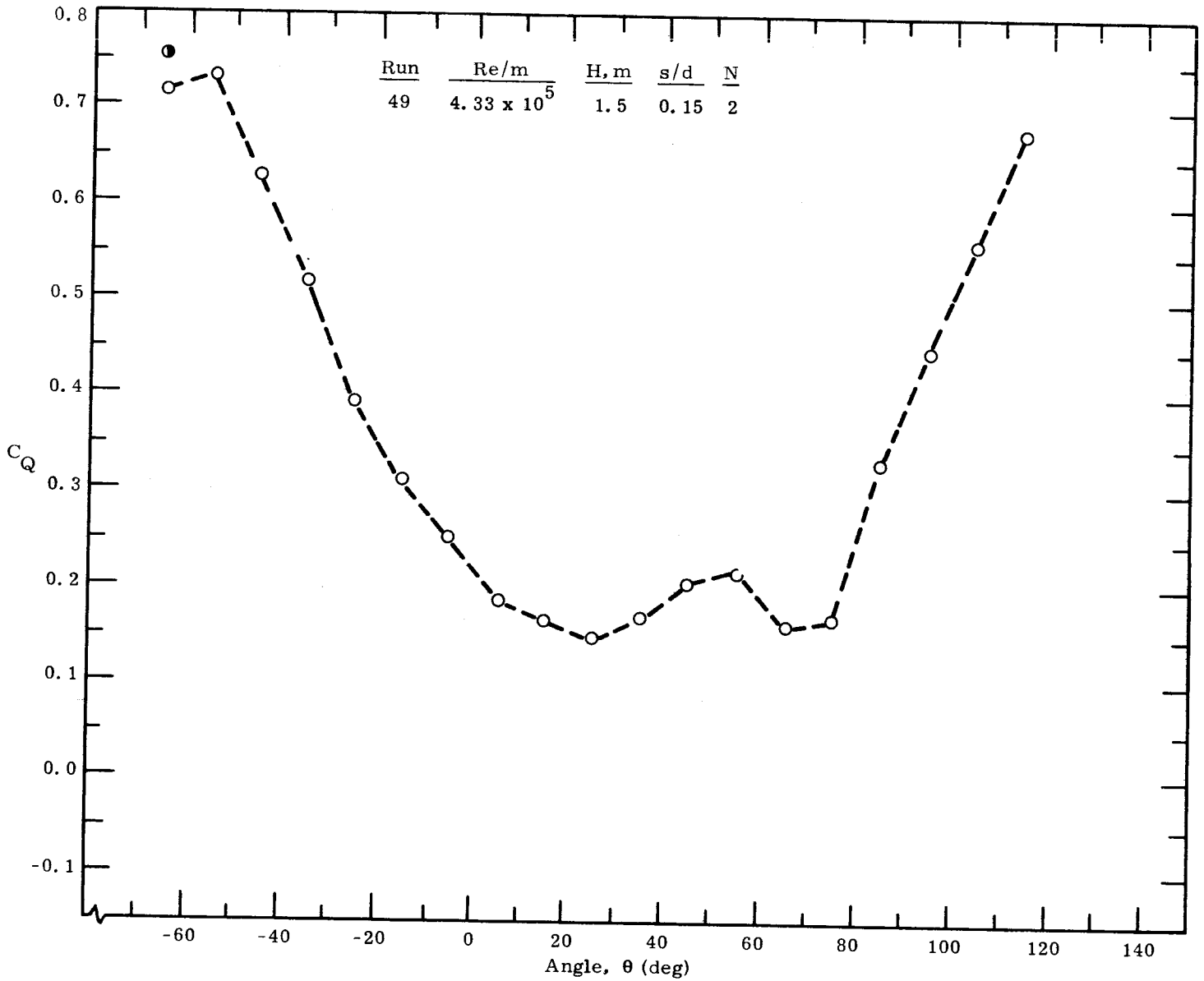

Figure 13. The static torque coefficient as a function of angular position for a two-bucket Savonius rotor (Configuration 17) with a gap width ratio of 0.15 for Re/m of 4.33×10^5.

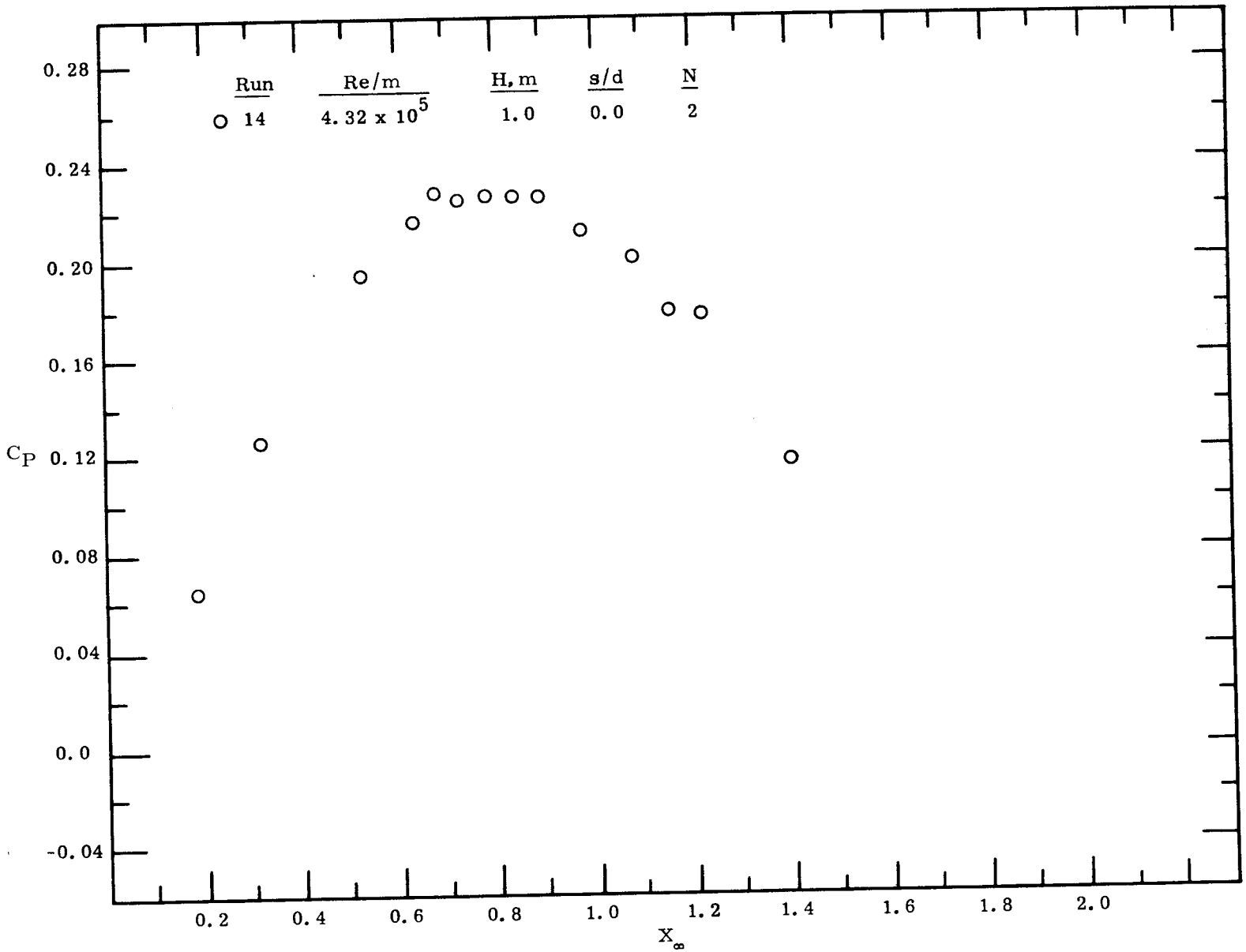
Run
Re/m
H, m
s/d
N
14
4.32 x 10^5
1.0
0.0
2
0.28
0.24
0.20
0.16
0.12
0.08
0.04
0.0
-0.04
C_P
0.2
0.4
0.6
0.8
1.0
1.2
1.4
1.6
1.8
2.0
X_∞

(a)

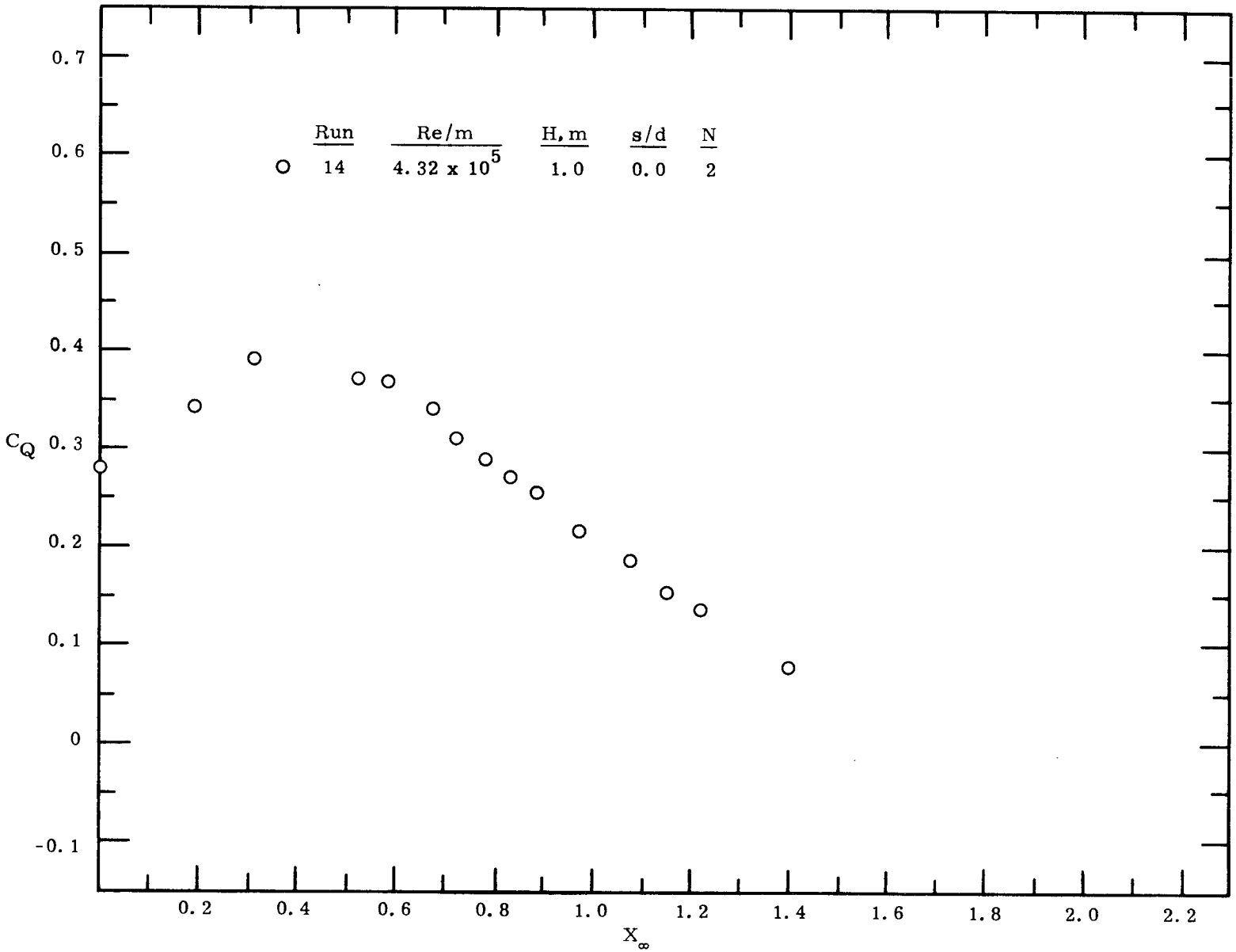

(b)

Figure 14. Power and torque coefficients as a function of speed ratio for a two-bucket Savonius rotor (Configuration 7) with a gap width ratio of 0.0 for Re/m of 4.32×10^5.

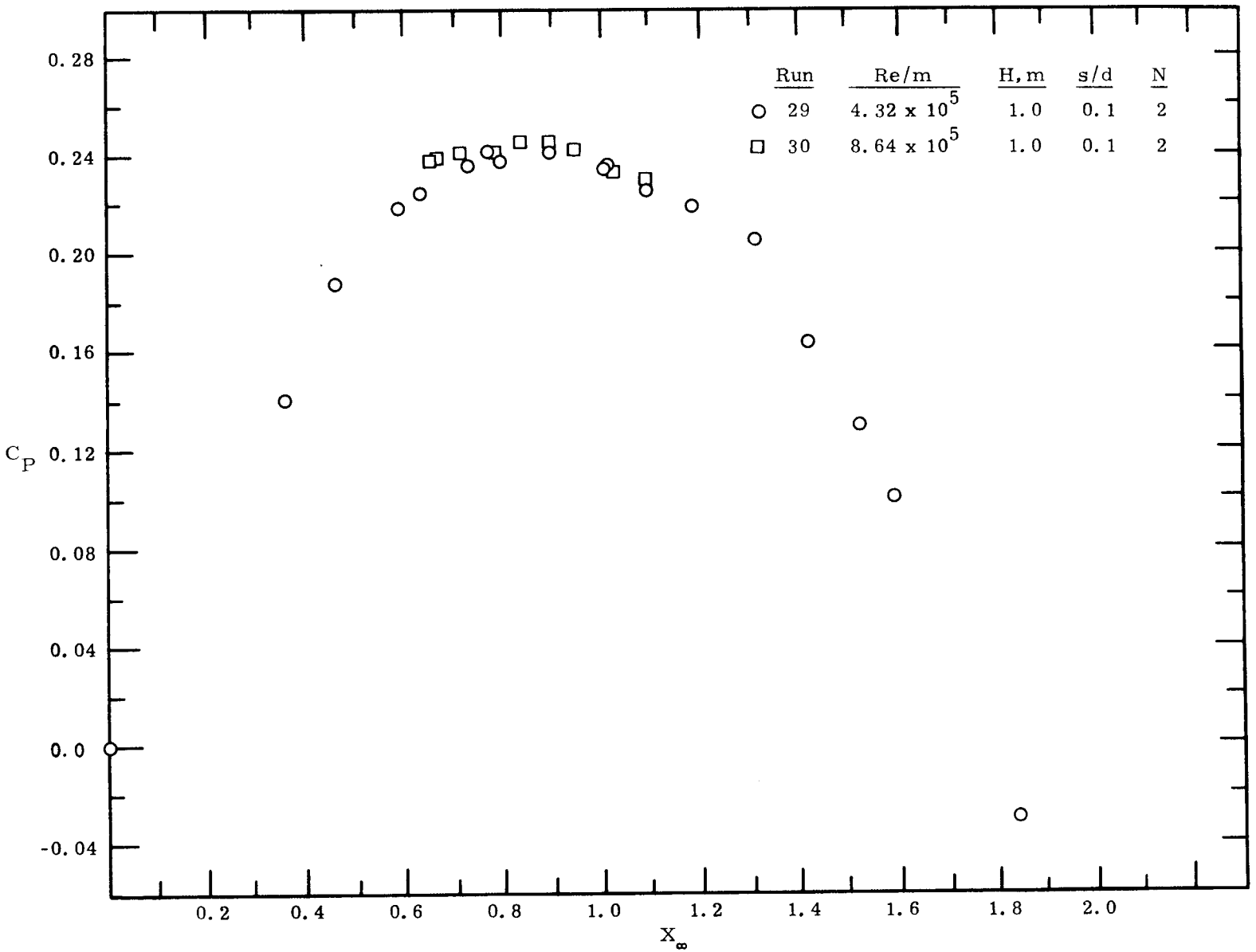
Run
Re/m
H, m
s/d
N
29
4.32 x 10^5
1.0
0.1
2
30
8.64 x 10^5
1.0
0.1
2
0.28
0.24
0.20
0.16
0.12
0.08
0.04
0.0
-0.04
C_P
0.2
0.4
0.6
0.8
1.0
1.2
1.4
1.6
1.8
2.0
X_∞

(a)

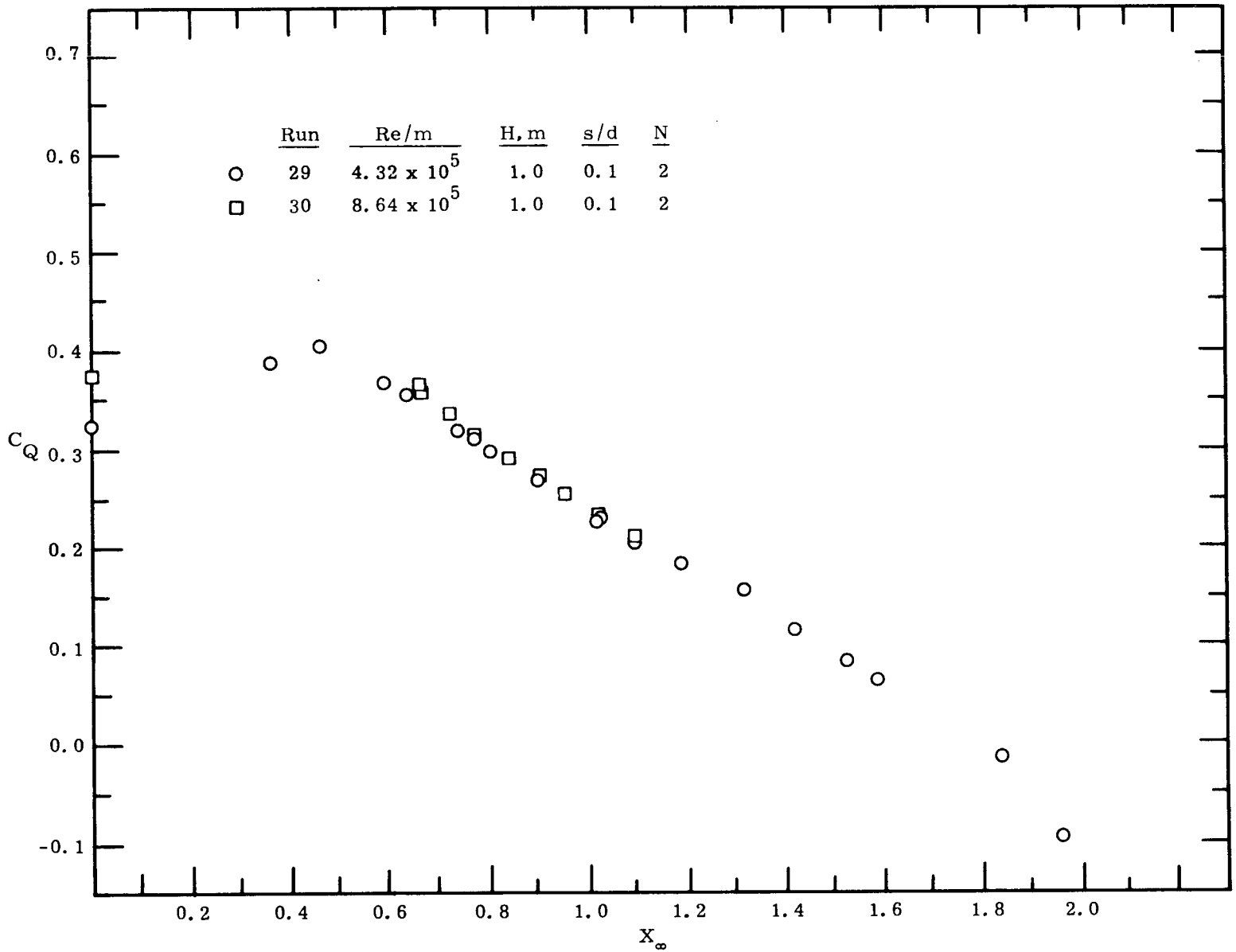

(b)

Figure 15. Power and torque coefficients as a function of speed ratio for a two-bucket Savonius rotor (Configuration 11) with a gap width ratio of 0.10 for Re/m of 4.32×10^5 and 8.64×10^5.

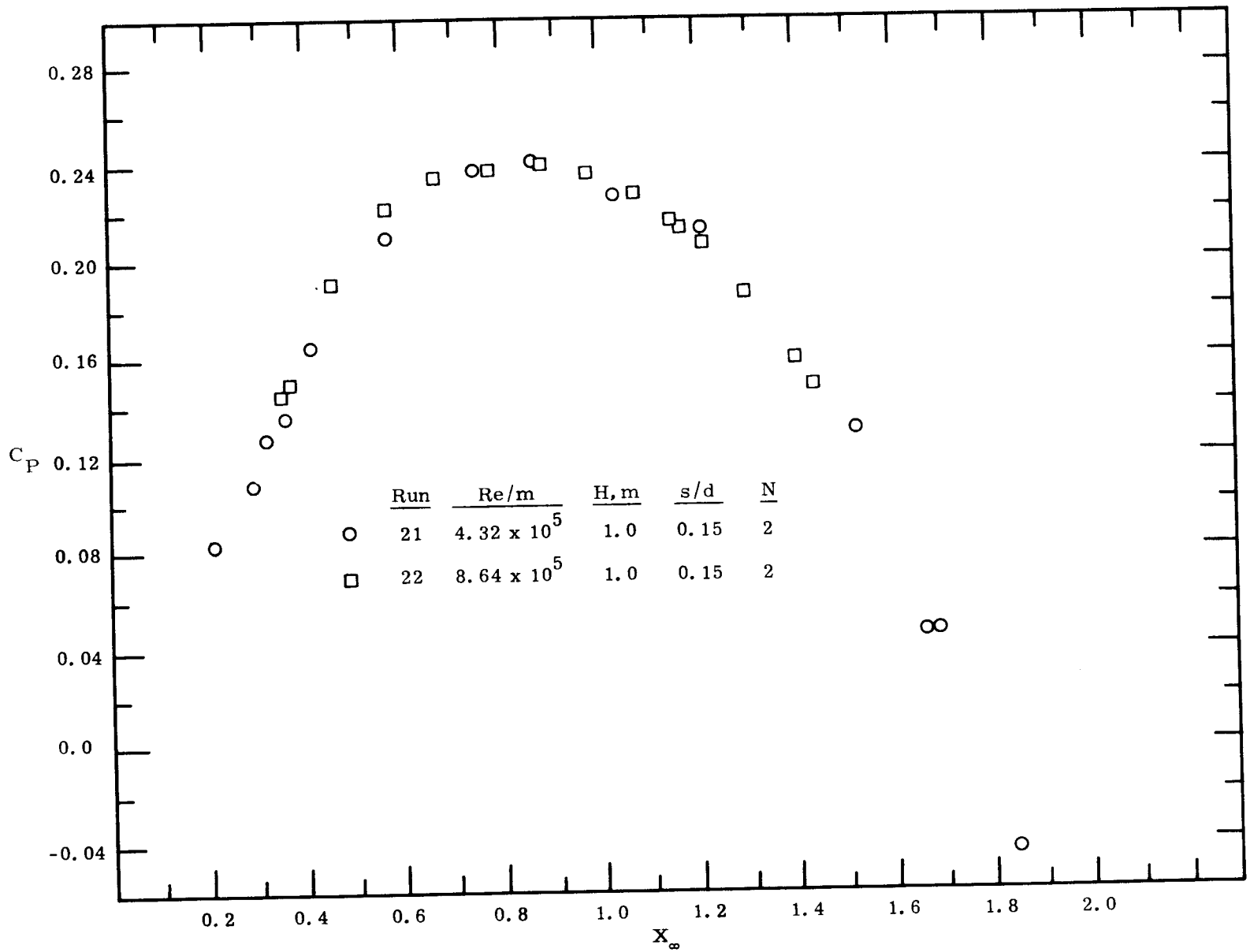
0.28
0.24
0.20
0.16
0.12
0.08
0.04
0.0
-0.04
C_P
0.2
0.4
0.6
0.8
1.0
1.2
1.4
1.6
1.8
2.0
X_∞
Run Re/m H, m s/d N
21 4.32 x 10^5 1.0 0.15 2
22 8.64 x 10^5 1.0 0.15 2

(a)

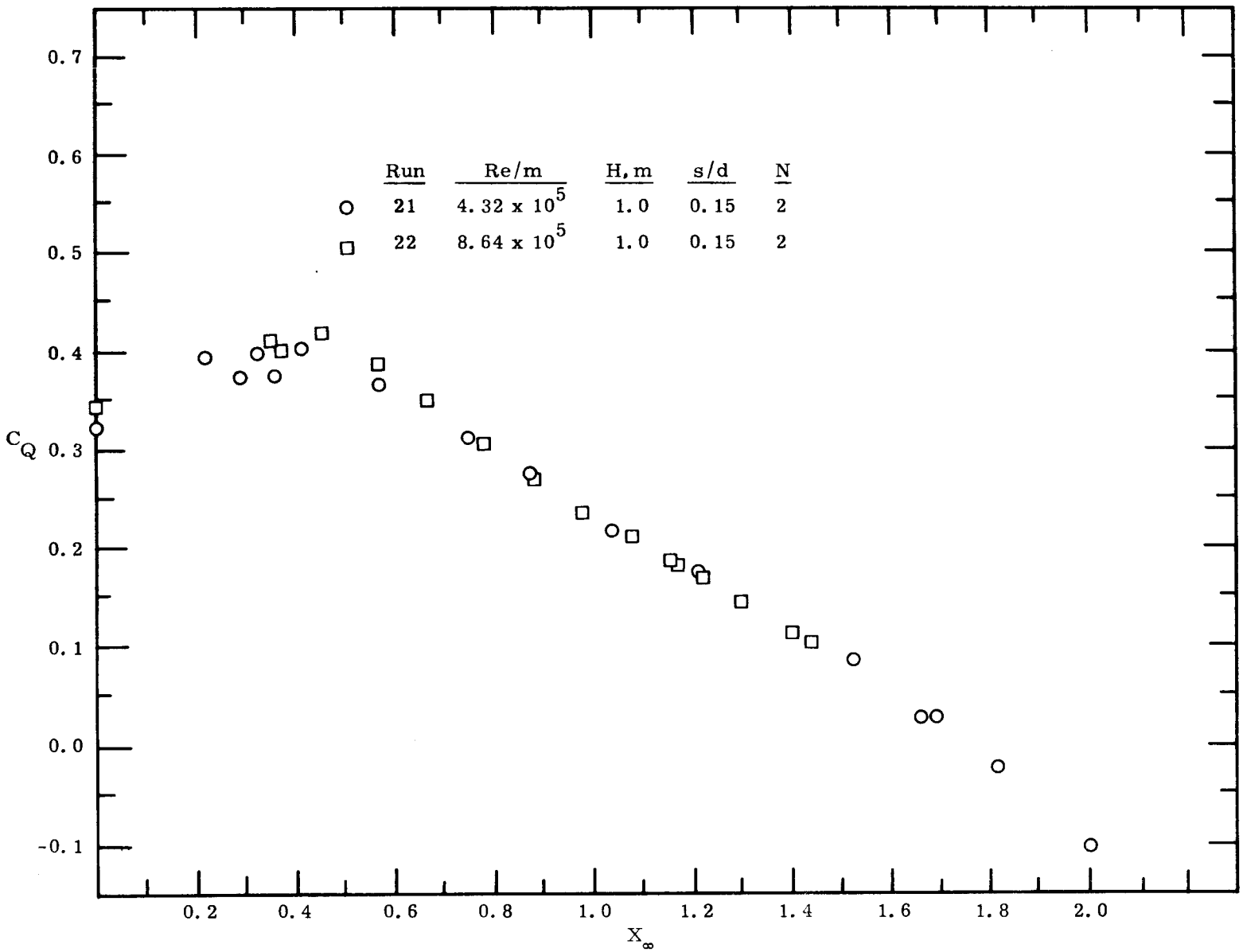

(b)

Figure 16. Power and torque coefficients as a function of speed ratio for a two-bucket Savonius rotor (Configuration 9) with a gap width ratio of 0.15 for Re/m of 4.32×10^5 and 8.64×10^5.

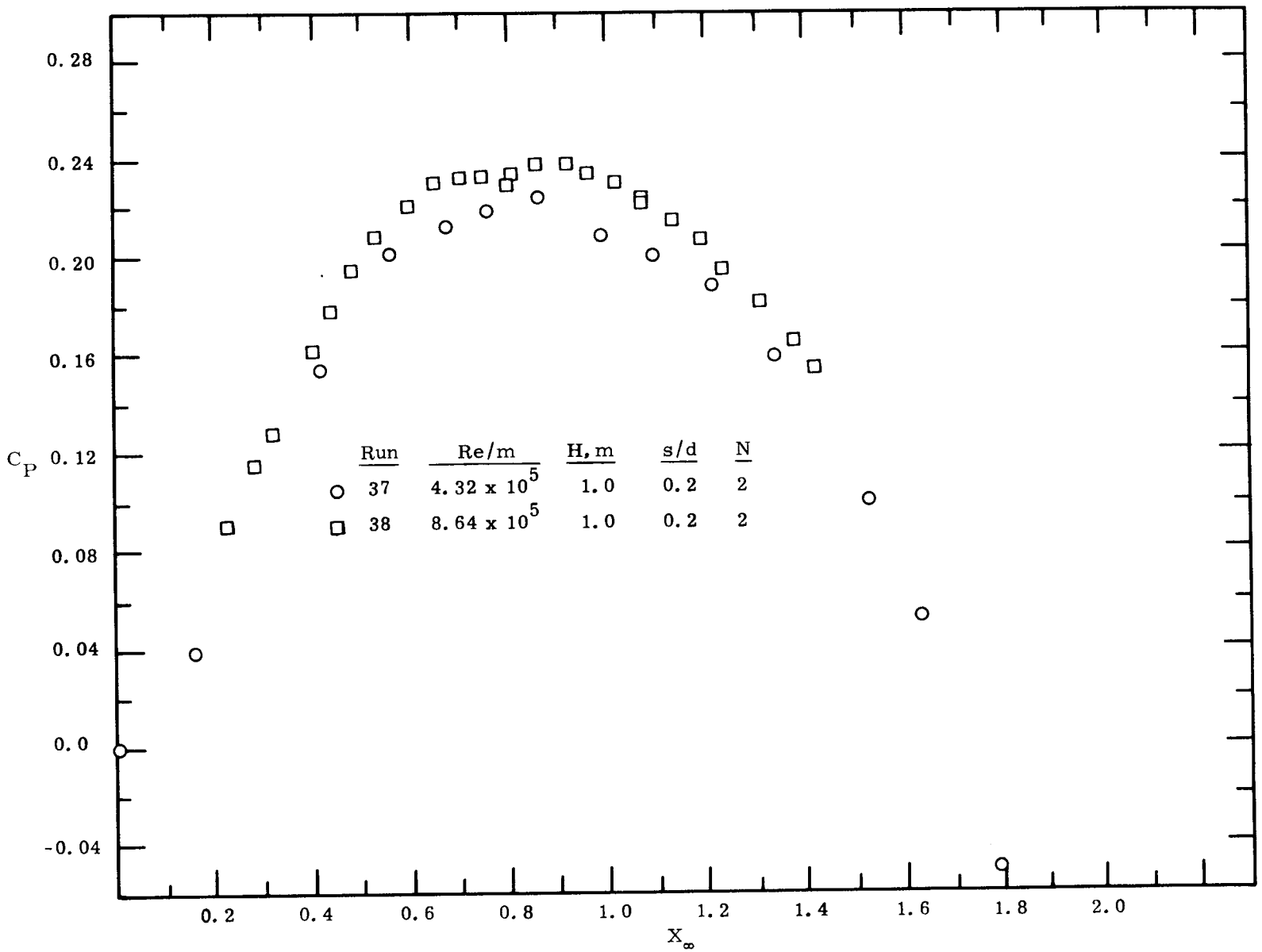
0.28
0.24
0.20
0.16
0.12
0.08
0.04
0.0
-0.04
C_P
0.2
0.4
0.6
0.8
1.0
1.2
1.4
1.6
1.8
2.0
X_∞
Run Re/m H, m s/d N
37 4.32 x 10^5 1.0 0.2 2
38 8.64 x 10^5 1.0 0.2 2

(a)

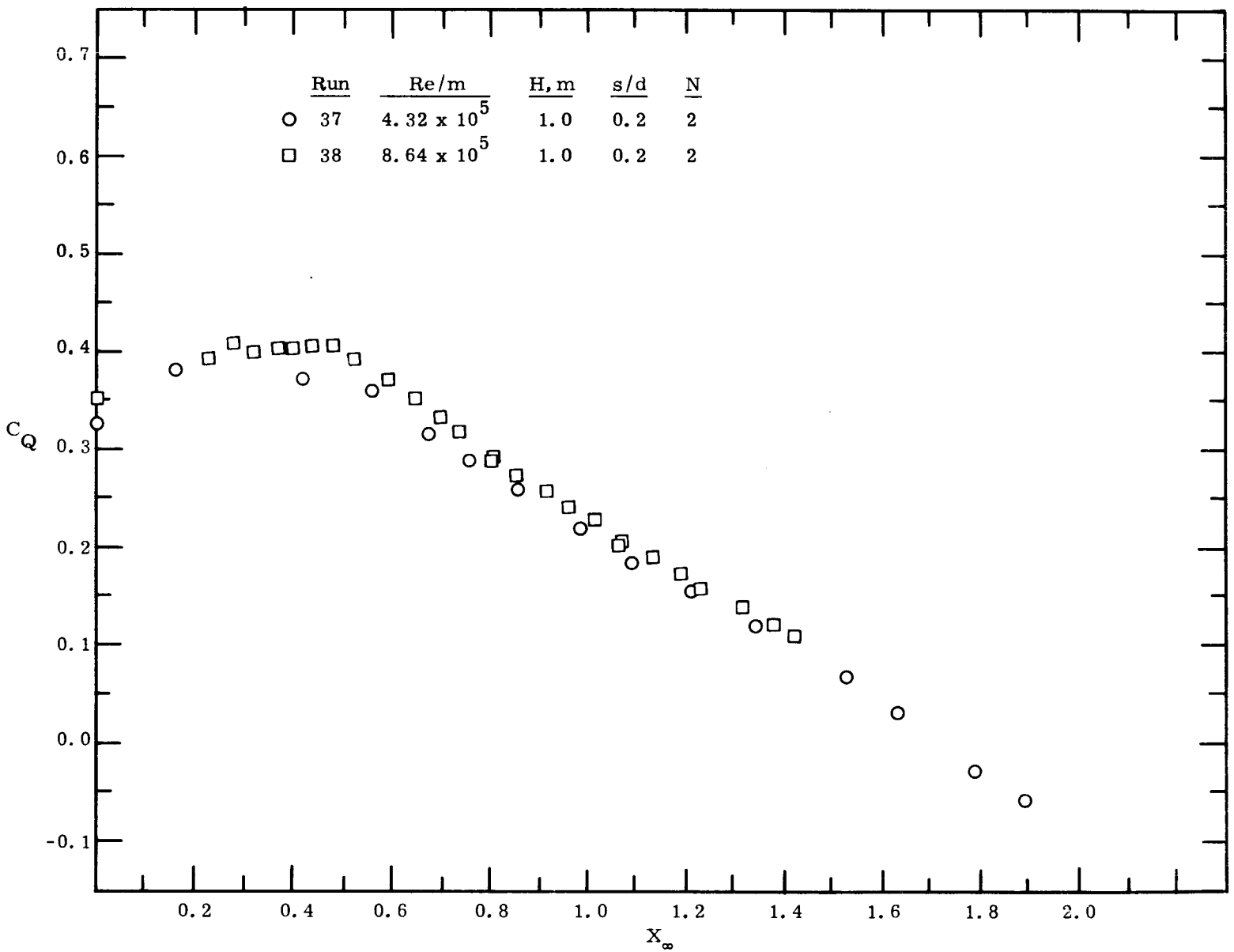

(b)

Figure 17. Power and torque coefficients as a function of speed ratio for a two-bucket Savonius rotor (Configuration 13) with a gap width ratio of 0.20 for Re/m of 4.32×10^5 and 8.64×10^5.

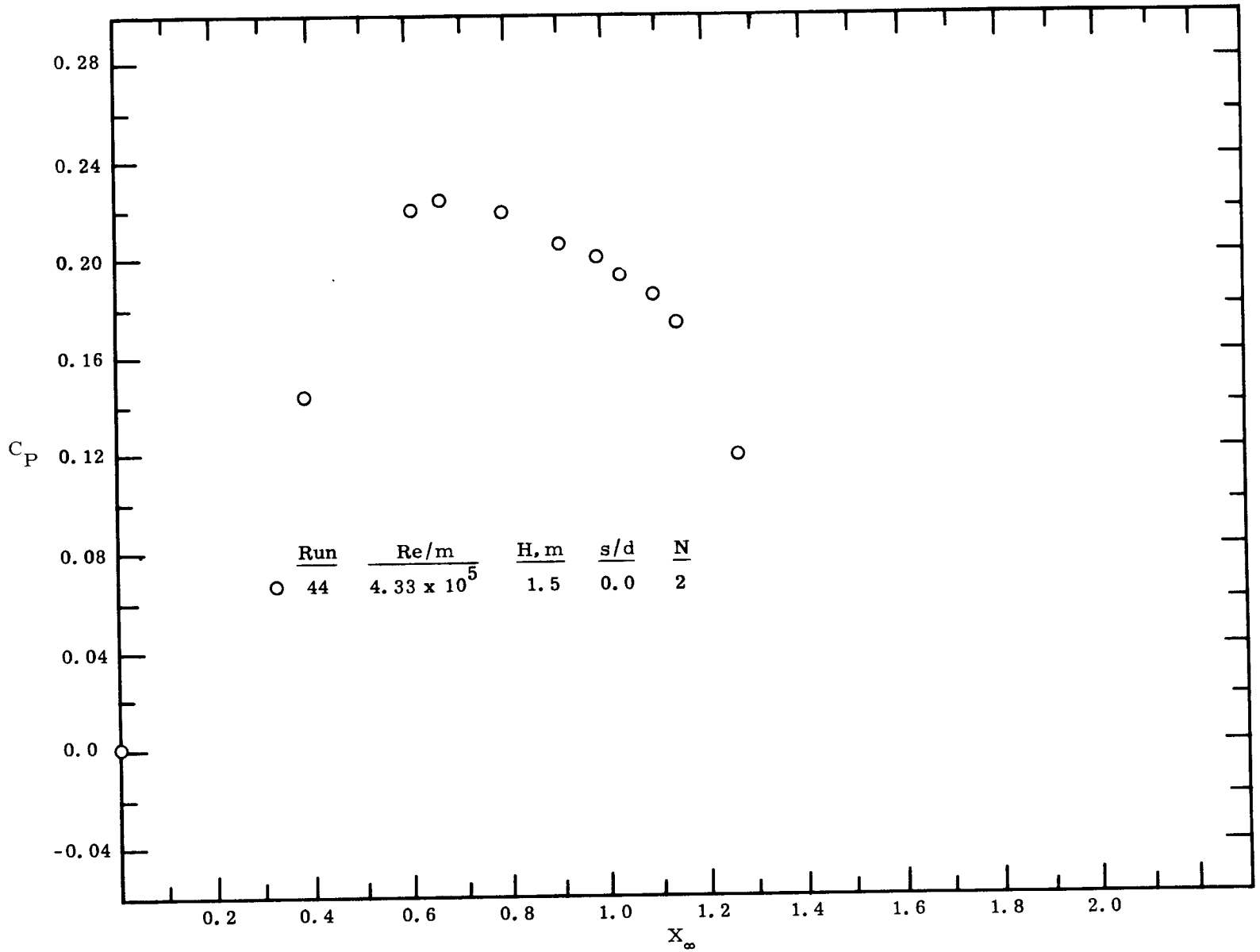
0.28
0.24
0.20
0.16
C_P 0.12
0.08
0.04
0.0
-0.04
0.2
0.4
0.6
0.8
1.0
1.2
1.4
1.6
1.8
2.0
X_∞
Run Re/m H, m s/d N
44 4.33 x 10^5 1.5 0.0 2

(a)

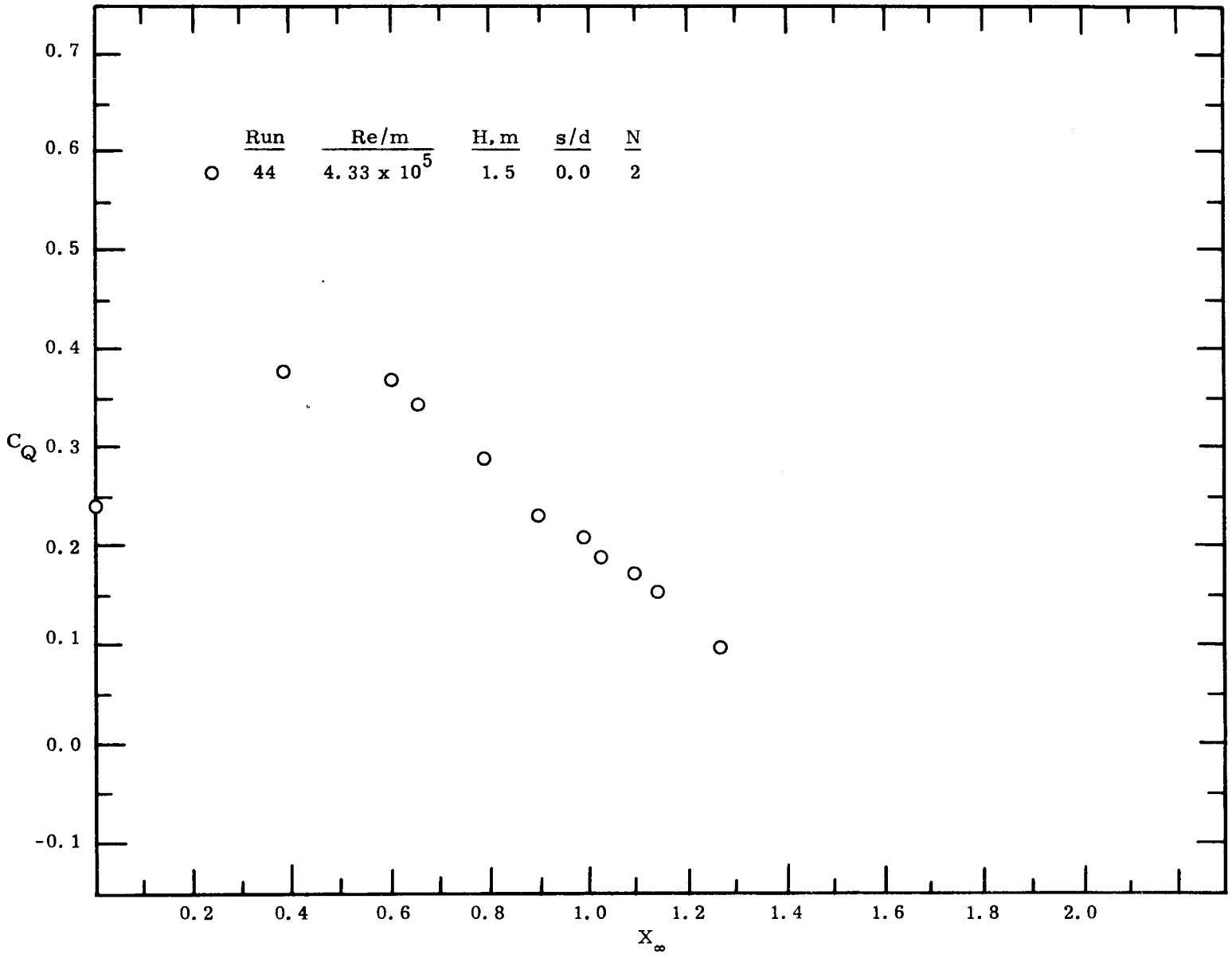

(b)

Figure 18. Power and torque coefficients as a function of speed ratio for a two-bucket Savonius rotor (Configuration 15) with a gap width ratio of 0.0 for Re/m of 4.33×10^5.

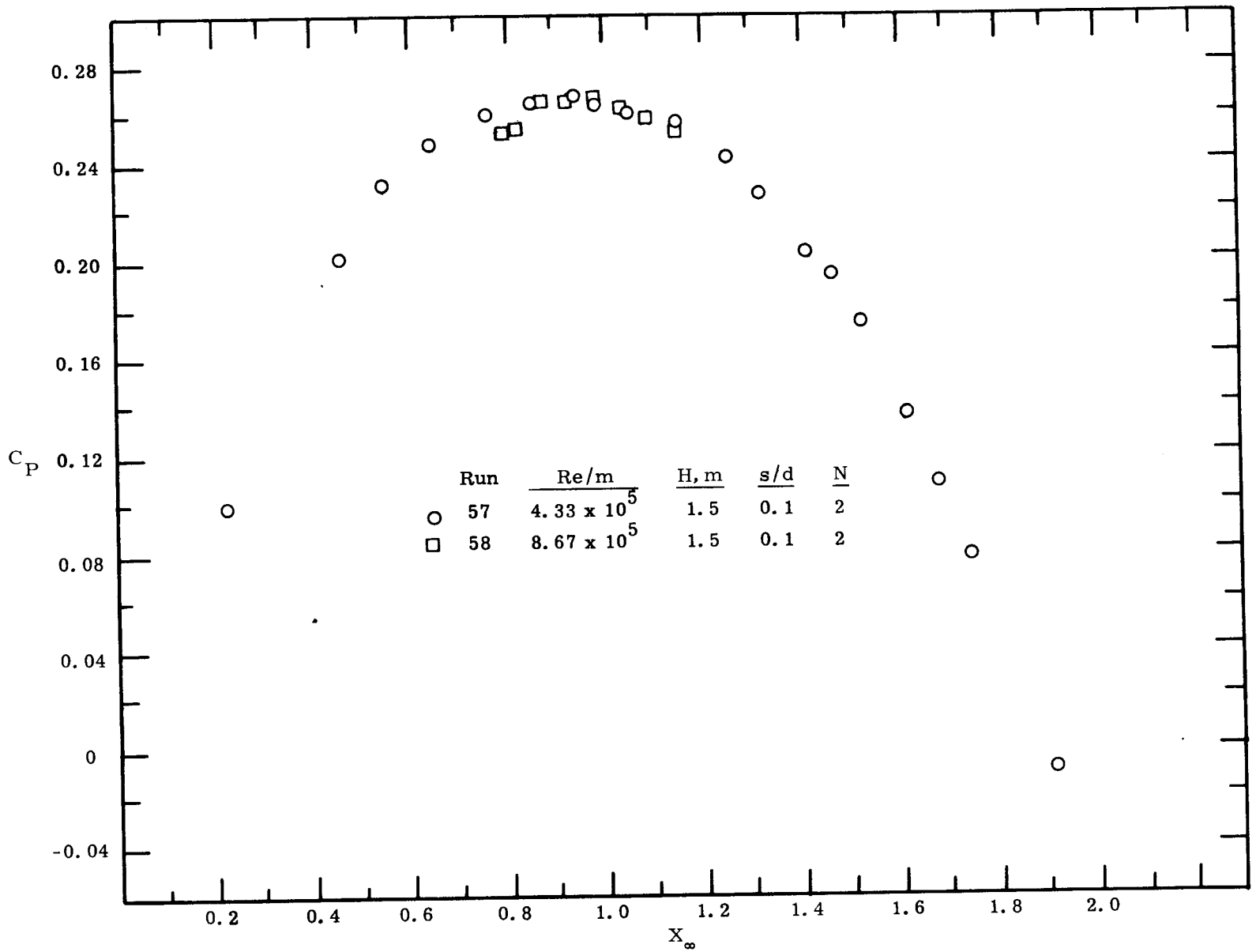
0.28
0.24
0.20
0.16
0.12
0.08
0.04
0
-0.04
C_P
0.2
0.4
0.6
0.8
1.0
1.2
1.4
1.6
1.8
2.0
X_∞
Run Re/m H, m s/d N
57 4.33 x 10^5 1.5 0.1 2
58 8.67 x 10^5 1.5 0.1 2

(a)

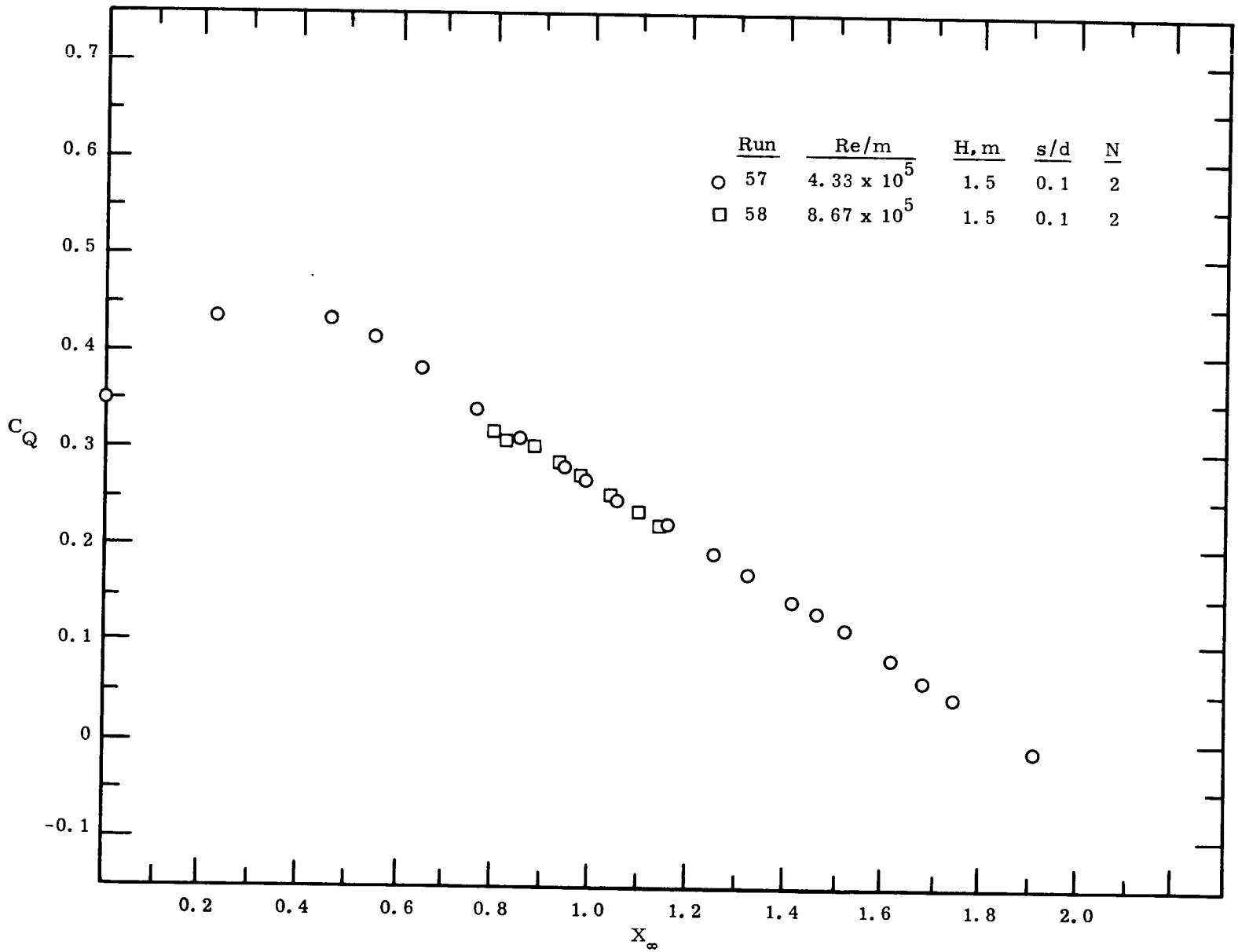

(b)

Figure 19. Power and torque coefficients as a function of speed ratio for a two-bucket Savonius rotor (Configuration 19) with a gap width ratio of 0.10 for Re/m of 4.33×10^5 and 8.67×10^5.

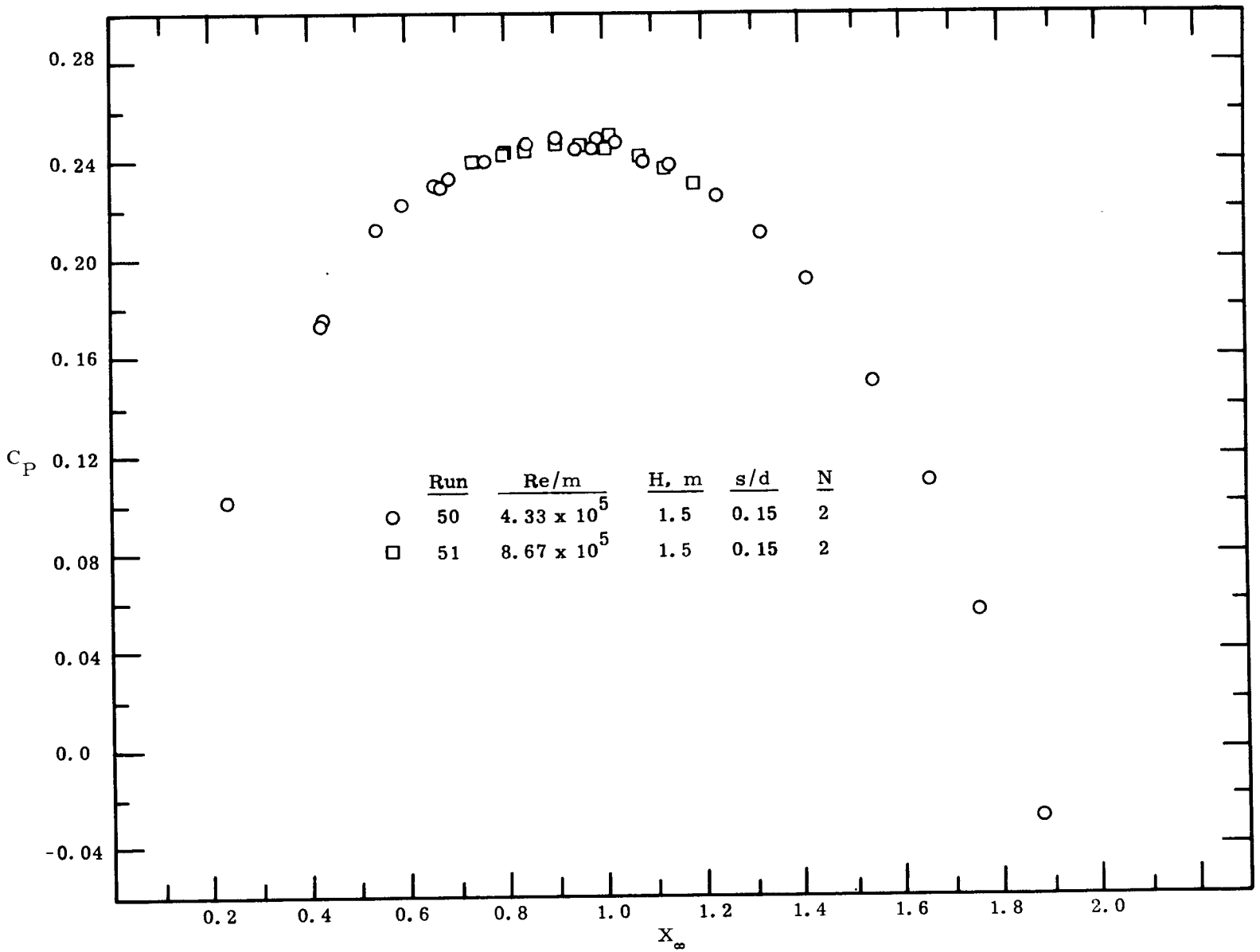
0.28
0.24
0.20
0.16
0.12
0.08
0.04
0.0
-0.04
C_P
0.2
0.4
0.6
0.8
1.0
1.2
1.4
1.6
1.8
2.0
X_∞
Run
Re/m
H, m
s/d
N
50
4.33 x 10^5
1.5
0.15
2
51
8.67 x 10^5
1.5
0.15
2

(a)

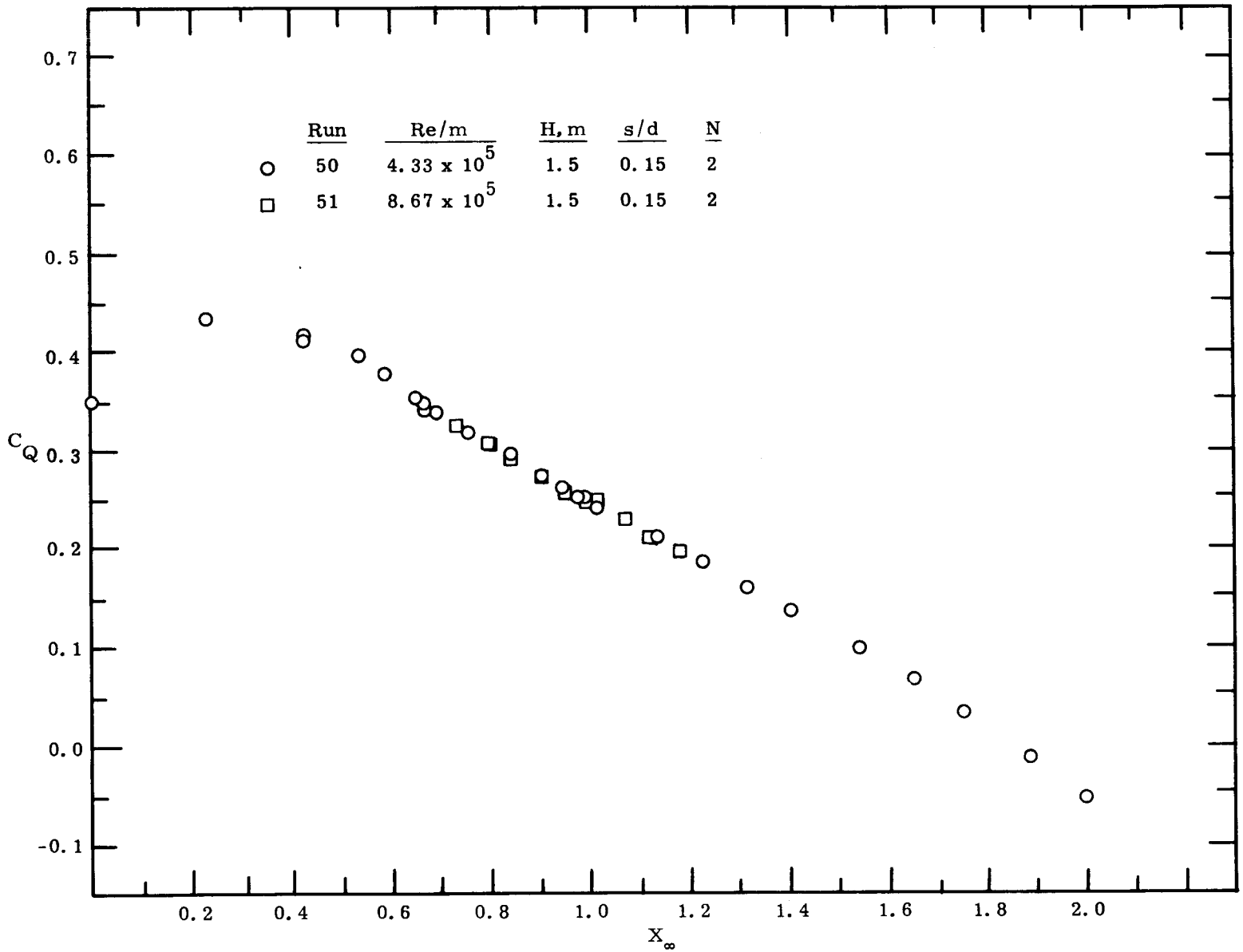

(b)

Figure 20. Power and torque coefficients as a function of speed ratio for a two-bucket Savonius rotor (Configuration 17) with a gap width ratio of 0.15 for Re/m of 4.33×10^5 and 8.67×10^5.

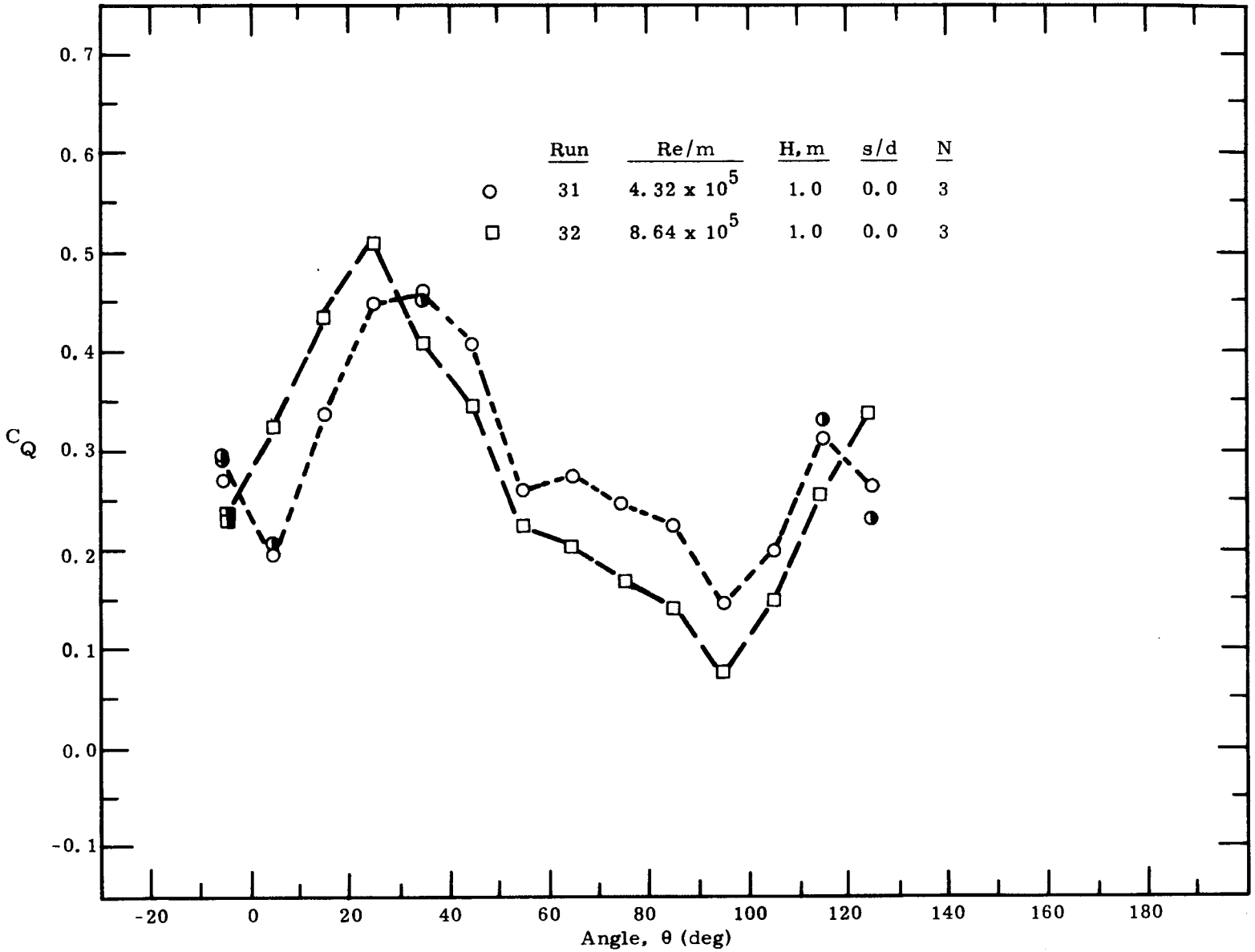

Figure 21. The static torque coefficient as a function of angular position for a three-bucket Savonius rotor (Configuration 12) with a gap width ratio of 0.0 for Re/m of 4.32×10^5 and 8.64×10^5.

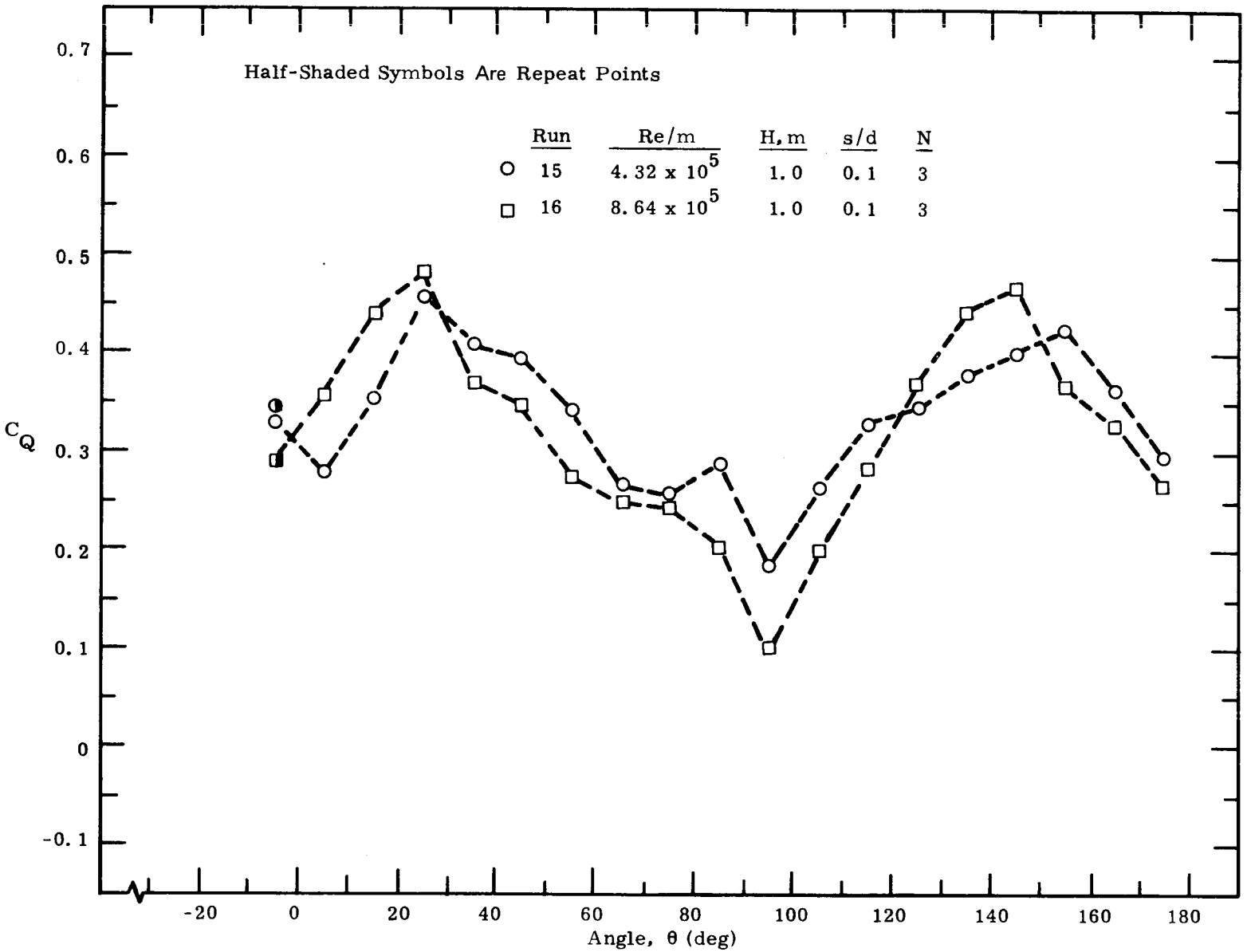

Figure 22. The static torque coefficient as a function of angular position for a three-bucket Savonius rotor (Configuration 8) with a gap width ratio of 0.10 for Re/m of 4.32×10^5 and 8.64×10^5.

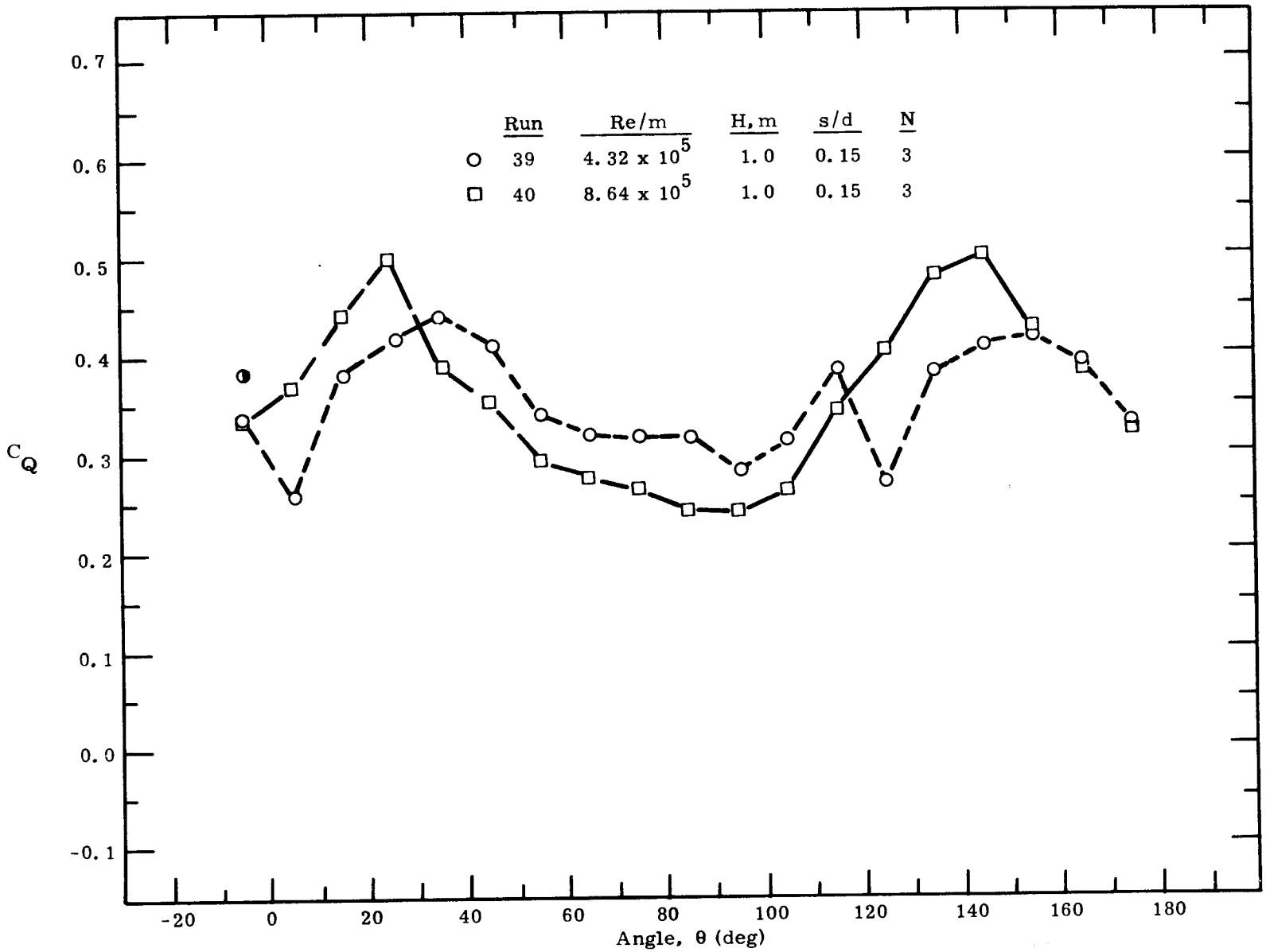

Figure 23. The static torque coefficient as a function of angular position for a three-bucket Savonius rotor (Configuration 14) with a gap width ratio of 0.15 for Re/m of 4.32×10^5 and 8.64×10^5.

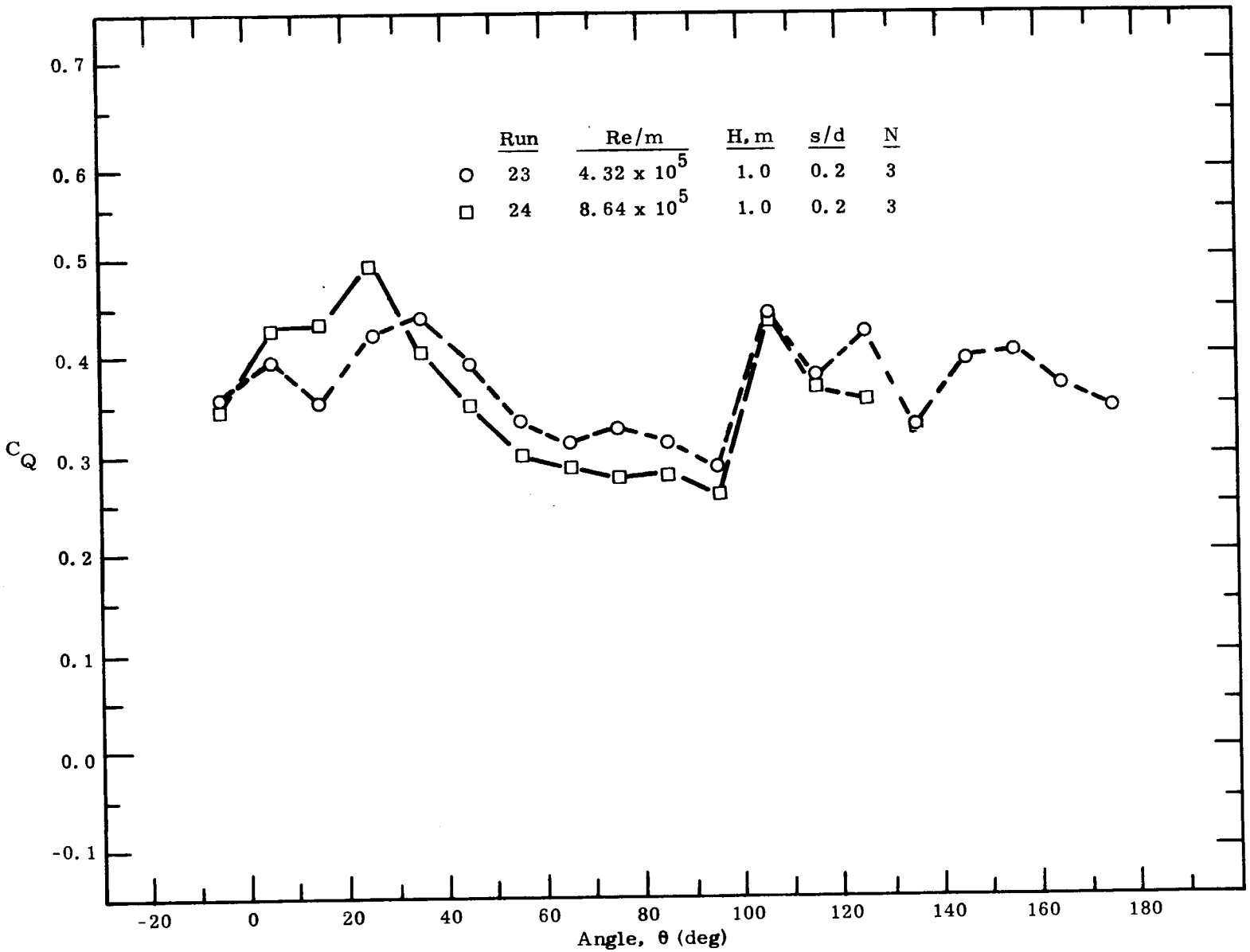

Figure 24. The static torque coefficient as a function of angular position for a three-bucket Savonius rotor (Configuration 10) with a gap width ratio of 0.20 for Re/m of 4.32×10^5 and 8.64×10^5.

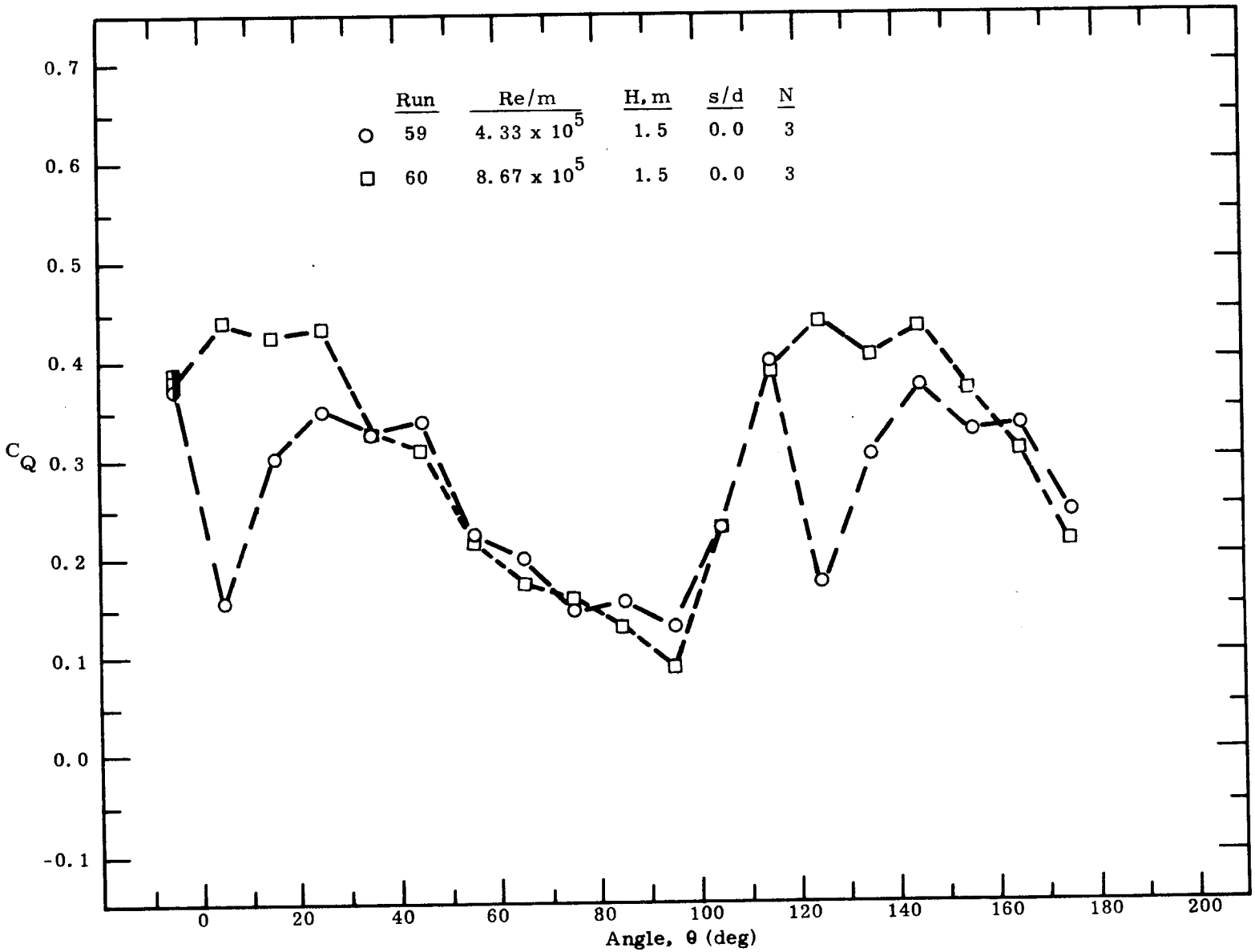

Figure 25. The static torque coefficient as a function of angular position for a three-bucket Savonius rotor (Configuration 20) with a gap width ratio of 0.0 for Re/m of 4.33×10^5 x 8.67×10^5.

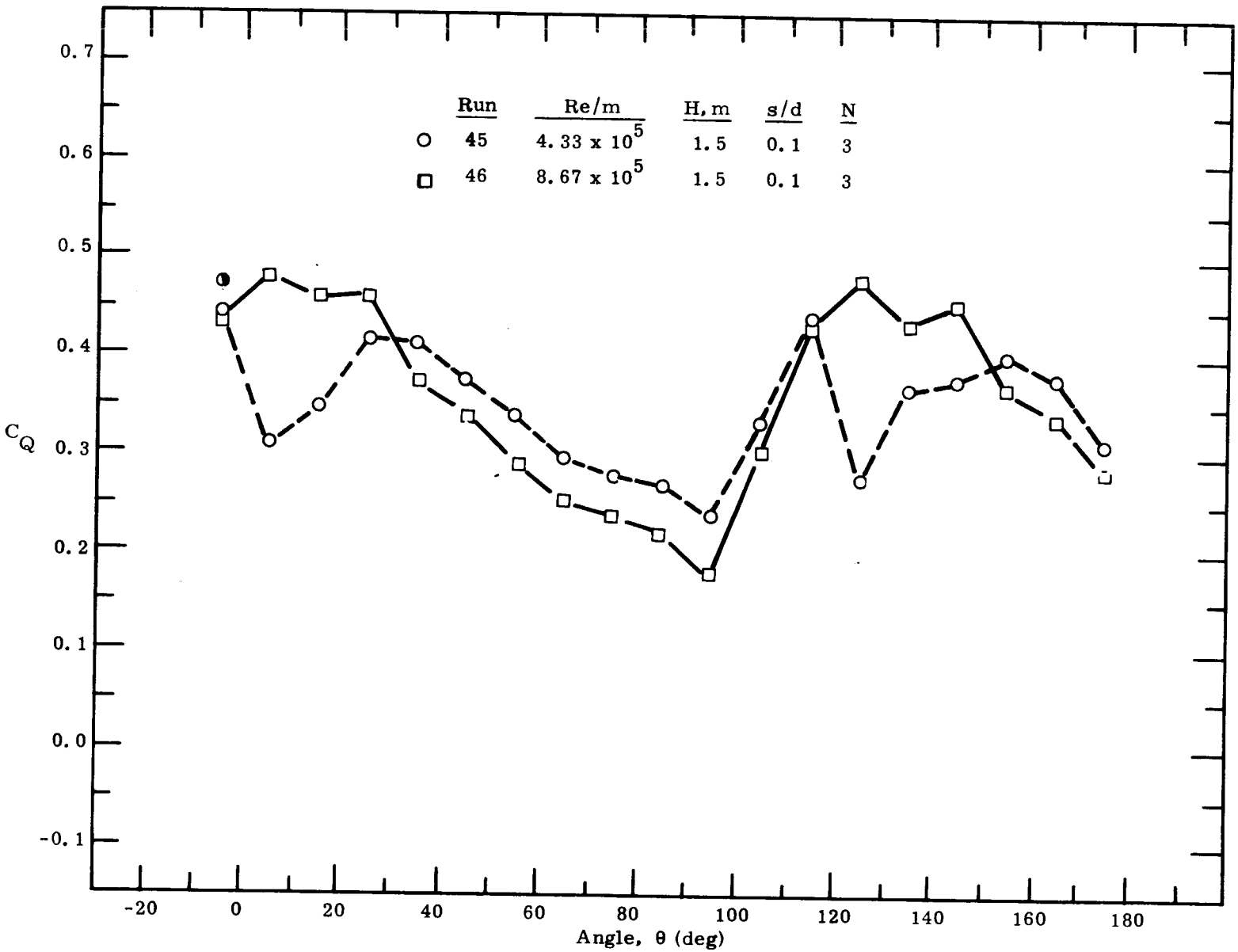

Figure 26. The static torque coefficient as a function of angular position for a three-bucket Savonius rotor (Configuration 16) with a gap width ratio of 0.10 for Re/m of 4.33×10^5 and 8.67×10^5.

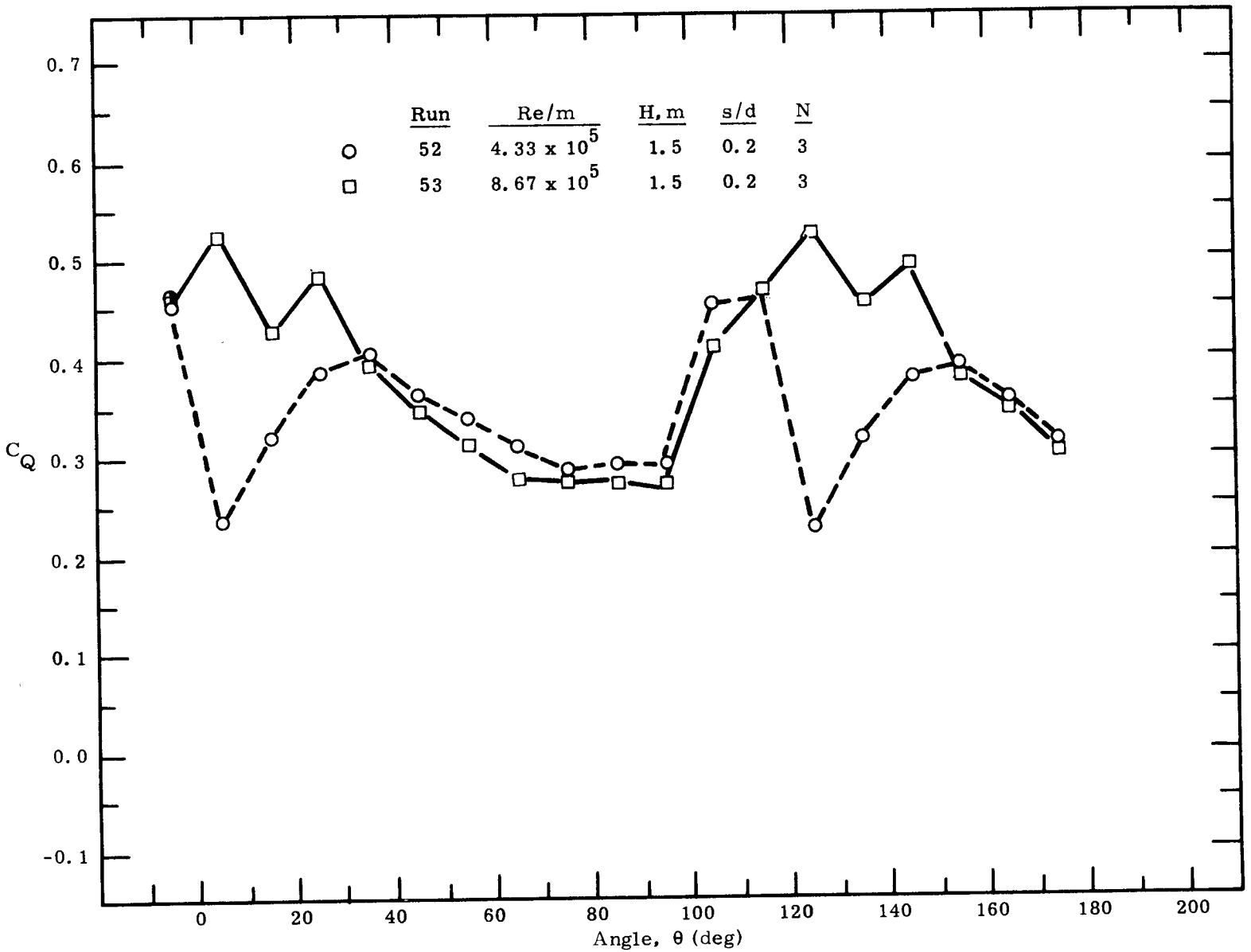

Figure 27. The static torque coefficient as a function of angular position for a three-bucket Savonius rotor (Configuration 18) with a gap width ratio of 0.20 for Re/m of 4.33×10^5 and 8.67×10^5.

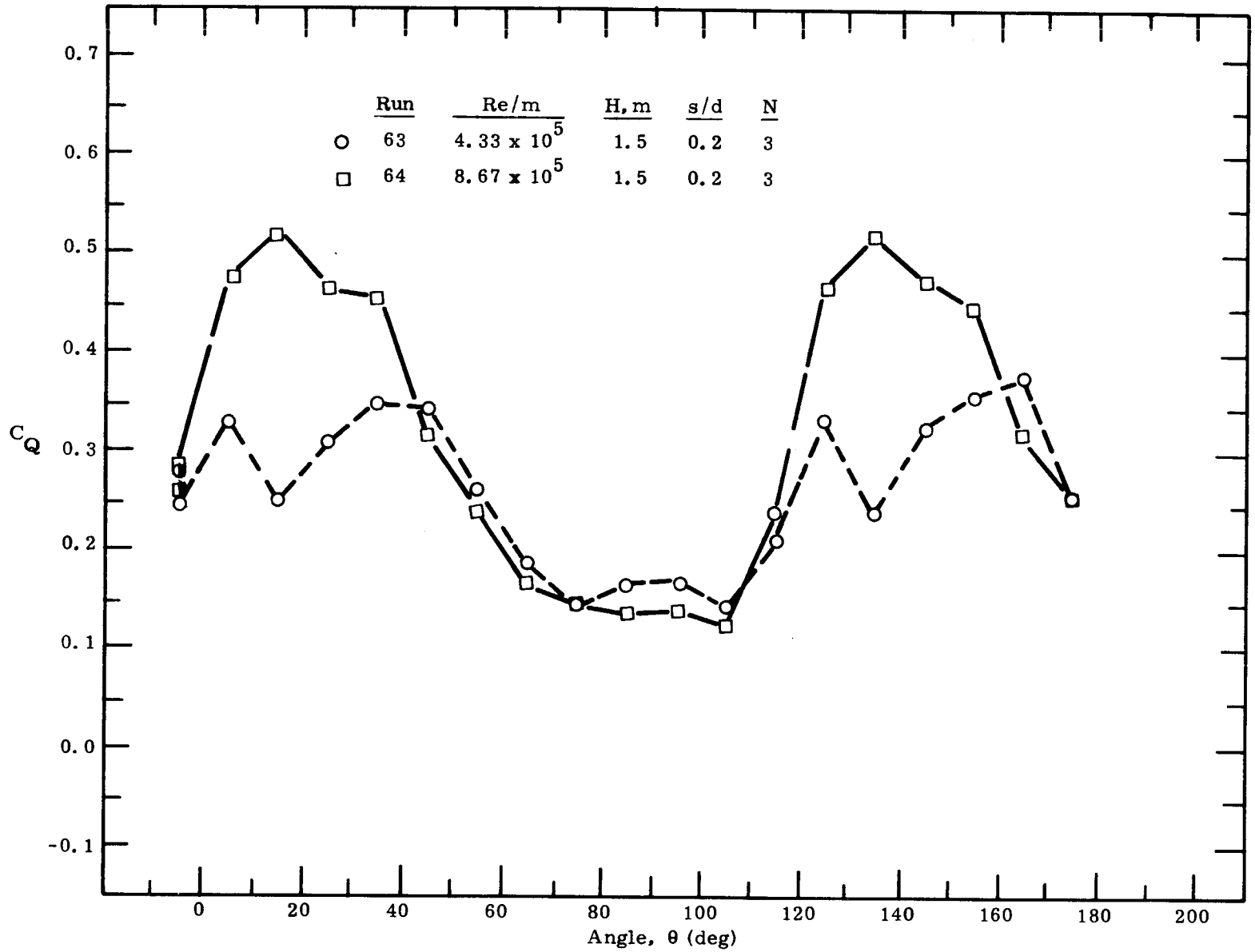

Figure 28. The static torque coefficient as a function of angular position for a three-bucket Savonius rotor (Configuration 21) with a gap width ratio of 0.2 for Re/m of 4.33×10^5 and 8.67×10^5 (180° buckets).

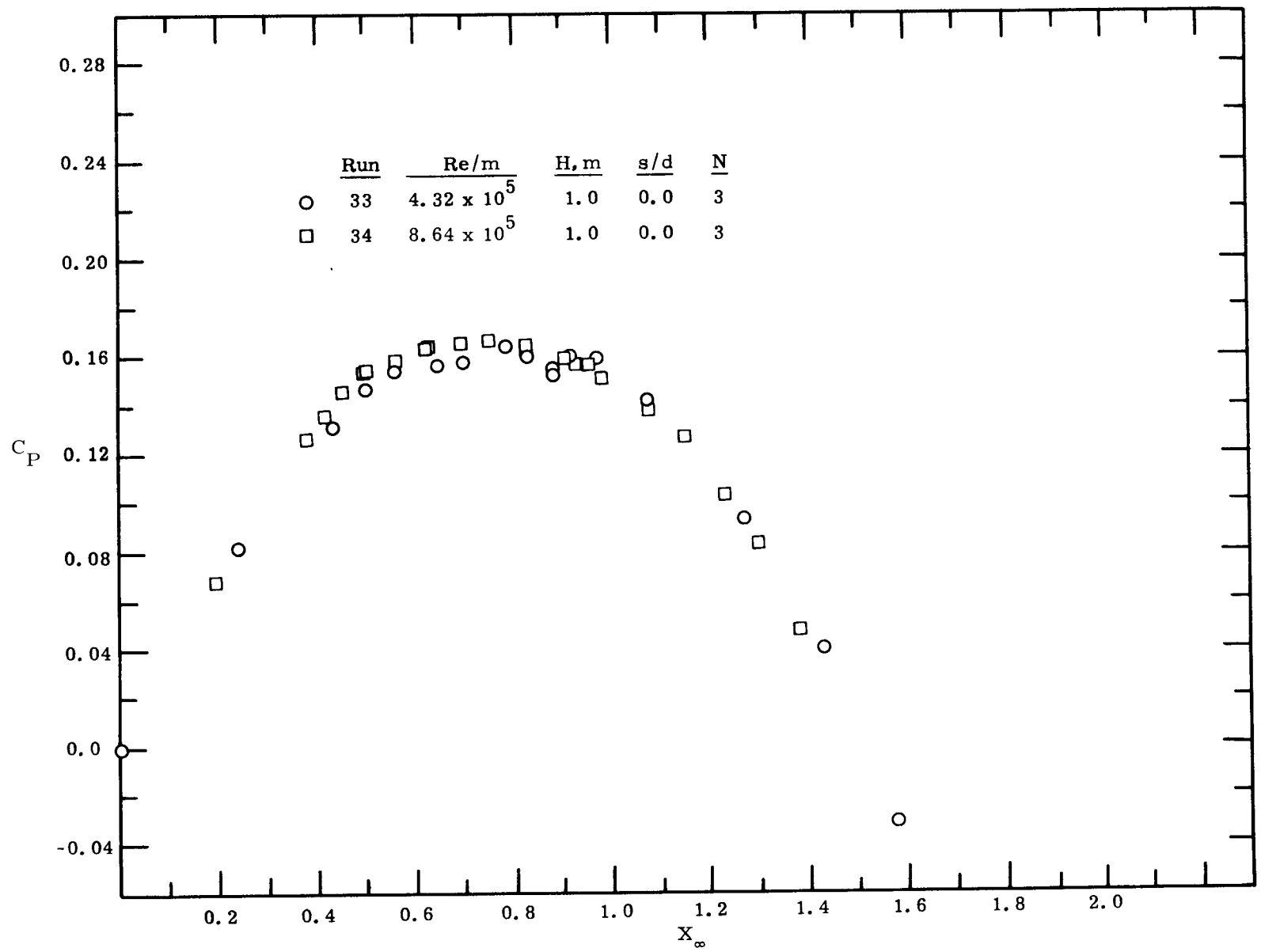
Run Re/m H, m s/d N
33 4.32 x 10^5 1.0 0.0 3
34 8.64 x 10^5 1.0 0.0 3
0.28
0.24
0.20
0.16
0.12
0.08
0.04
0.0
-0.04
C_P
0.2
0.4
0.6
0.8
1.0
1.2
1.4
1.6
1.8
2.0
X_∞

(a)

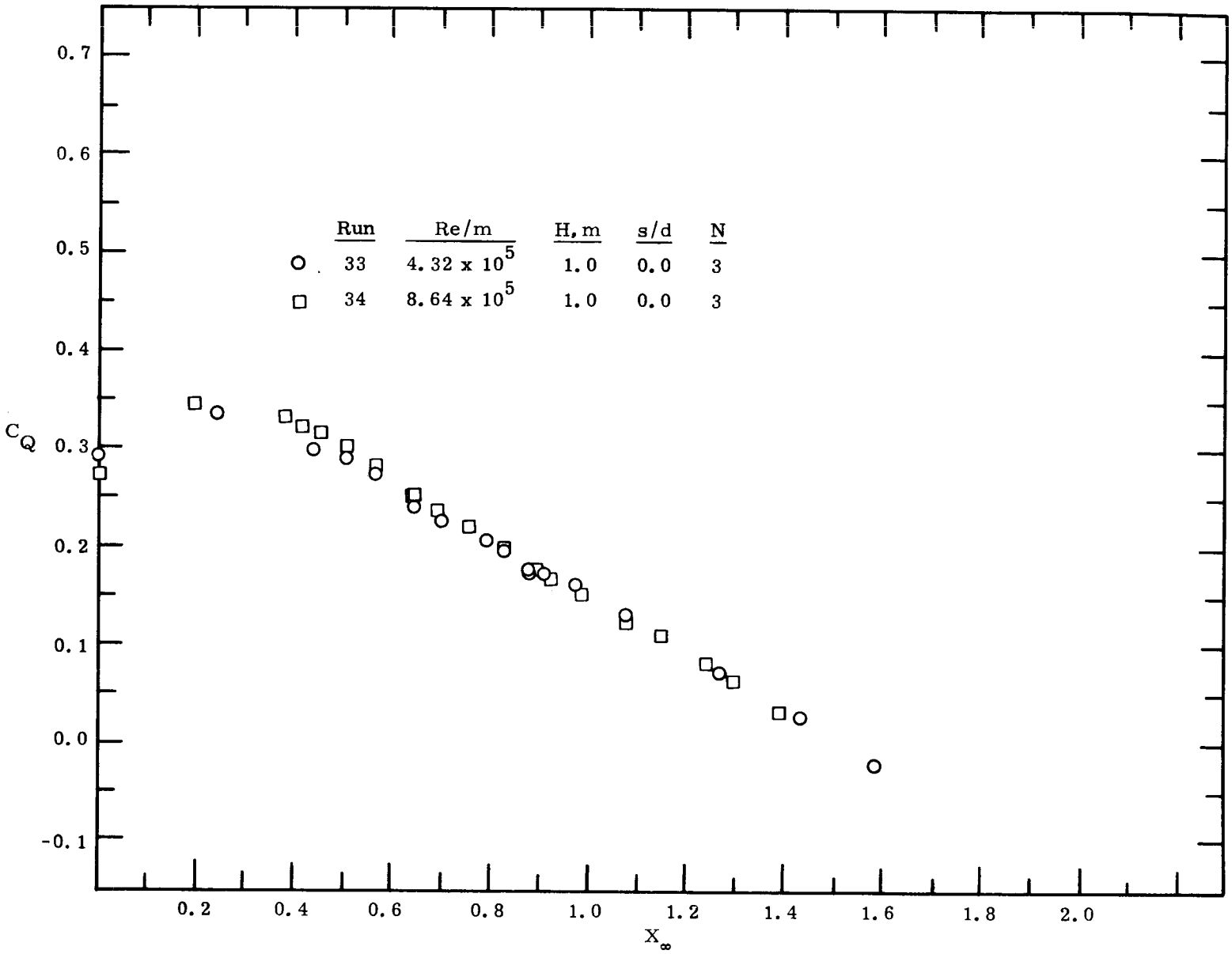

(b)

Figure 29. Power and torque coefficients as a function of speed ratio for a three-bucket Savonius rotor (Configuration 12) with a gap width ratio of 0.0 for Re/m of 4.32×10^5 and 8.64×10^5.

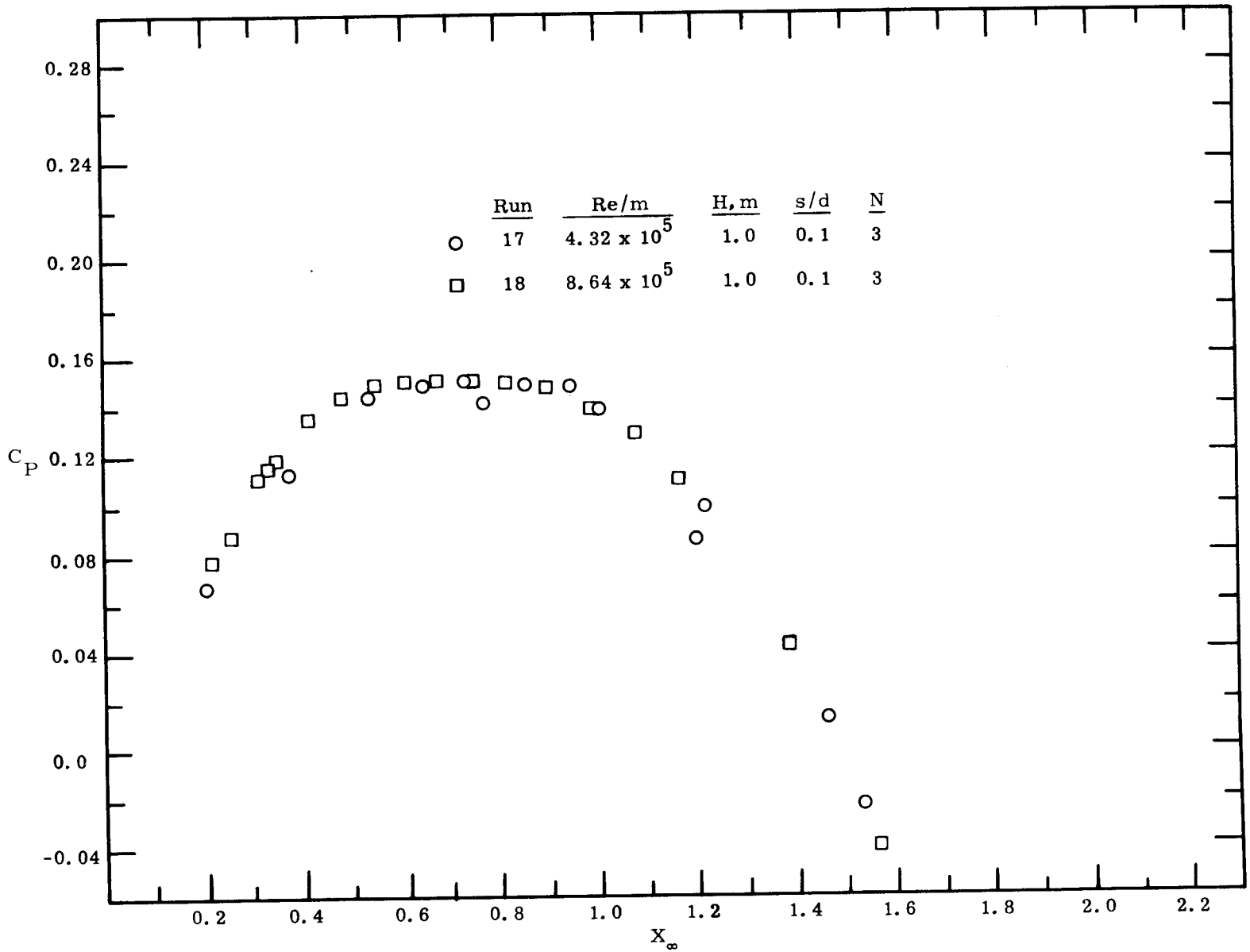
Run
Re/m
H, m
s/d
N
17
4.32 x 10^5
1.0
0.1
3
18
8.64 x 10^5
1.0
0.1
3
0.28
0.24
0.20
0.16
0.12
0.08
0.04
0.0
-0.04
C_P
0.2
0.4
0.6
0.8
1.0
1.2
1.4
1.6
1.8
2.0
2.2
X_∞

(a)

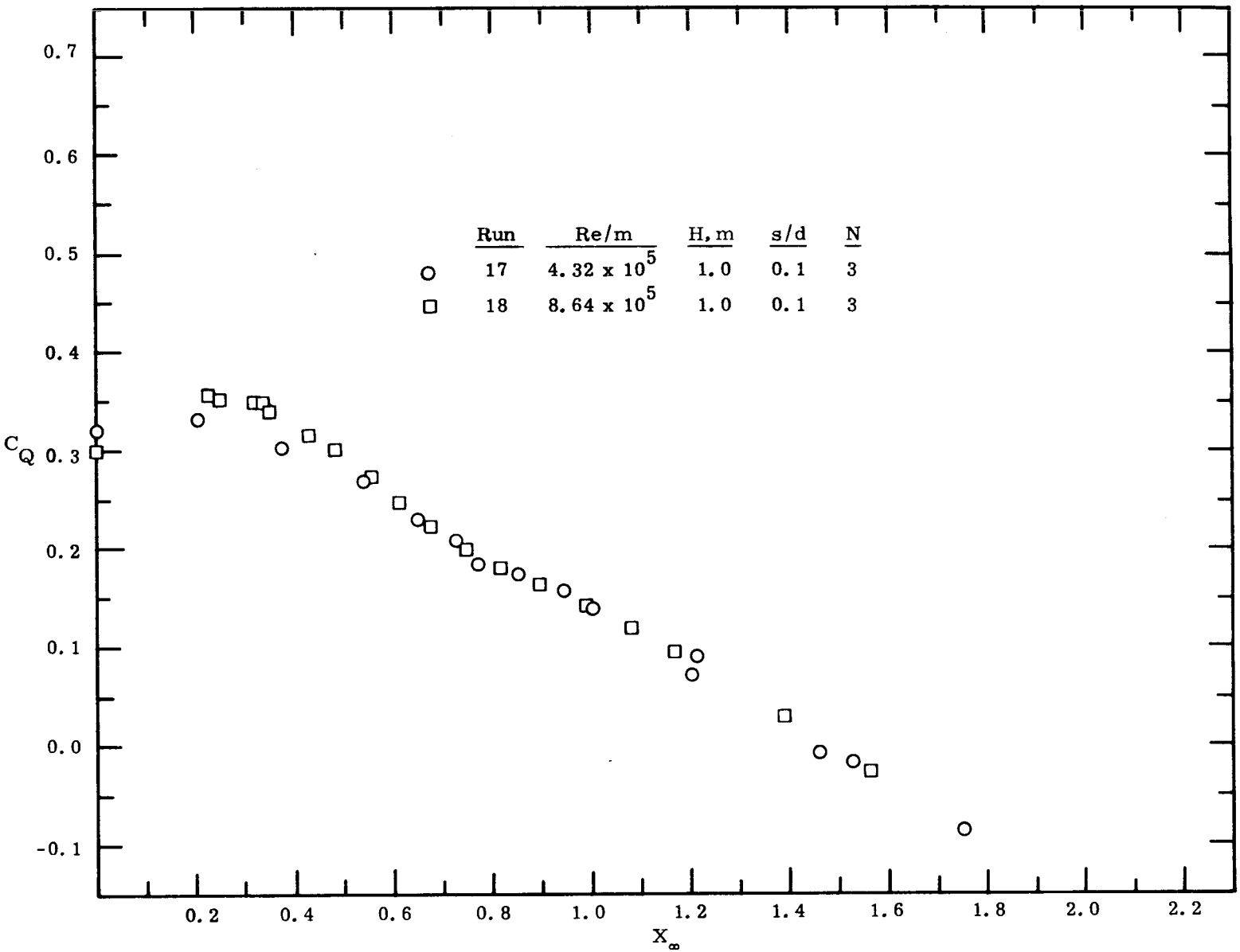

(b)

Figure 30. Power and torque coefficients as a function of speed ratio for a three-bucket Savonius rotor (Configuration 8) with a gap width ratio of 0.10 for Re/m of 4.32×10^5 and 8.64×10^5.

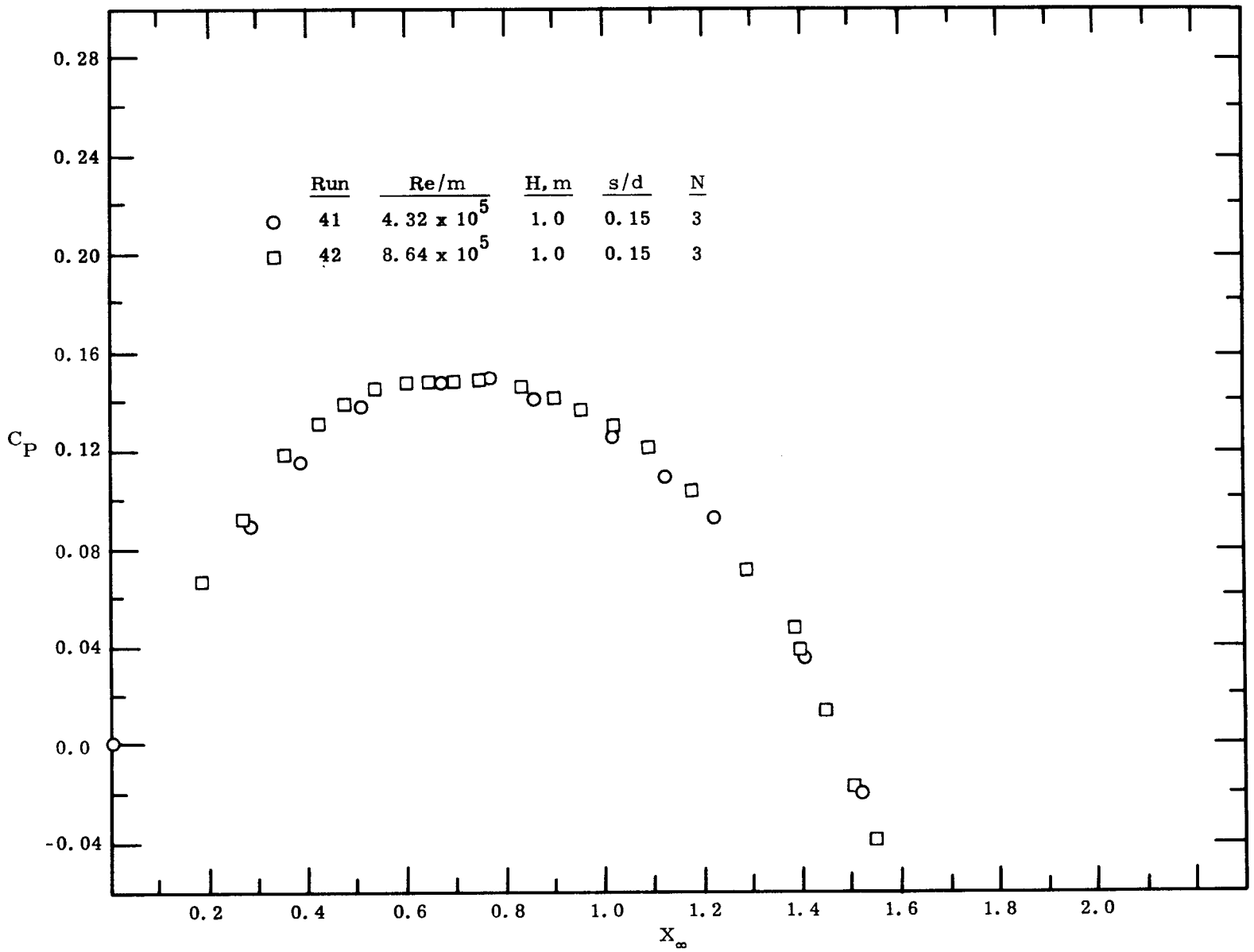
0.28
0.24
0.20
0.16
0.12
0.08
0.04
0.0
-0.04
C_P
Run Re/m H, m s/d N
41 4.32 x 10^5 1.0 0.15 3
42 8.64 x 10^5 1.0 0.15 3
0.2
0.4
0.6
0.8
1.0
1.2
1.4
1.6
1.8
2.0
X_∞

(a)

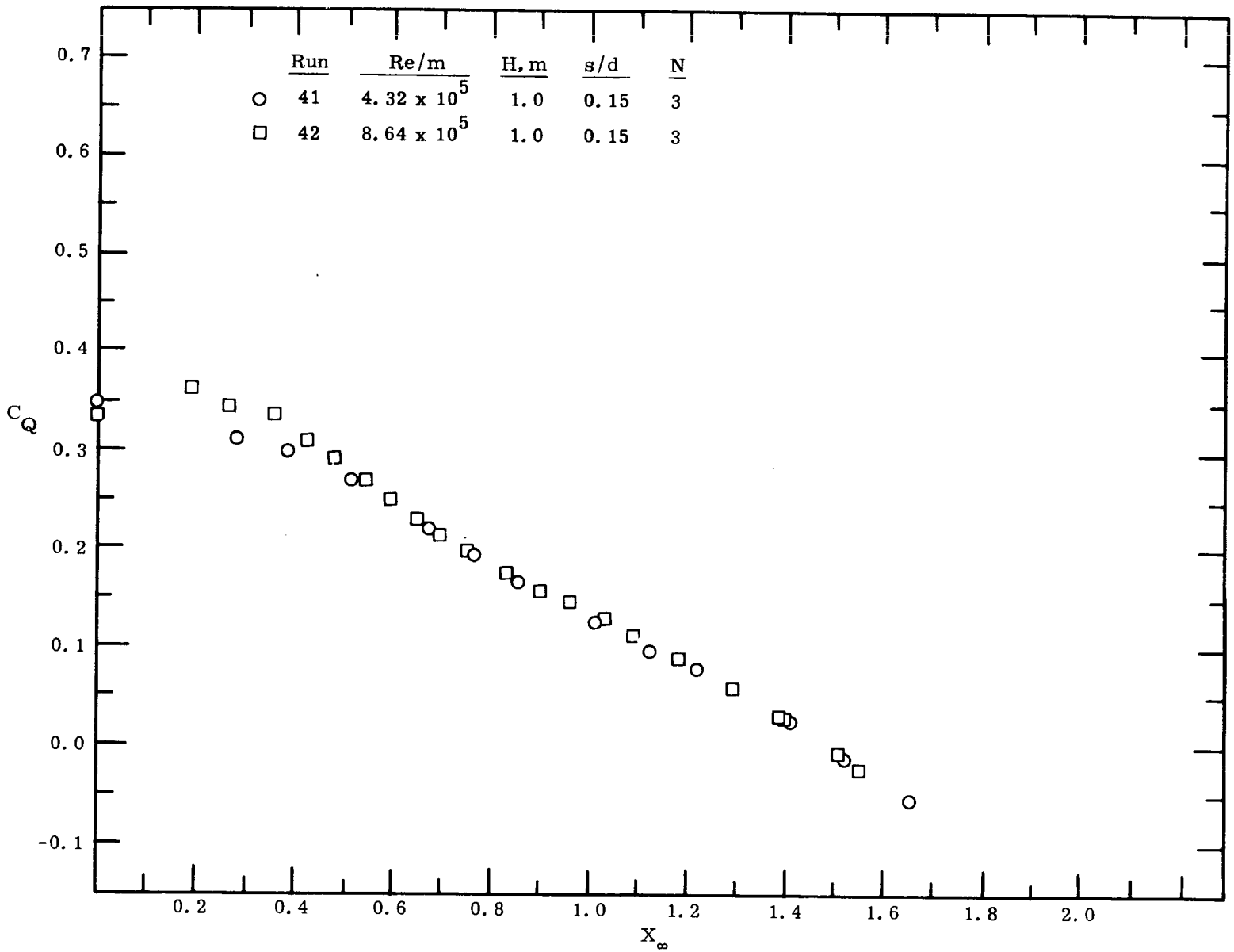

(b)

Figure 31. Power and torque coefficients as a function of speed ratio for a three-bucket Savonius rotor (Configuration 14) with a gap width ratio of 0.15 for Re/m of 4.32×10^5 and 8.64×10^5.

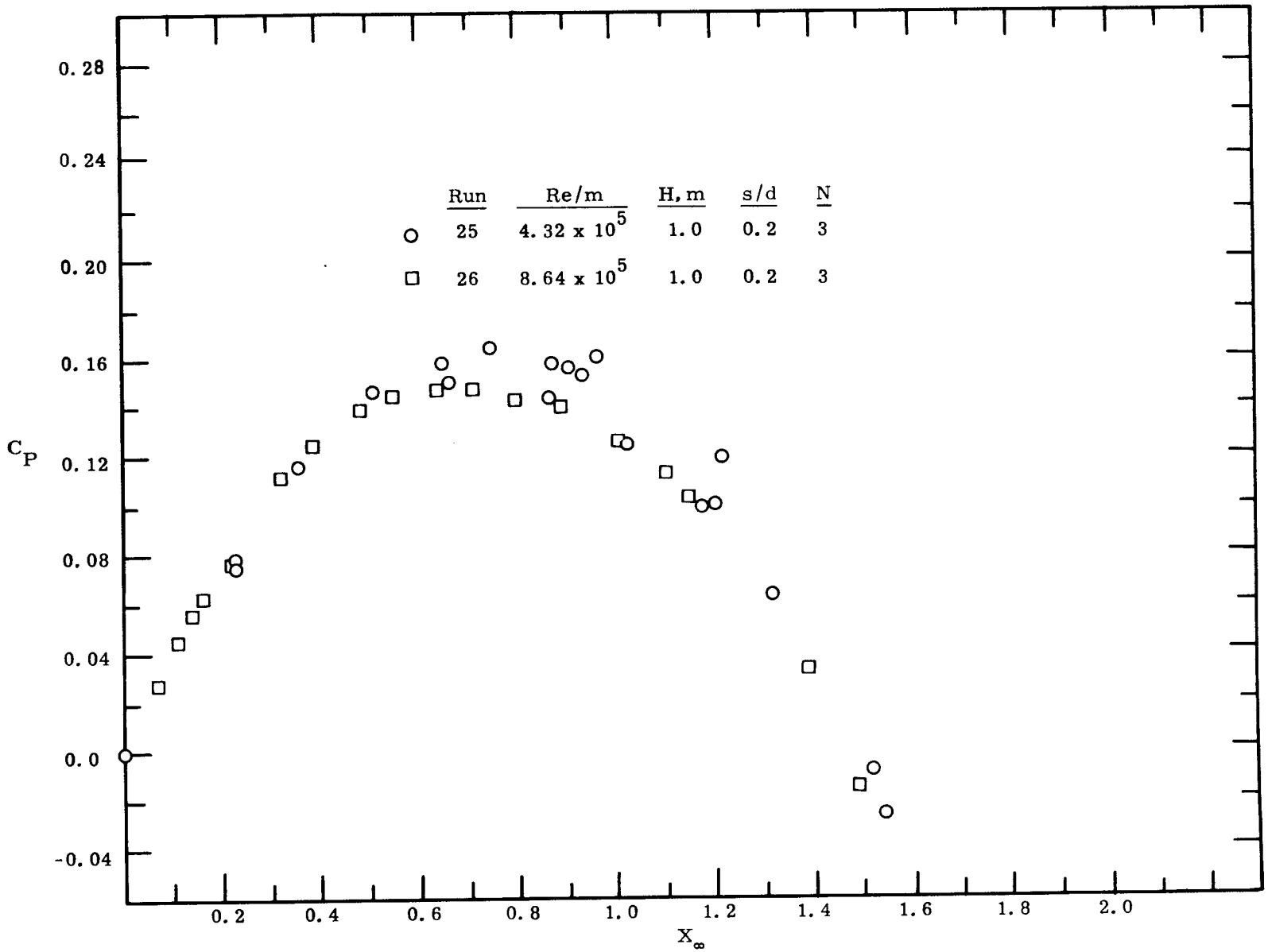
Run
Re/m
H, m
s/d
N
25
4.32 x 10^5
1.0
0.2
3
26
8.64 x 10^5
1.0
0.2
3
C_P
0.28
0.24
0.20
0.16
0.12
0.08
0.04
0.0
-0.04
0.2
0.4
0.6
0.8
1.0
1.2
1.4
1.6
1.8
2.0
X_∞

(a)

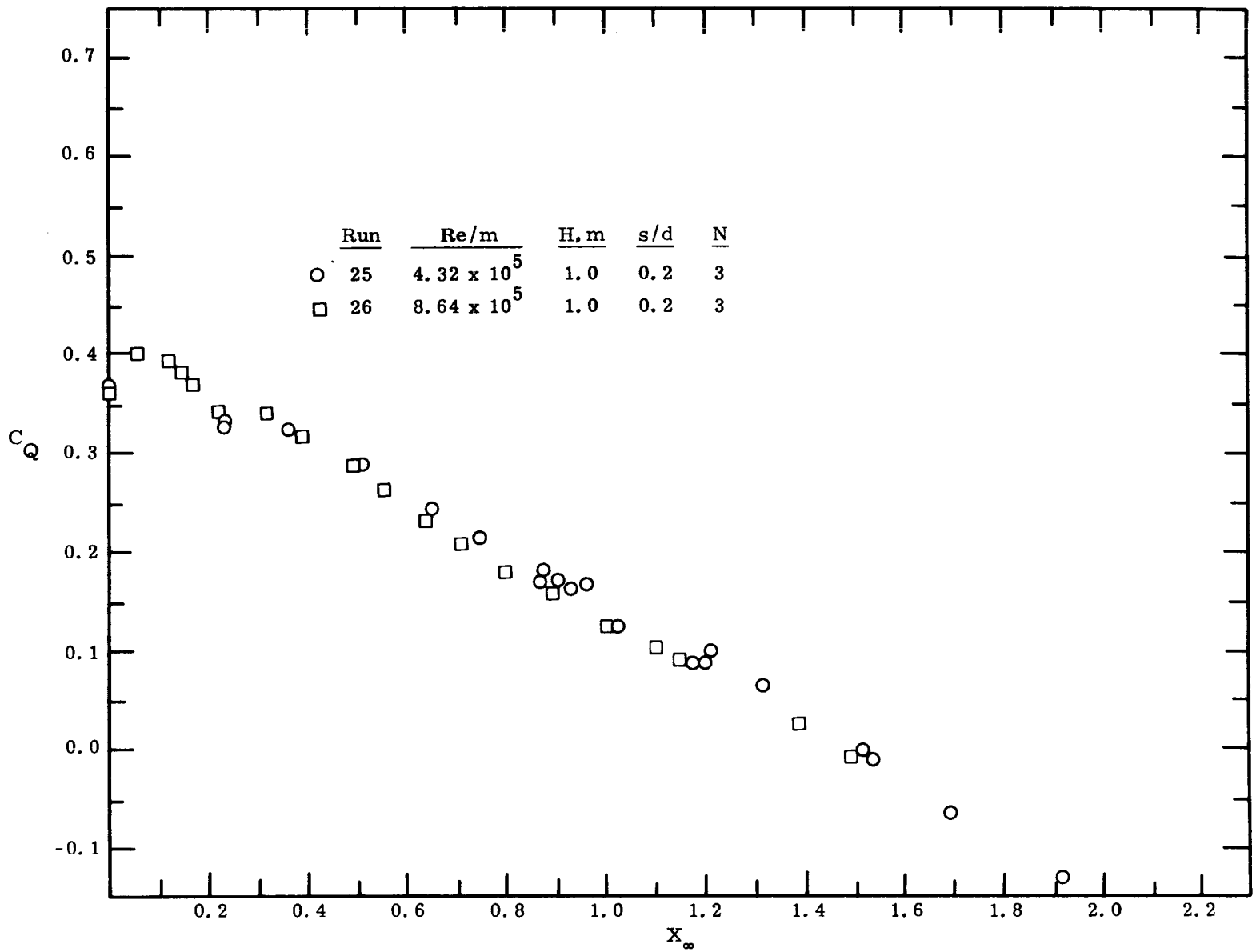

(b)

Figure 32. Power and torque coefficients as a function of speed ratio for a three-bucket Savonius rotor (Configuration 10) with a gap width ratio of 0.20 for Re/m of 4.32×10^5 and 8.64×10^5.

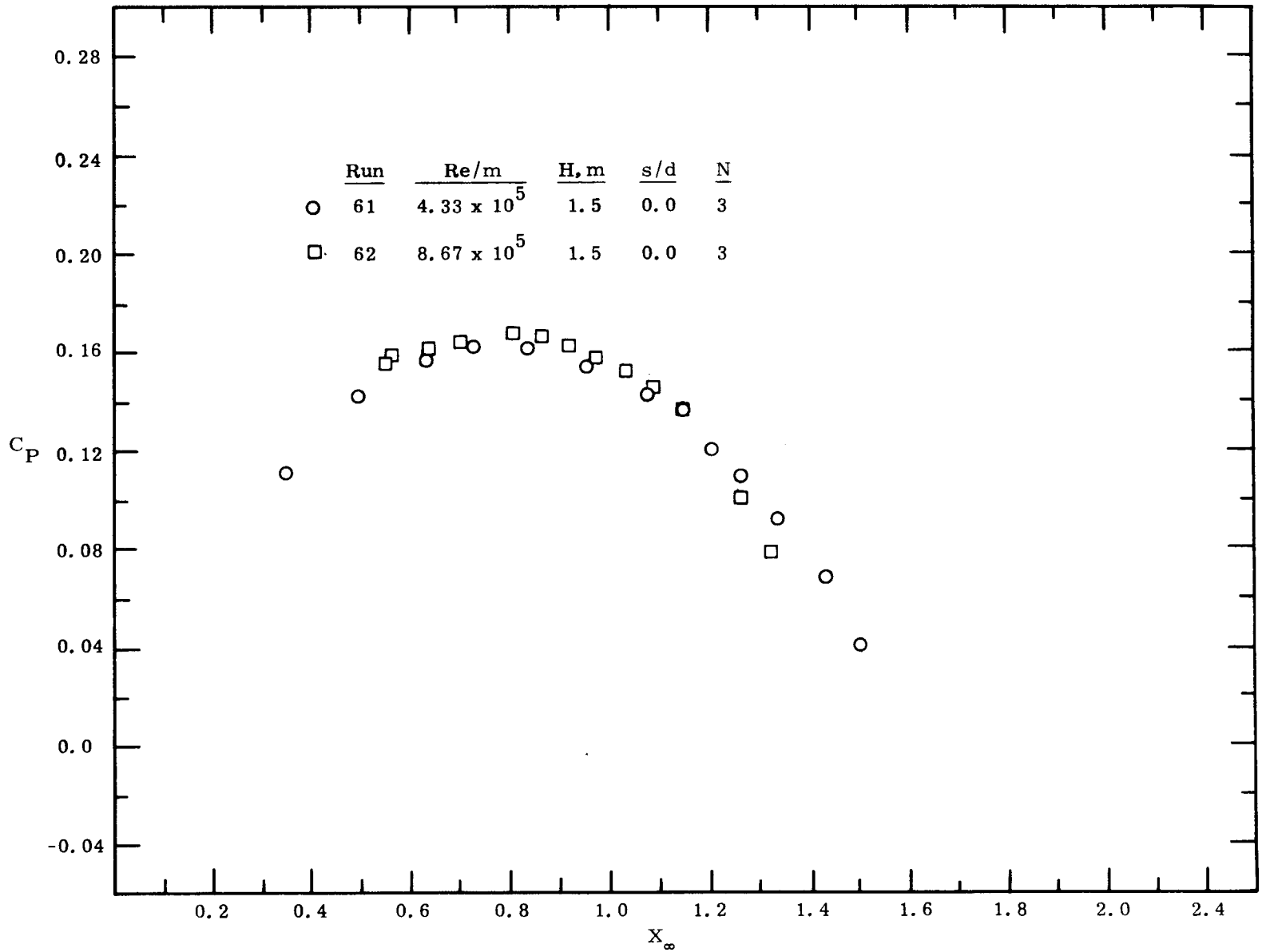
0.28
0.24
0.20
0.16
0.12
0.08
0.04
0.0
-0.04
C_P
Run Re/m H, m s/d N
61 4.33 x 10^5 1.5 0.0 3
62 8.67 x 10^5 1.5 0.0 3
0.2
0.4
0.6
0.8
1.0
1.2
1.4
1.6
1.8
2.0
2.4
X_∞

(a)

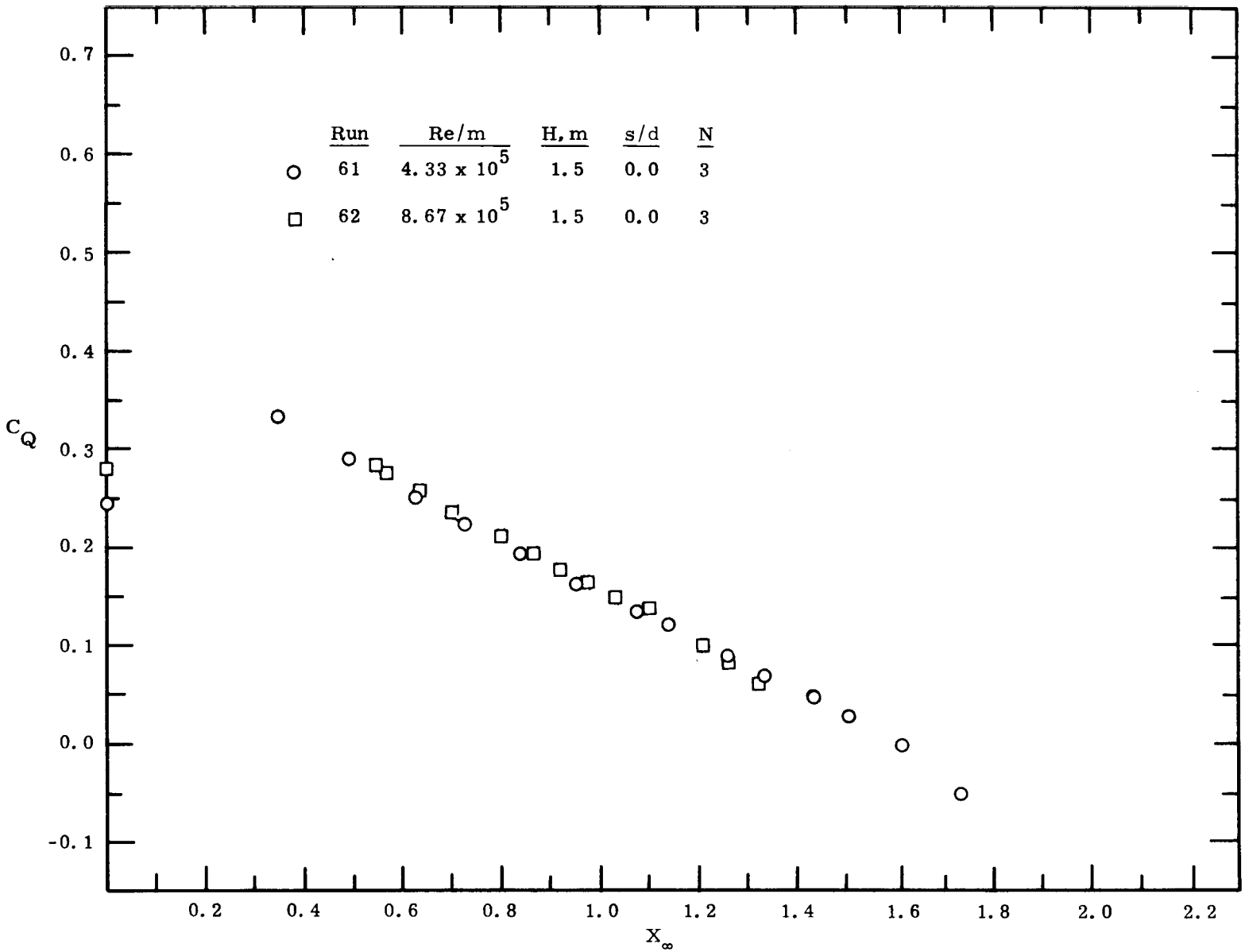

(b)

Figure 33. Power and torque coefficients as a function of speed ratio for a three-bucket Savonius rotor (Configuration 20) with a gap width ratio of 0.0 for Re/m of 4.33×10^5 and 8.67×10^5.

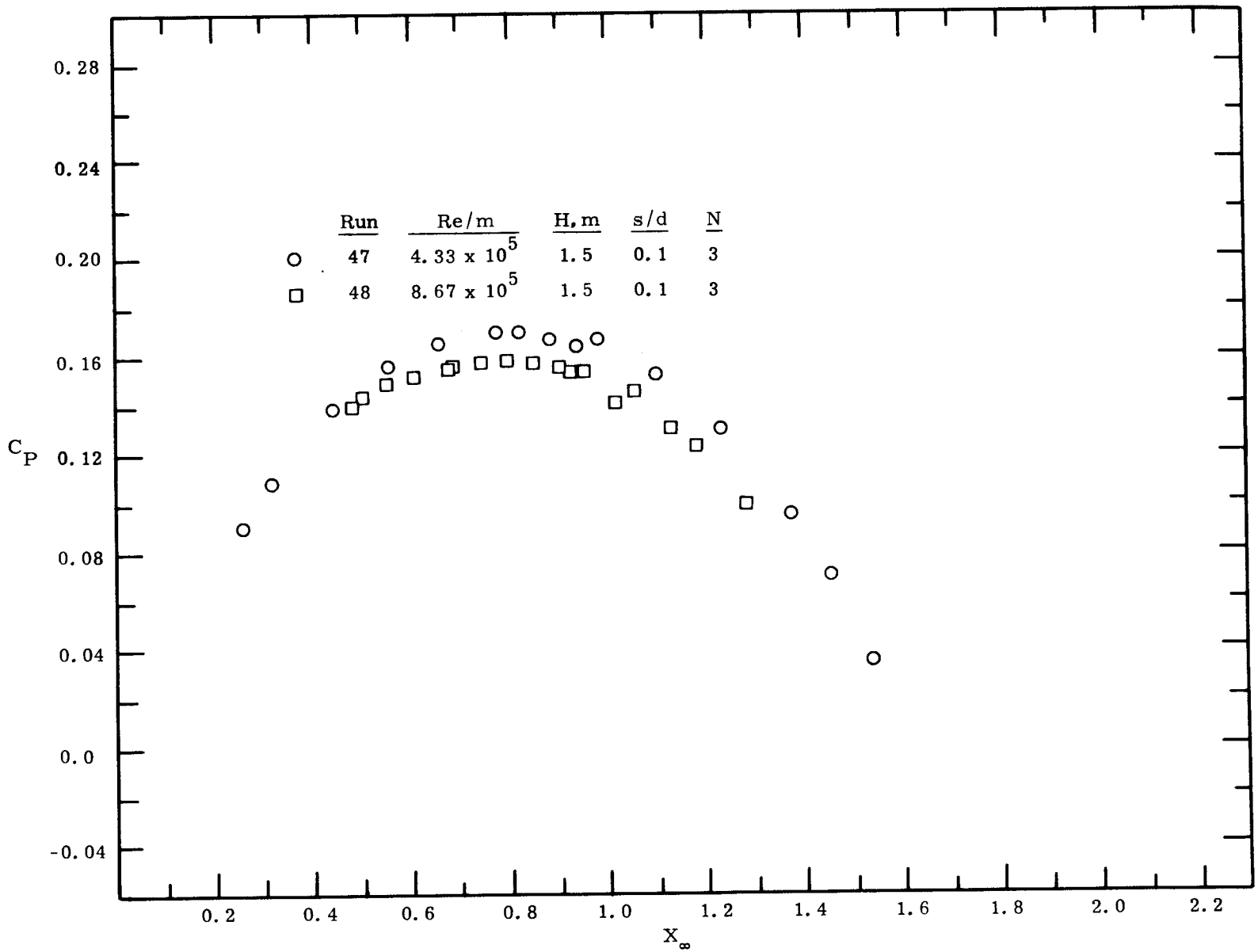
Run
Re/m
H, m
s/d
N
47
4.33 x 10^5
1.5
0.1
3
48
8.67 x 10^5
1.5
0.1
3
C_P
0.28
0.24
0.20
0.16
0.12
0.08
0.04
0.0
-0.04
0.2
0.4
0.6
0.8
1.0
1.2
1.4
1.6
1.8
2.0
2.2
X_∞

(a)

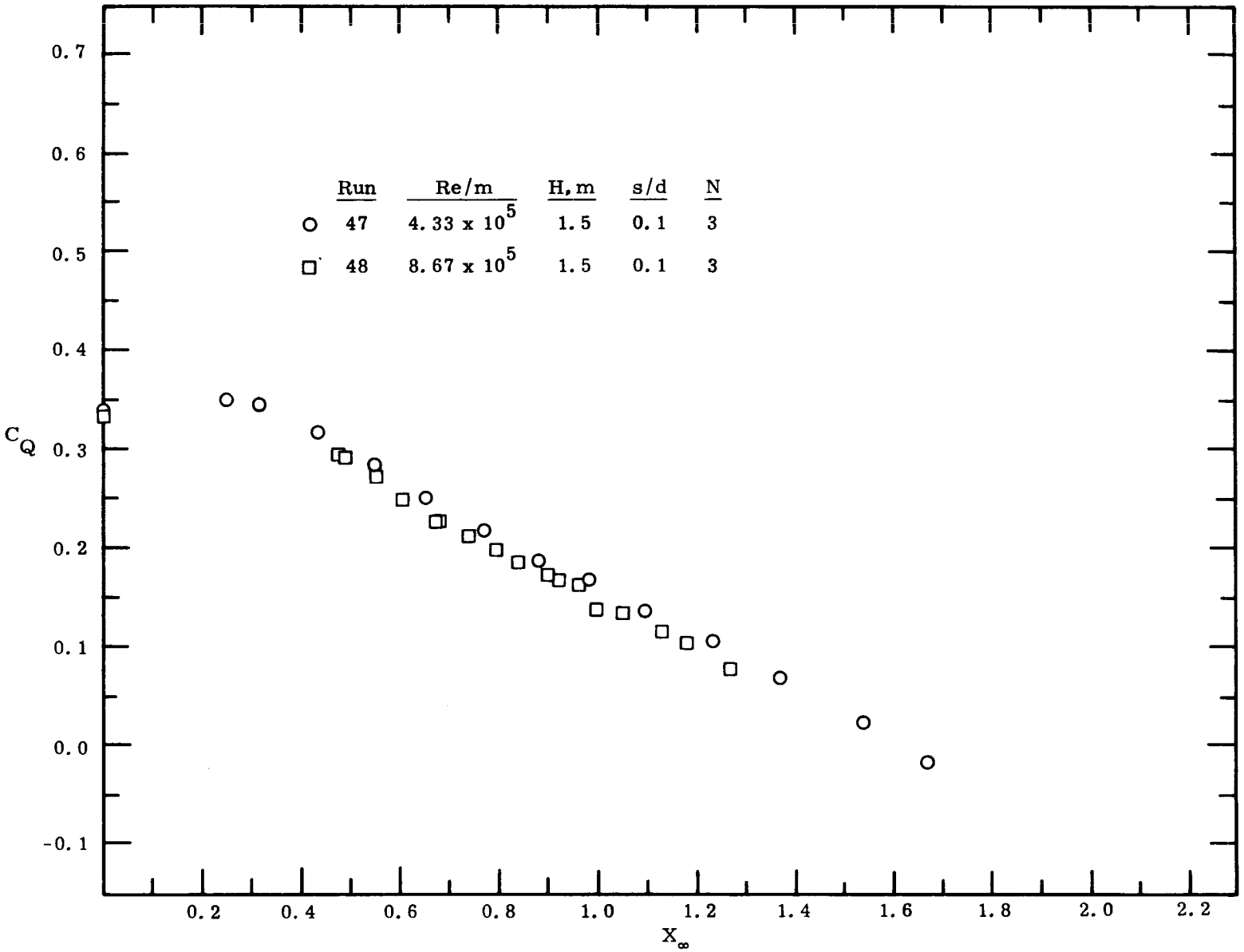

(b)

Figure 34. Power and torque coefficients as a function of speed ratio for a three-bucket Savonius rotor (Configuration 16) with a gap width ratio of 0.10 for Re/m of 4.32×10^5 and 8.64×10^5.

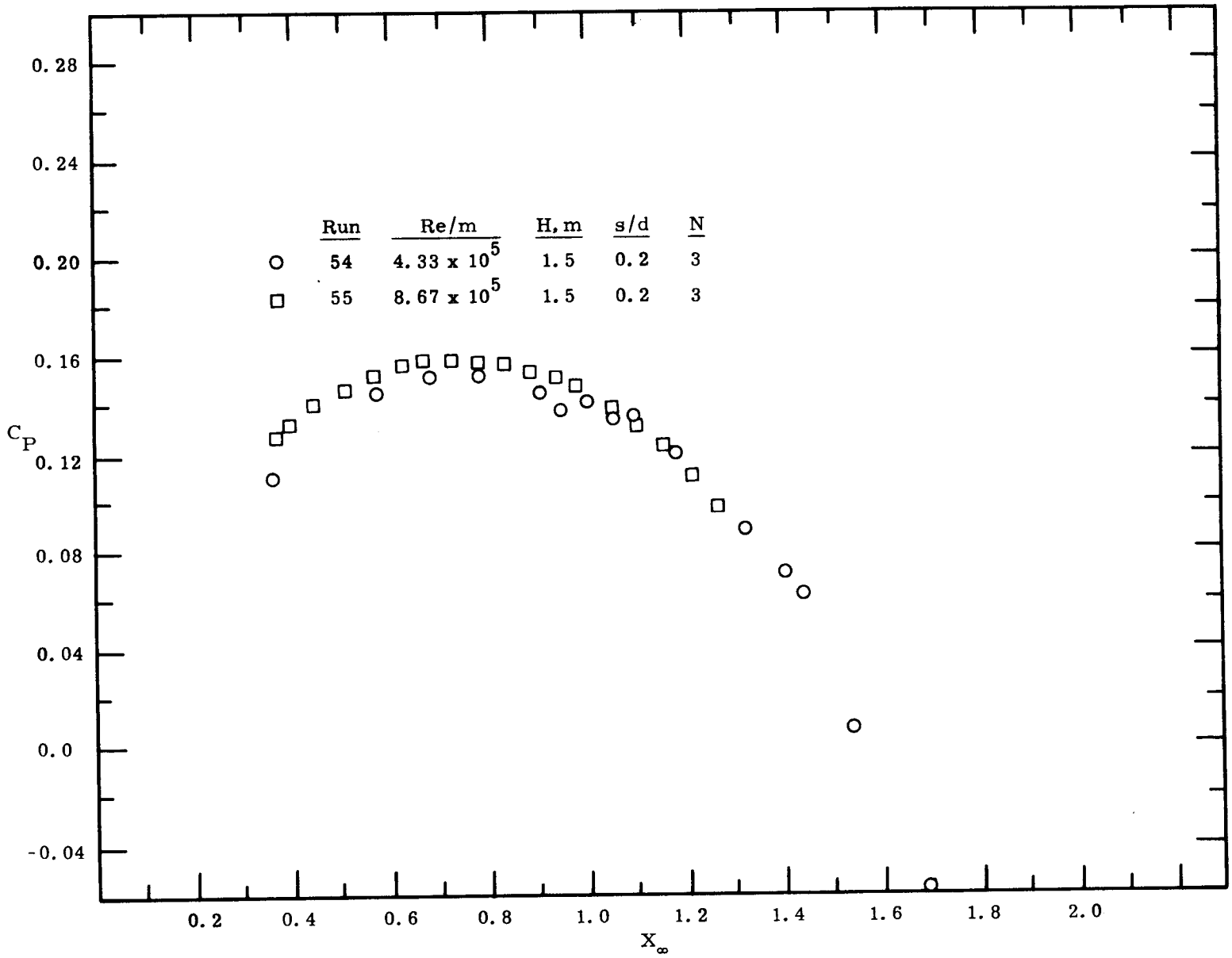
0.28
0.24
0.20
0.16
0.12
0.08
0.04
0.0
-0.04
C_P
0.2
0.4
0.6
0.8
1.0
1.2
1.4
1.6
1.8
2.0
X_∞
Run Re/m H, m s/d N
54 4.33 x 10^5 1.5 0.2 3
55 8.67 x 10^5 1.5 0.2 3

(a)

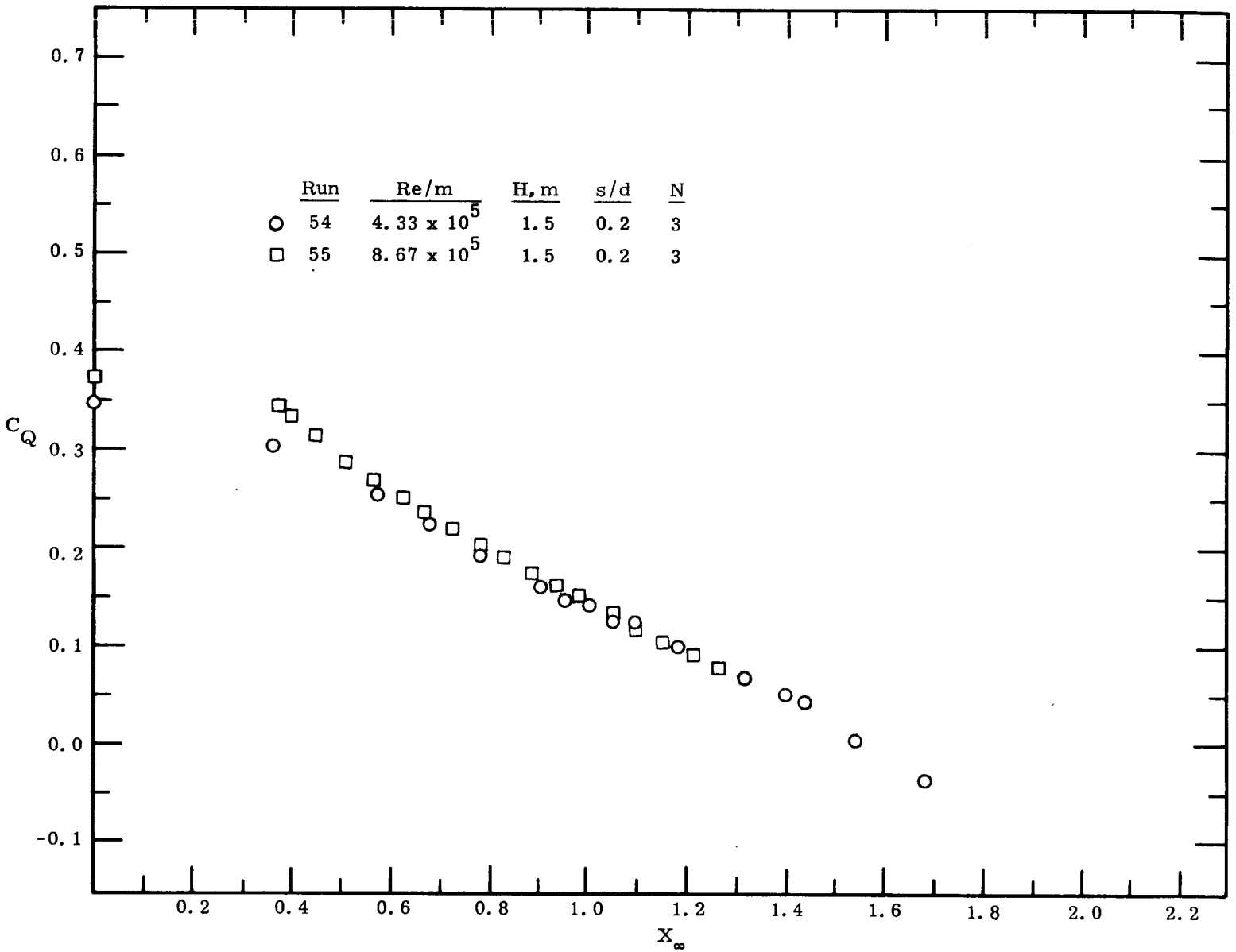

(b)

Figure 35. Power and torque coefficients as a function of speed ratio for a three-bucket Savonius rotor (Configuration 18) with a gap width ratio of 0.20 for Re/m of 4.33×10^5 and 8.67×10^5.

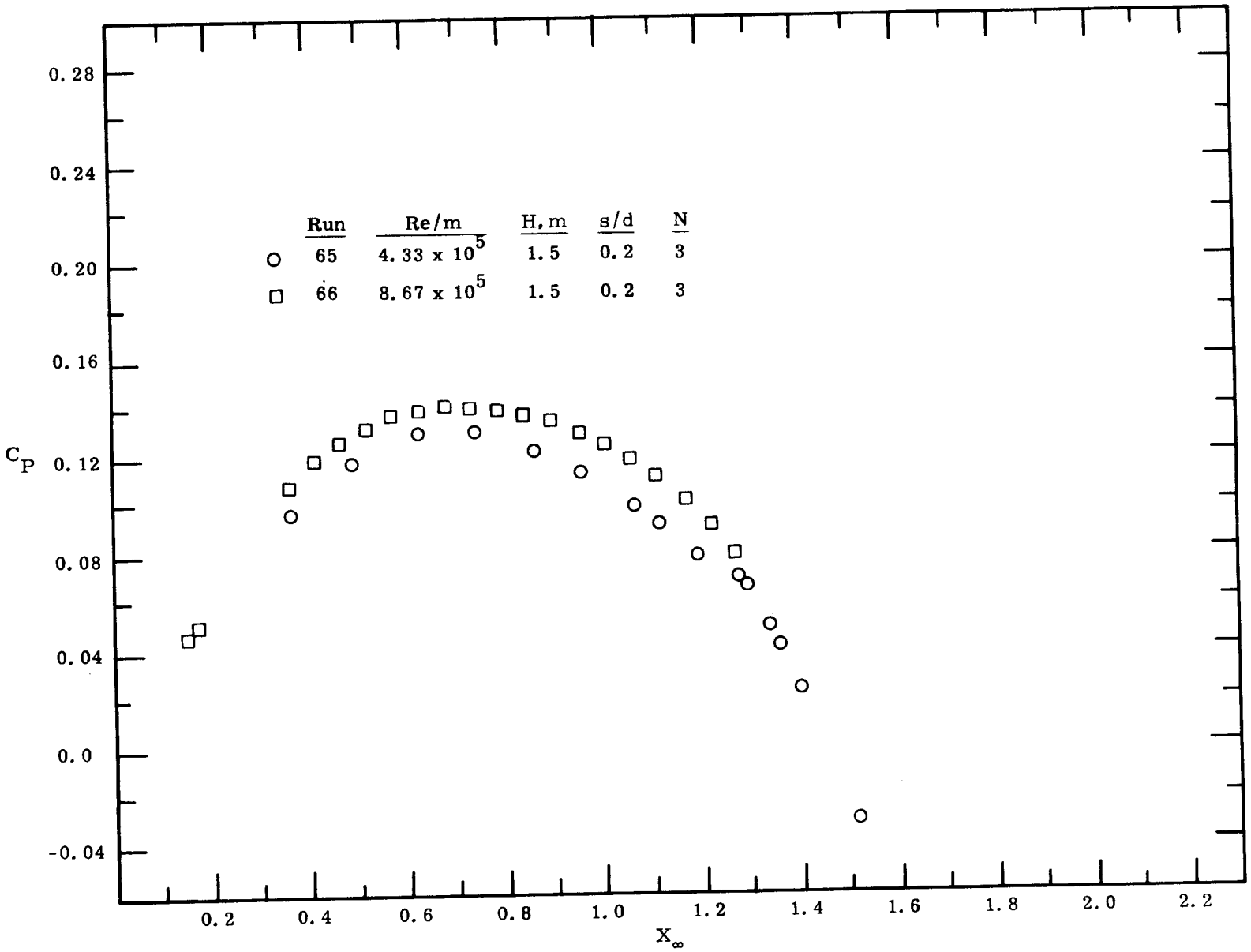
Run
Re/m
H, m
s/d
N
65
4.33 x 10^5
1.5
0.2
3
66
8.67 x 10^5
1.5
0.2
3
C_P
0.28
0.24
0.20
0.16
0.12
0.08
0.04
0.0
-0.04
0.2
0.4
0.6
0.8
1.0
1.2
1.4
1.6
1.8
2.0
2.2
X_∞

(a)

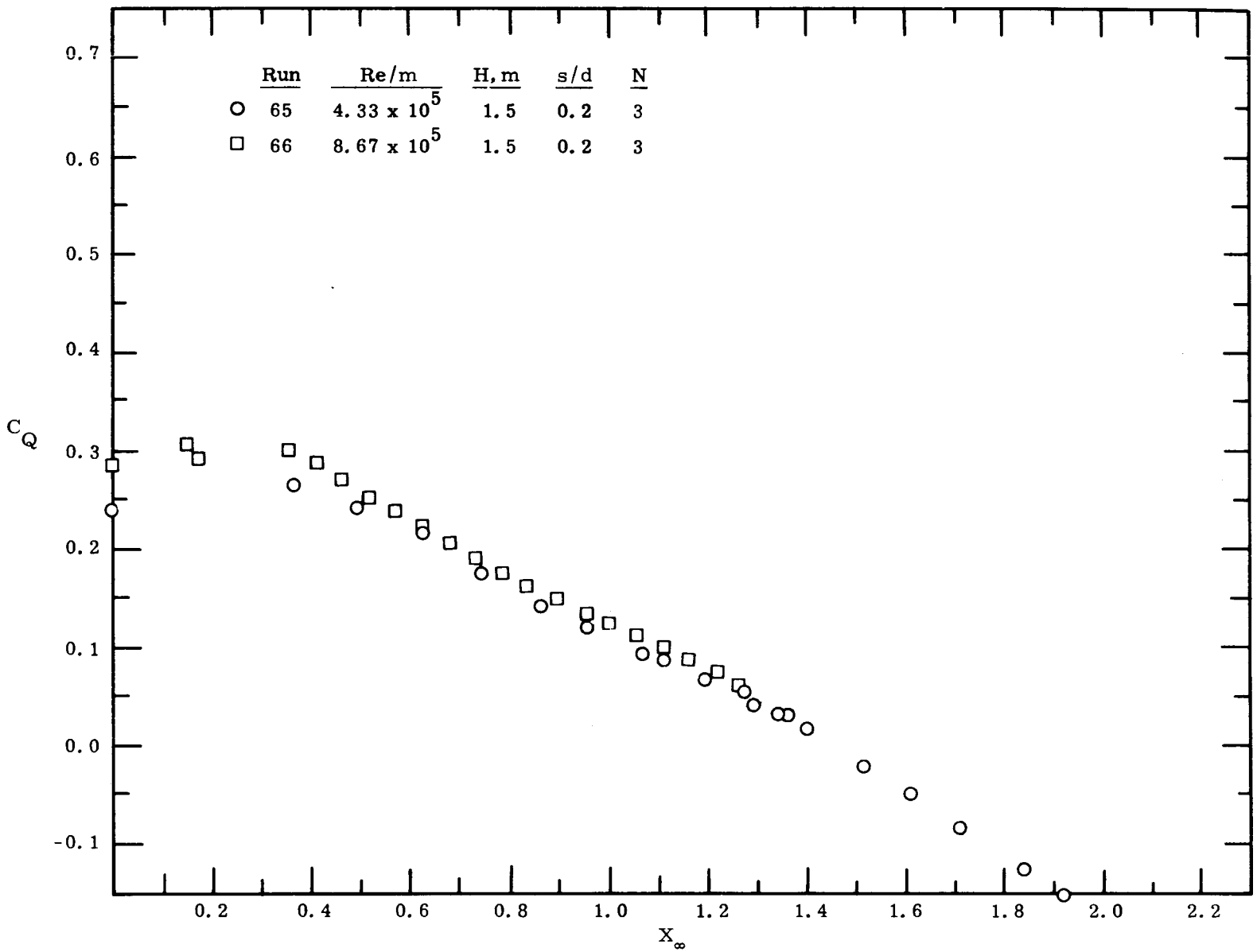

(b)

Figure 36. Power and torque coefficient as a function of speed ratio for a three-bucket Savonius rotor (Configuration 21) with a gap width ratio of 0.20 for Re/m of 4.33×10^5 and 8.67×10^5 (180° buckets).

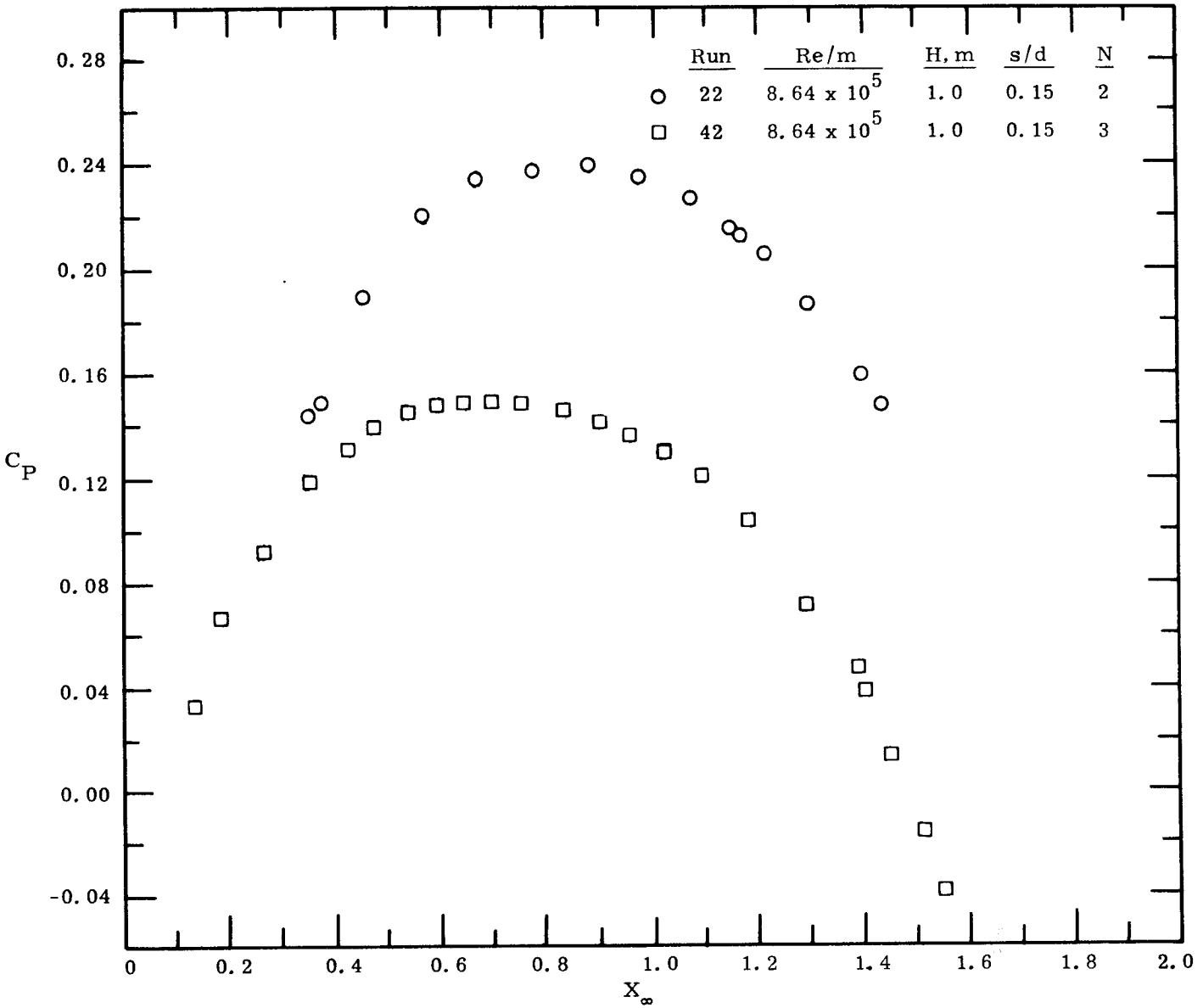
Run
Re/m
H, m
s/d
N
22
8.64 x 10^5
1.0
0.15
2
42
8.64 x 10^5
1.0
0.15
3
0.28
0.24
0.20
0.16
0.12
0.08
0.04
0.00
-0.04
C_P
0
0.2
0.4
0.6
0.8
1.0
1.2
1.4
1.6
1.8
2.0
X_∞

(a)

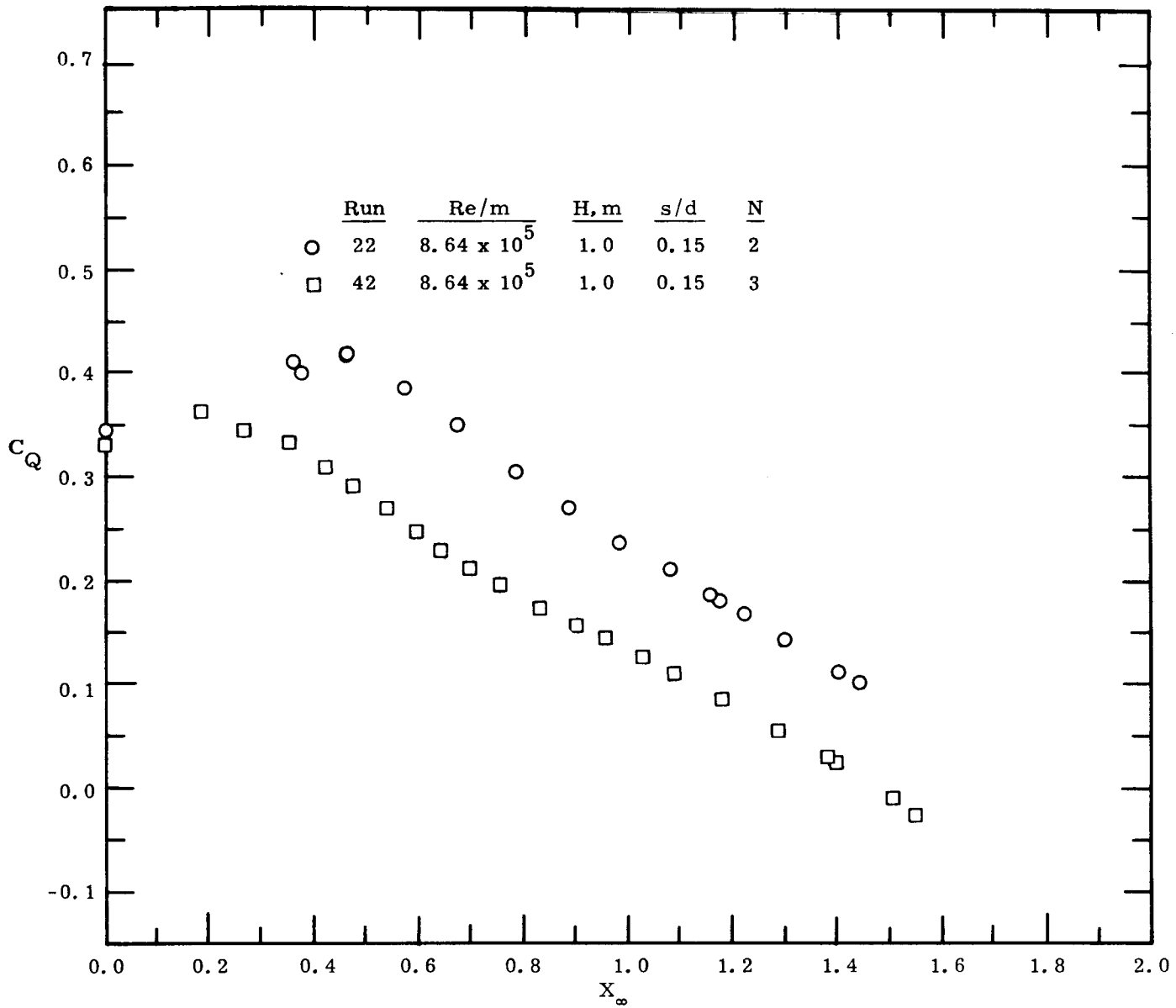

(b)

Figure 37. A comparison of the power and torque coefficients for two- and three-bucket Savonius rotors with a gap width ratio of 0.15 at Re/m of 8.64×10^5.

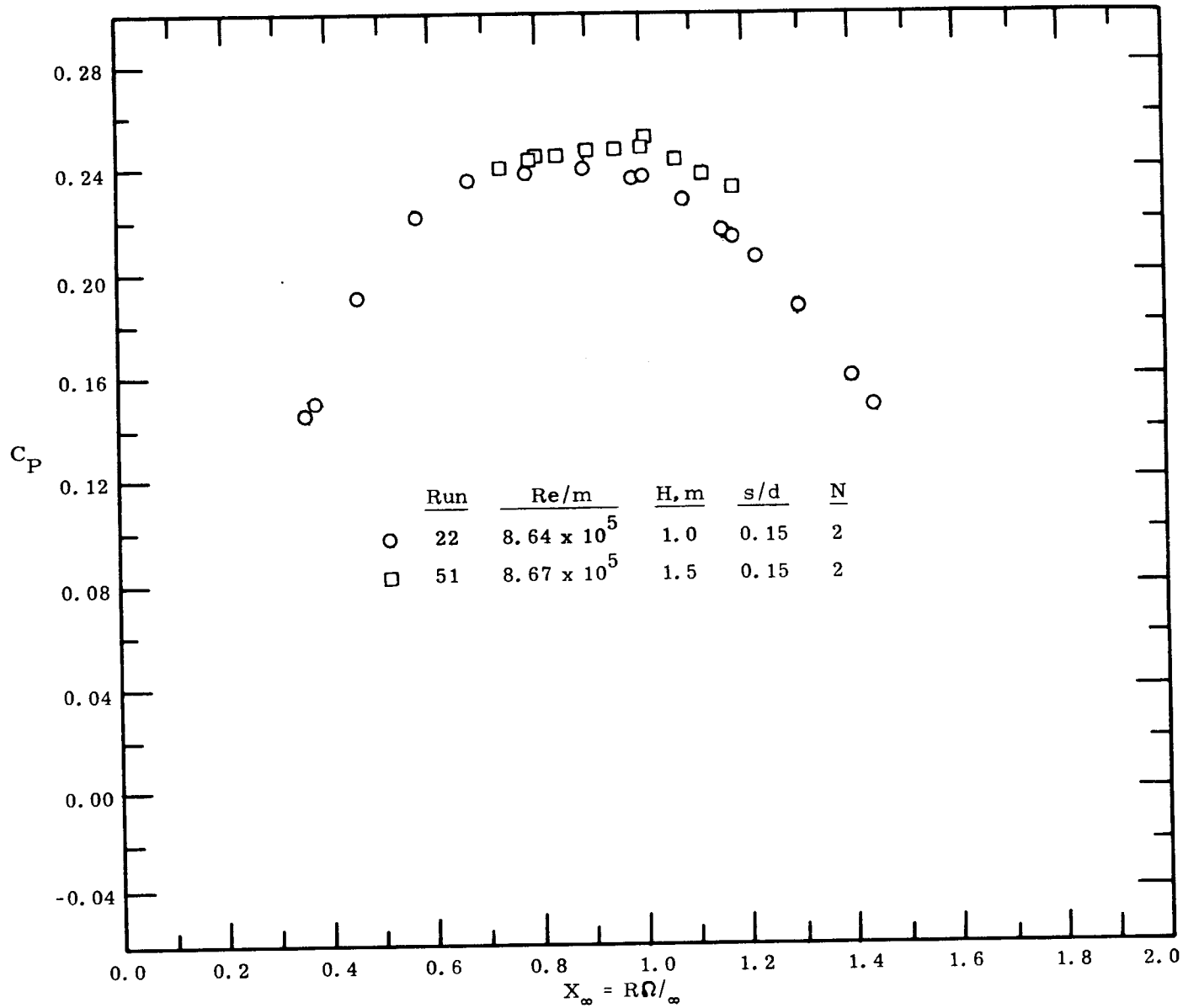
0.28
0.24
0.20
0.16
0.12
0.08
0.04
0.00
-0.04
C_P
0.0
0.2
0.4
0.6
0.8
1.0
1.2
1.4
1.6
1.8
2.0
$X_\infty = R\Omega/_\infty$
Run Re/m H, m s/d N
22 8.64 x 10^5 1.0 0.15 2
51 8.67 x 10^5 1.5 0.15 2

(a)

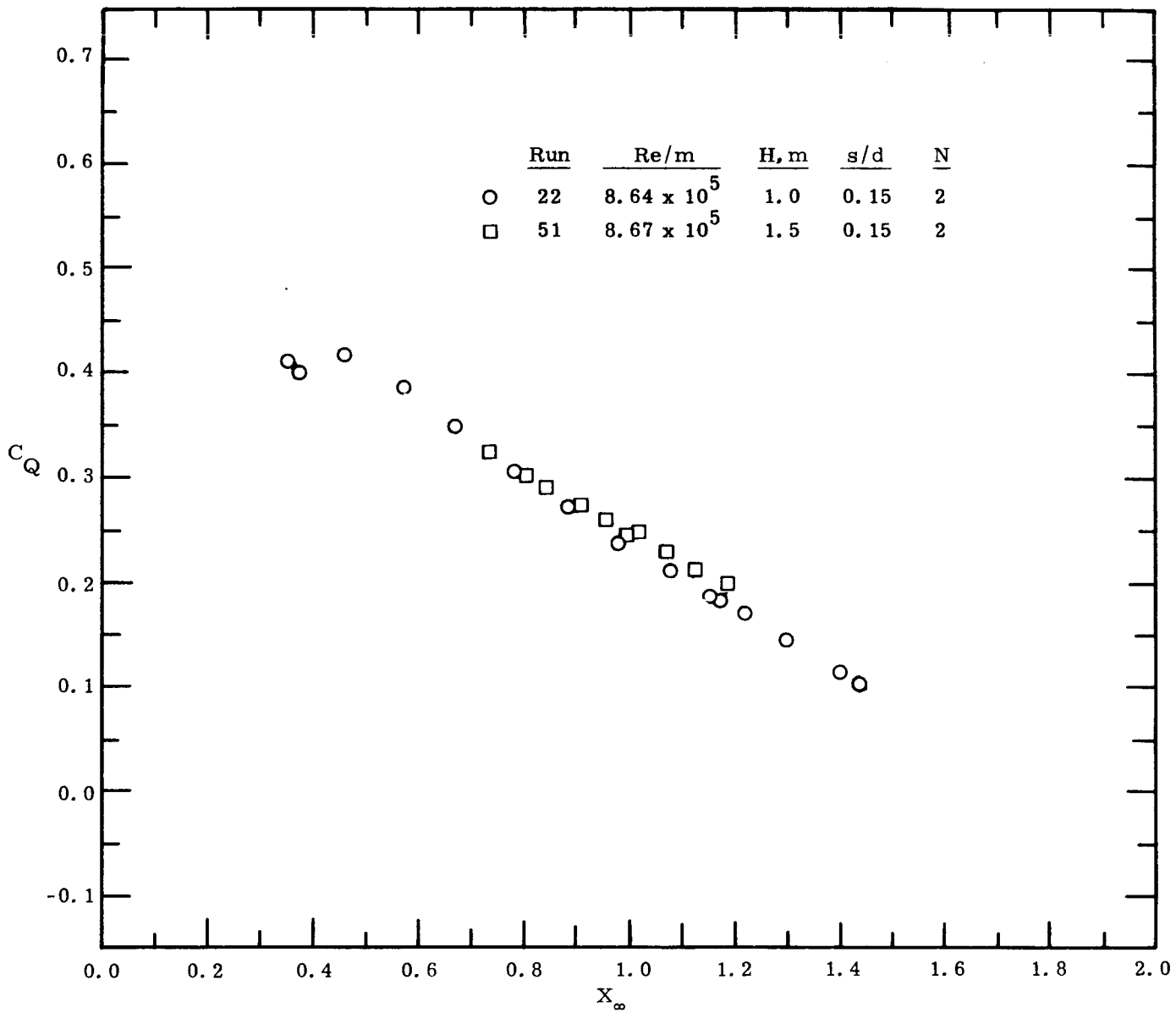

(b)

Figure 38. Comparison of power and torque coefficients for a two-bucket configuration with gap width ratio of 0.15 at Re/m of 8.6×10^5 for two rotor heights.

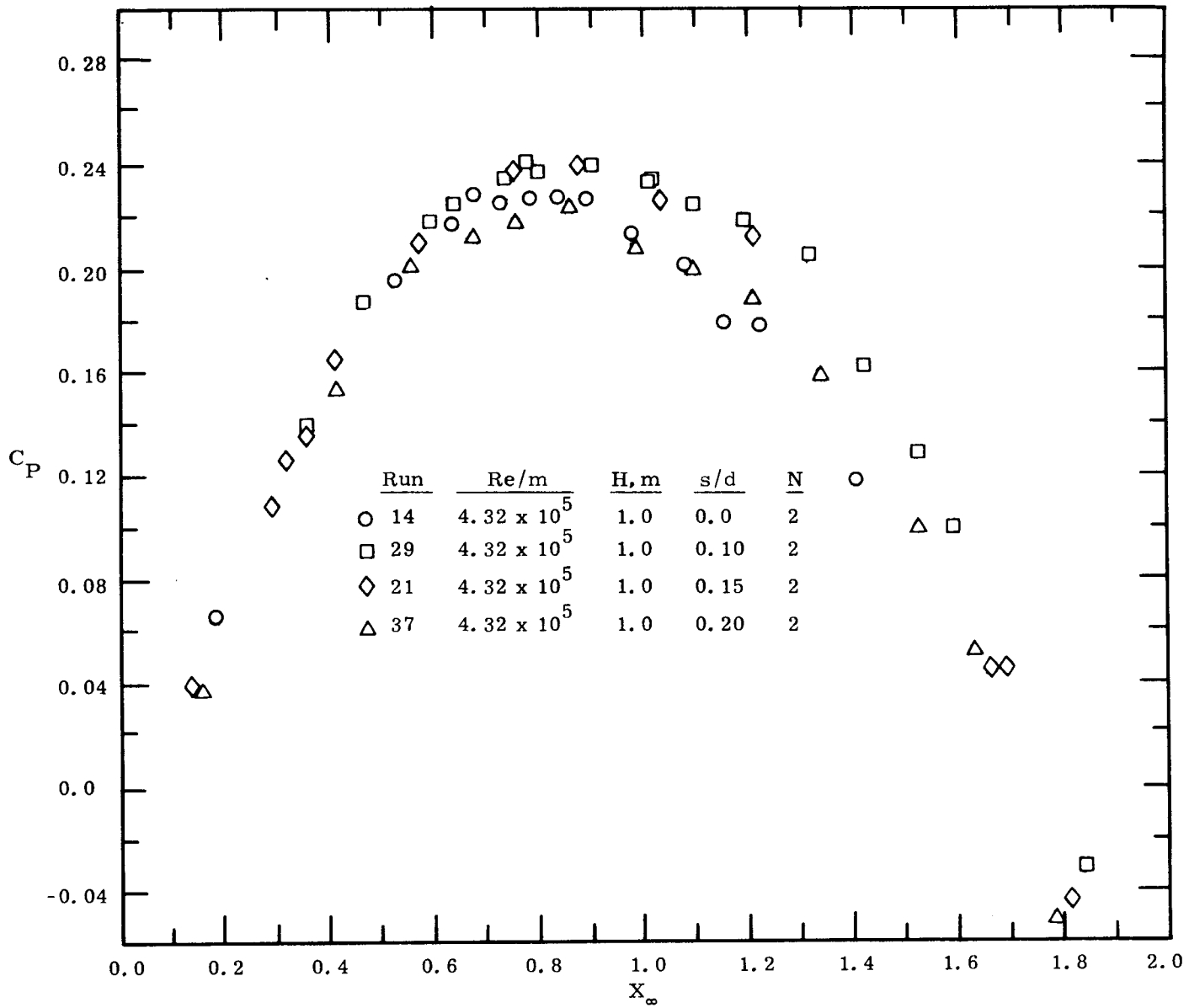
0.28
0.24
0.20
0.16
0.12
0.08
0.04
0.0
-0.04
C_P
0.0
0.2
0.4
0.6
0.8
1.0
1.2
1.4
1.6
1.8
2.0
X_∞
Run | Re/m | H, m | s/d | N
14 | 4.32 x 10^5 | 1.0 | 0.0 | 2
29 | 4.32 x 10^5 | 1.0 | 0.10 | 2
21 | 4.32 x 10^5 | 1.0 | 0.15 | 2
37 | 4.32 x 10^5 | 1.0 | 0.20 | 2

(a)

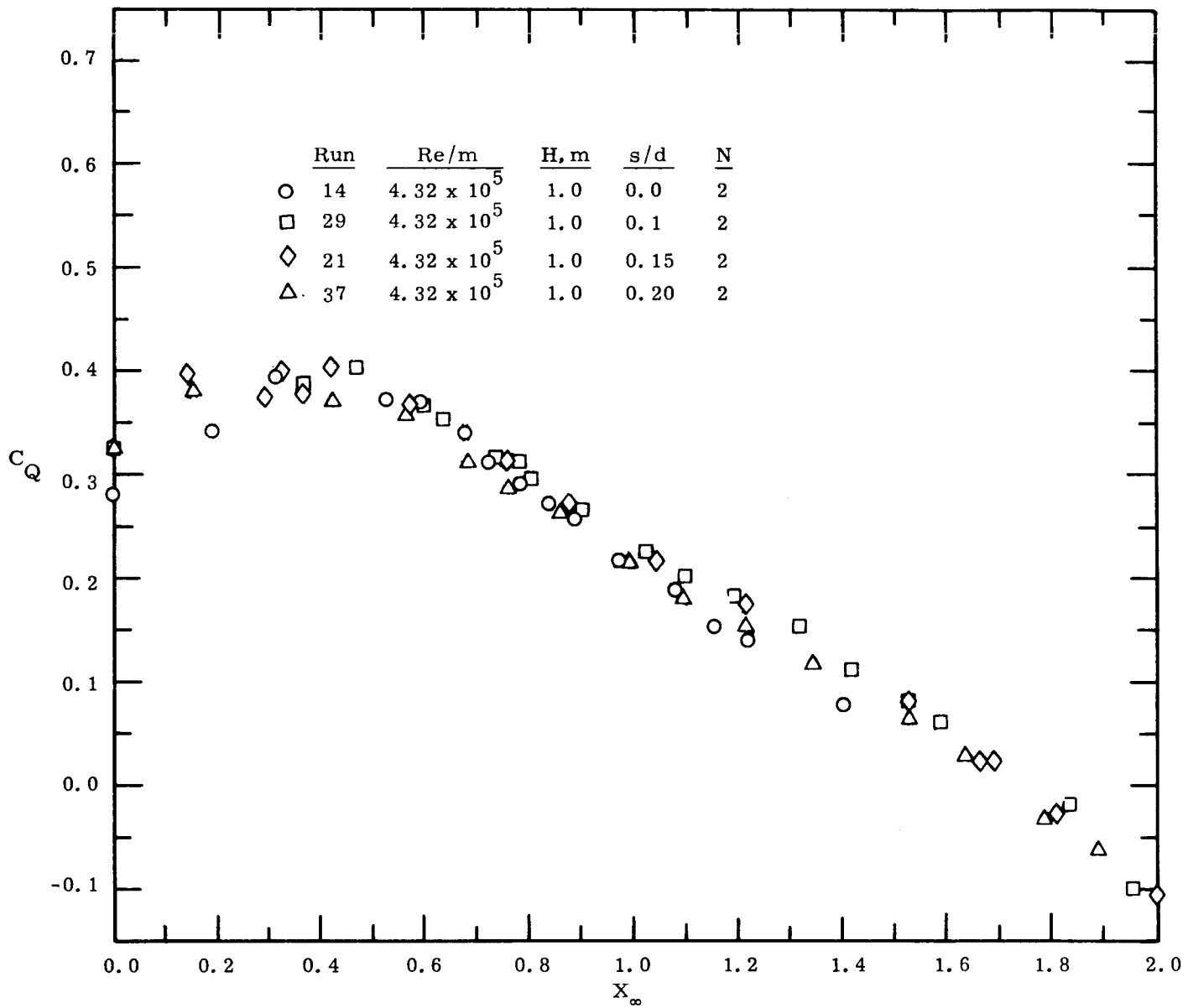

(b)

Figure 39. Power and torque coefficients for the 1-metre, two-bucket Savonius rotors with various gap width ratios at a Re/m of 4.32×10^5.

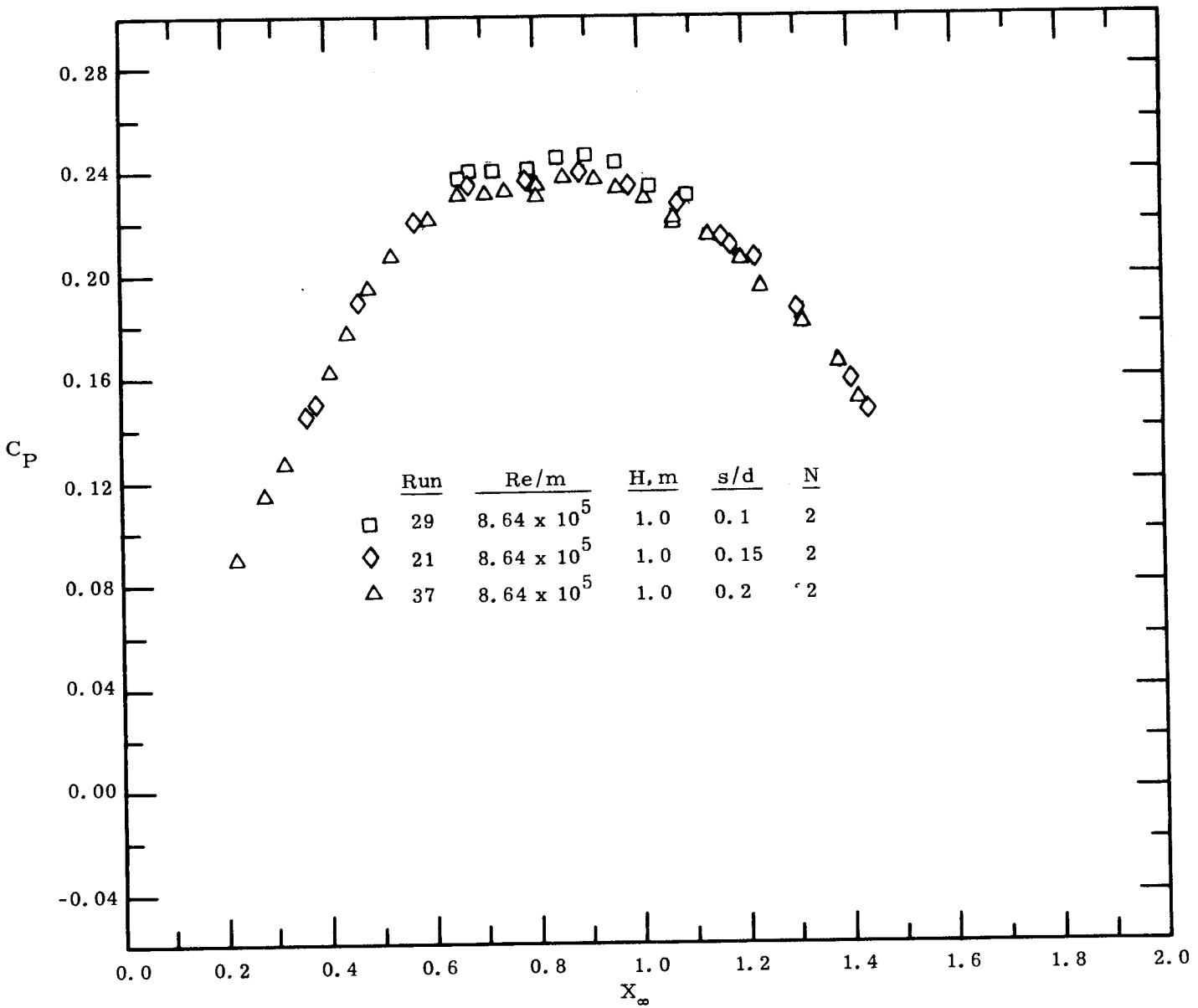
0.28
0.24
0.20
0.16
0.12
0.08
0.04
0.00
-0.04
C_P
0.0
0.2
0.4
0.6
0.8
1.0
1.2
1.4
1.6
1.8
2.0
X_∞
Run Re/m H, m s/d N
29 8.64 x 10^5 1.0 0.1 2
21 8.64 x 10^5 1.0 0.15 2
37 8.64 x 10^5 1.0 0.2 2

(a)

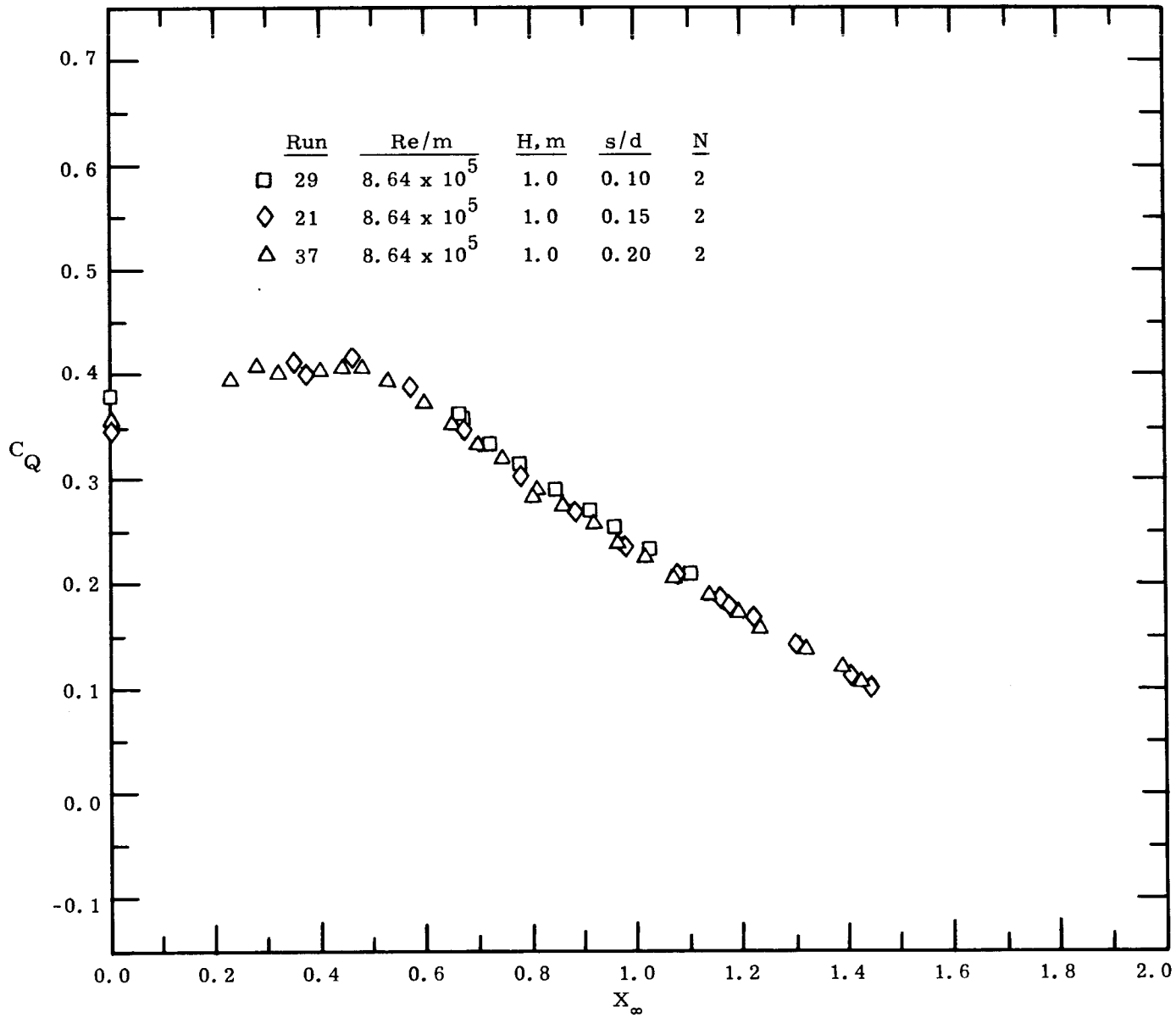

(b)

Figure 40. Power and torque coefficients for the 1-metre, two-bucket Savonius rotors with various gap width ratios at a Re/m of 8.64×10^5.

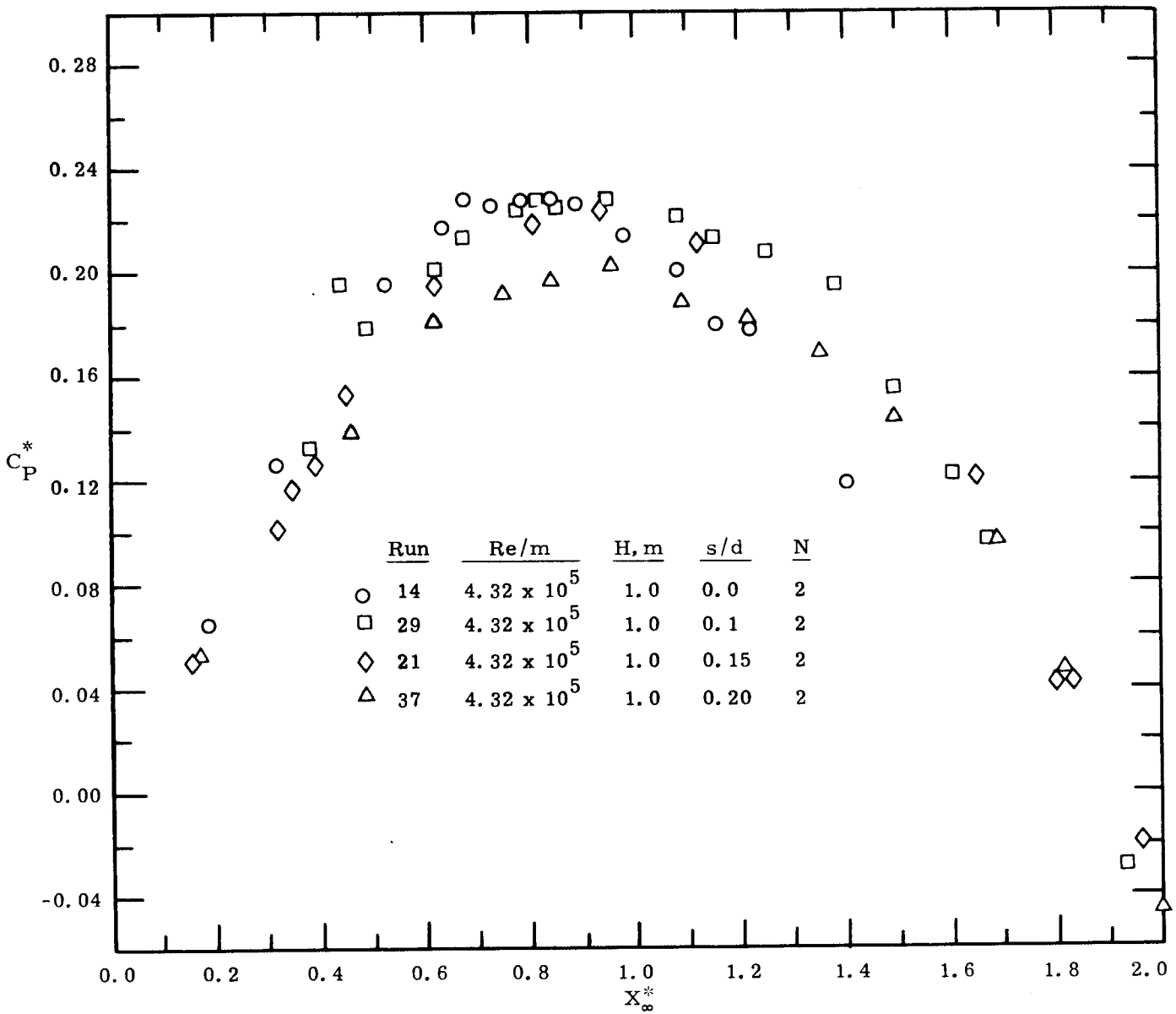
0.28
0.24
0.20
0.16
0.12
0.08
0.04
0.00
-0.04
C_P^*
0.0
0.2
0.4
0.6
0.8
1.0
1.2
1.4
1.6
1.8
2.0
X_∞^*
Run Re/m H, m s/d N
14 4.32 x 10^5 1.0 0.0 2
29 4.32 x 10^5 1.0 0.1 2
21 4.32 x 10^5 1.0 0.15 2
37 4.32 x 10^5 1.0 0.20 2

(a)

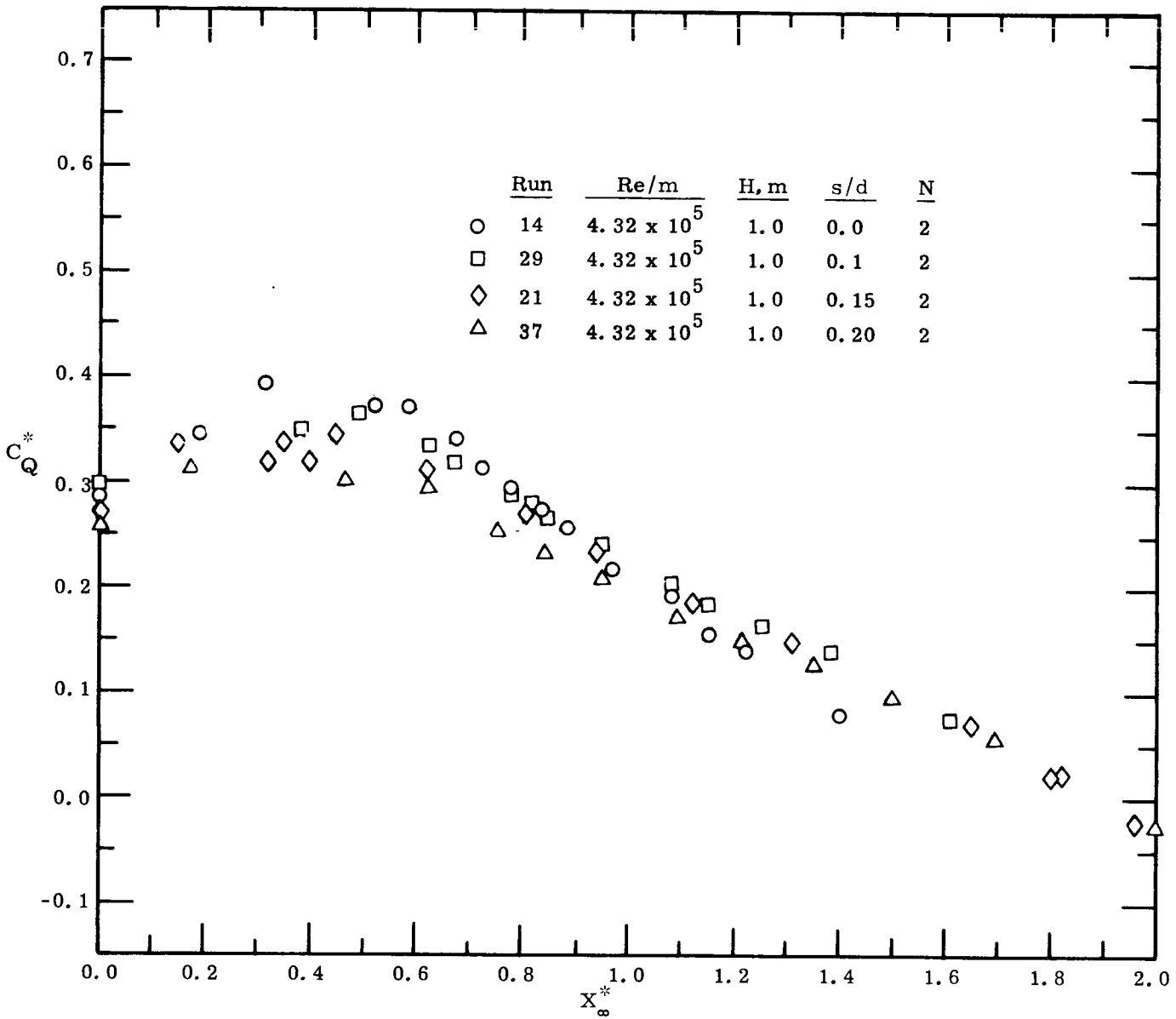

(b)

Figure 41. Normalized turbine power for 1-metre, two-bucket Savonius rotors as a function of normalized rotational speed showing the effect of gap width ratio for a given bucket size for Re/m of 4.32×10^5.

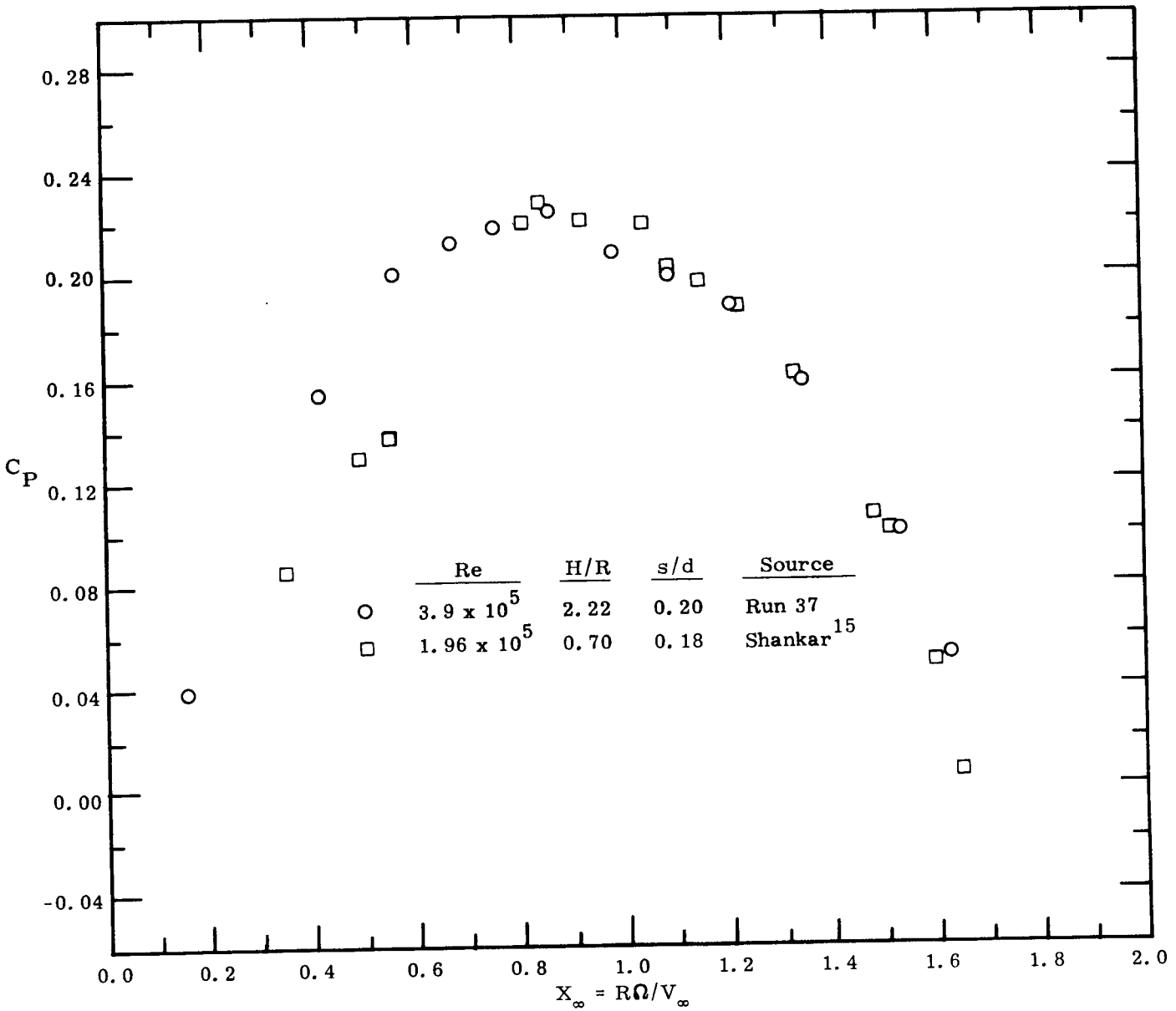

Figure 42. Power coefficients for a two-bucket Savonius rotor at a Reynolds number of 3.9 x 10^5 compared to Shankar's data for a two-bucket Savonius rotor for a Reynolds number of 1.96 x 10^5 (Reynolds numbers are based on rotor diameter).

APPENDIX

UNCERTAINTY ANALYSIS

Appendix

UNCERTAINTY ANALYSIS

The method of Kline and McClintock[A-1] was used to estimate the experimental uncertainty associated with the determination of torque coefficient, C_Q, power coefficient, C_p, and speed ratio, X_∞. These quantities are calculated from the following relationships:

$$C_Q = \frac{(Q_i + Q_f)}{q_\infty R A_s} \tag{A.1}$$

$$C_p = \frac{(Q_i + Q_f)\,\Omega}{q_\infty V_\infty A_s} \tag{A.2}$$

$$X_\infty = \frac{R\Omega}{V_\infty} \tag{A.3}$$

Both the turbine torque and the rotational speed were measured directly, whereas the freestream velocity and dynamic pressure were determined from the measured (uncorrected) dynamic pressure and an assumed tunnel blockage factor. These relationships are

$$q_\infty = q_{\infty_u}(1 + \epsilon_t)^2 \tag{A.4}$$

$$V_\infty = \sqrt{\frac{2q_\infty}{\rho}}\ . \tag{A.5}$$

In a previous study of the experimental uncertainty associated with the testing of Darrieus turbine models in the same test facility as this study, Blackwell, Sheldahl, and Feltz[A-2] concluded that the most important variables affecting the computed uncertainty were Ω, Q_i, Q_f, q_{∞_u}, and ϵ_t. This conclusion allows the uncertainty to be written as

$$\frac{\delta C_Q}{C_Q} = \left\{ \left[\frac{\delta(Q_i + Q_f)}{Q_i + Q_f} \right]^2 + \left(\frac{\delta q_{\infty_u}}{q_{\infty_u}} \right)^2 + \left(2 \frac{\delta \epsilon_t}{1 + \epsilon_t} \right)^2 \right\}^{1/2} \tag{A.6}$$

$$\frac{\delta C_p}{C_p} = \left\{ \left[\frac{\delta(Q_i + Q_f)}{Q_i + Q_f} \right]^2 + \left(\frac{3}{2} \frac{\delta q_{\infty_u}}{q_{\infty_u}} \right)^2 + \left(3 \frac{\delta \epsilon_t}{1 + \epsilon_t} \right)^2 + \left(\frac{\delta \Omega}{\Omega} \right)^2 \right\}^{1/2} \tag{A.7}$$

$$\frac{\delta X_\infty}{X_\infty} = \left[\left(\frac{1}{2} \frac{\delta q_{\infty_u}}{q_{\delta_u}} \right)^2 + \left(\frac{\delta \epsilon_t}{1 + \epsilon_t} \right)^2 + \left(\frac{\delta \Omega}{\Omega} \right)^2 \right]^{1/2} . \tag{A.8}$$

Table A-I tabulates the assumed uncertainties for this analysis. Most are self-explanatory, but the torque and dynamic pressure require a few words of explanation. The calibration curve for the torque meter was linear to within 0.4 in-lbf; the indicator was accurate to within 0.3 in-lbf and can be read to within 0.1 in-lbf for a total of 0.8 in-lbf uncertainty. Reference 8 indicates that the tunnel dynamic pressure was uniform to within ±1.5 percent and that a prescribed value of the dynamic pressure can be set to within 0.017 psf. The blockage uncertainty was assumed constant for all runs.

From the data presented in Table A-I and the basic uncertainty equations, one can show that the relative uncertainty in C_Q, in C_P, and in X_∞ decreases with increasing rpm, torque, and dynamic pressure. Increasing the model size will increase the tunnel blockage uncertainty term while decreasing the torque uncertainty term.

TABLE A-I

Uncertainty in Primary Variables
(from Ref. A-2)

Variable		Uncertainty	
Ω	rotation speed	$\delta\Omega$	= 1 rpm
Q	torque	δQ	= 0.8 in-lbf
Q_f	friction torque	δQ_f	= 0.8 in-lbf
q_{∞_u}	dynamic pressure	δq_{∞_u}	= 0.015 q_{∞_u} + 0.017 (lbf/ft^2)
ϵ_t	total blockage	$\delta\epsilon_t$	= 0.5 ϵ_t

For the data presented in this report, the following bounds on the uncertainty of the primary variables can be established:

$$0.002 < \frac{\delta\Omega}{\Omega} < 0.040$$

$$-23.5 < Q_i + Q_f < 197.3 \text{ (in-lbf)}$$

$$0.008 < \frac{\delta(Q_i + Q_f)}{Q_i + Q_i} < \infty^*$$

$$0.006 < \frac{\delta\epsilon_t}{1 + \epsilon_t} < 0.008$$

$$0.023 < \frac{\delta q_{\infty_u}}{q_{\infty_u}} < 0.048 \quad .$$

*This upper bound is infinity because $Q_i + Q_f$ can theoretically be zero.

The uncertainty in torque and dynamic pressure are the major contributors to the overall uncertainty, whereas rotational speed and tunnel blockage are only minor contributors.

Figures A-1 and A-2 present representative uncertainty calculations for typical two- and three-bucket configurations. The bars around each data point represent uncertainty bounds. For those data points that do not have uncertainty bars, the uncertainty lies within the plotting symbol.

Figure A-1 presents the uncertainty for a two-bucket configuration. The uncertainty in C_p is quite large for the 4.32×10^5 Re run because the dynamic pressure is low; the higher Re run has a much smaller uncertainty. The uncertainty in C_Q and in X_∞ is smaller than that for C_p.

Figure A-2 presents the uncertainty for a three-bucket configuration. The general trends are the same as for the two-bucket configuration.

The uncertainty trends presented can be taken to be representative of the uncertainty for other configurations tested.

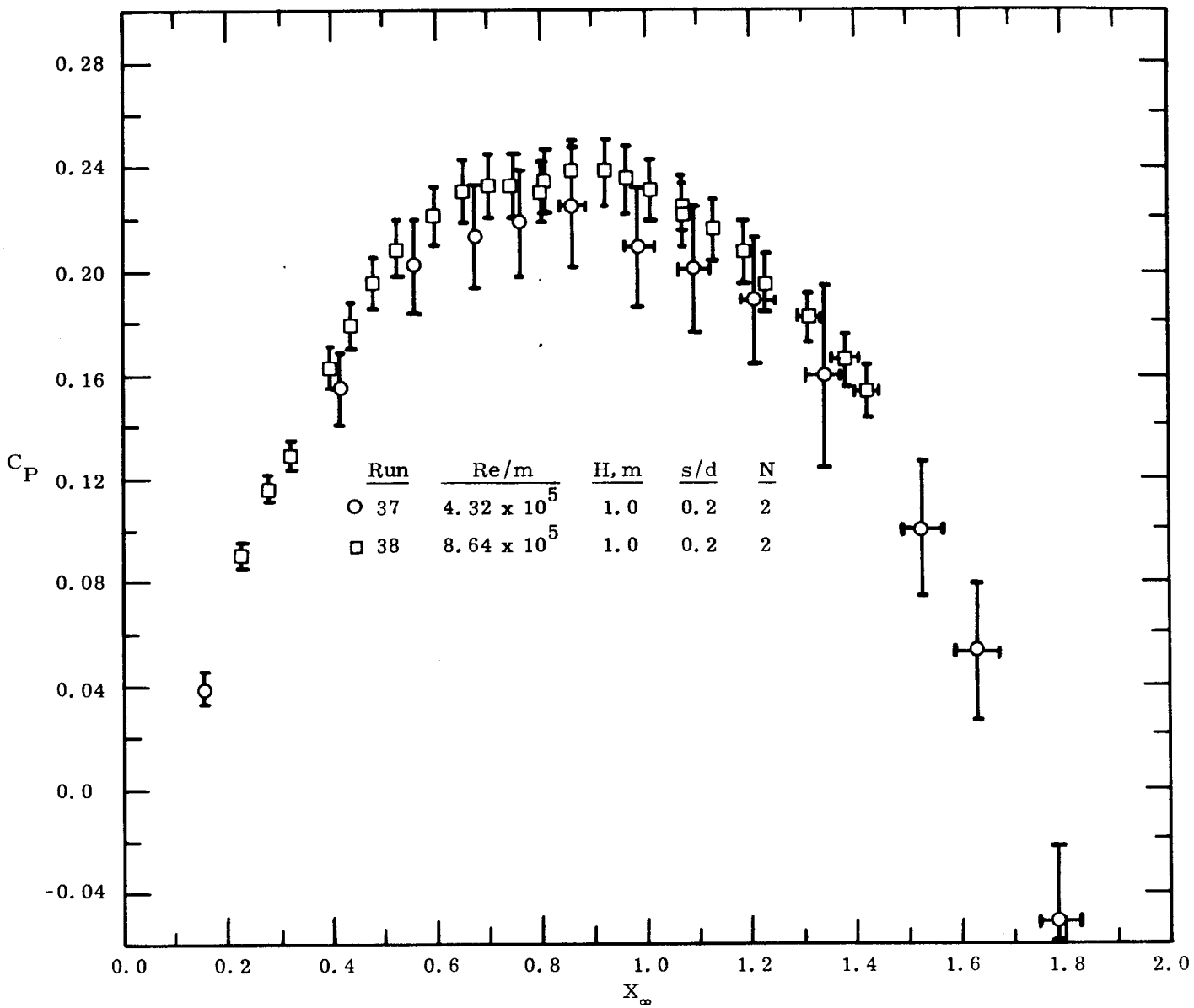
0.28
0.24
0.20
0.16
0.12
0.08
0.04
0.0
-0.04
C_P
Run Re/m H, m s/d N
O 37 4.32 x 10^5 1.0 0.2 2
□ 38 8.64 x 10^5 1.0 0.2 2
0.0 0.2 0.4 0.6 0.8 1.0 1.2 1.4 1.6 1.8 2.0
X_∞

(a)

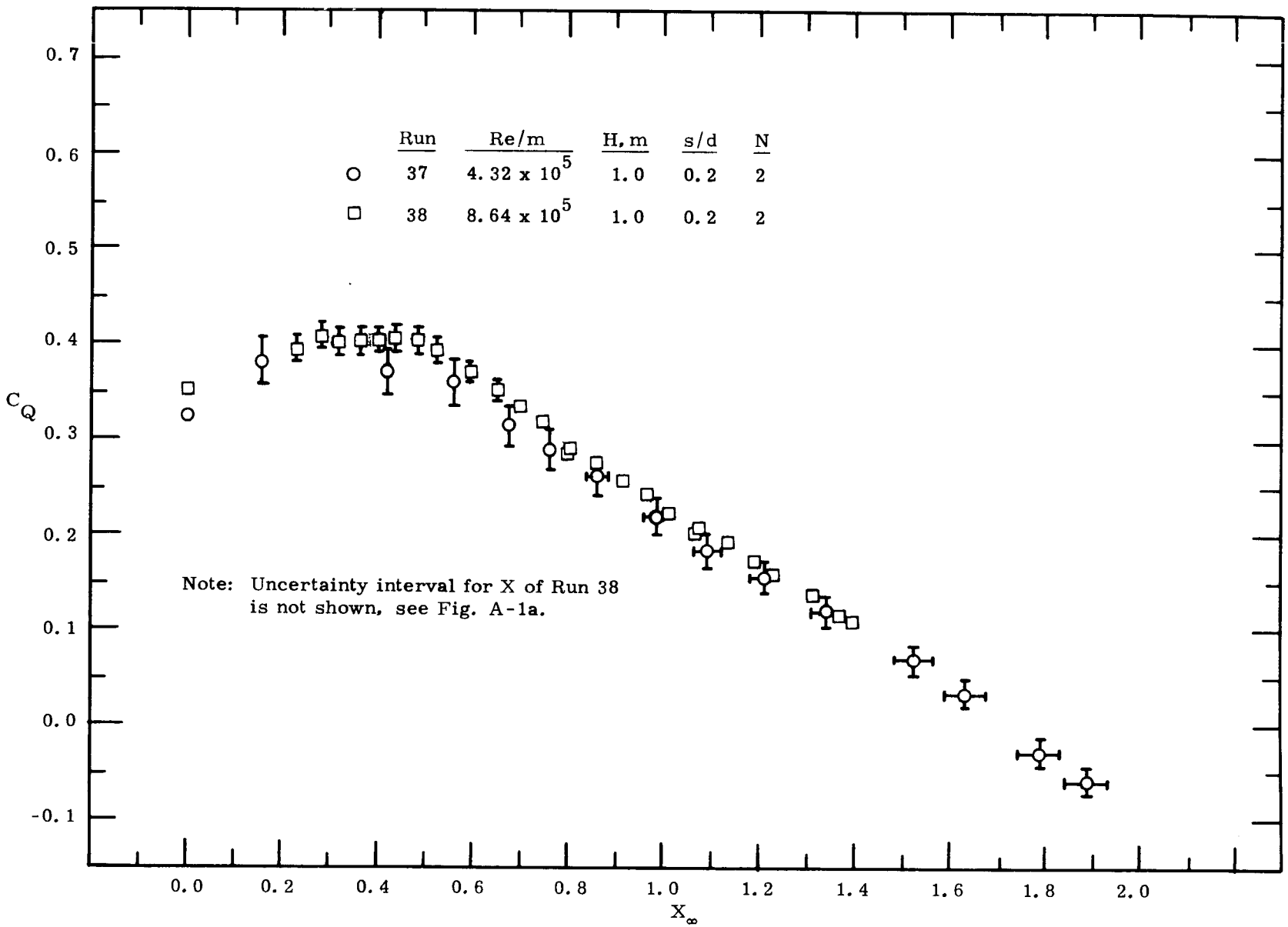

(b)

Figure A-1. Uncertainty analysis for a two-bucket Savonius rotor for two Reynolds numbers.

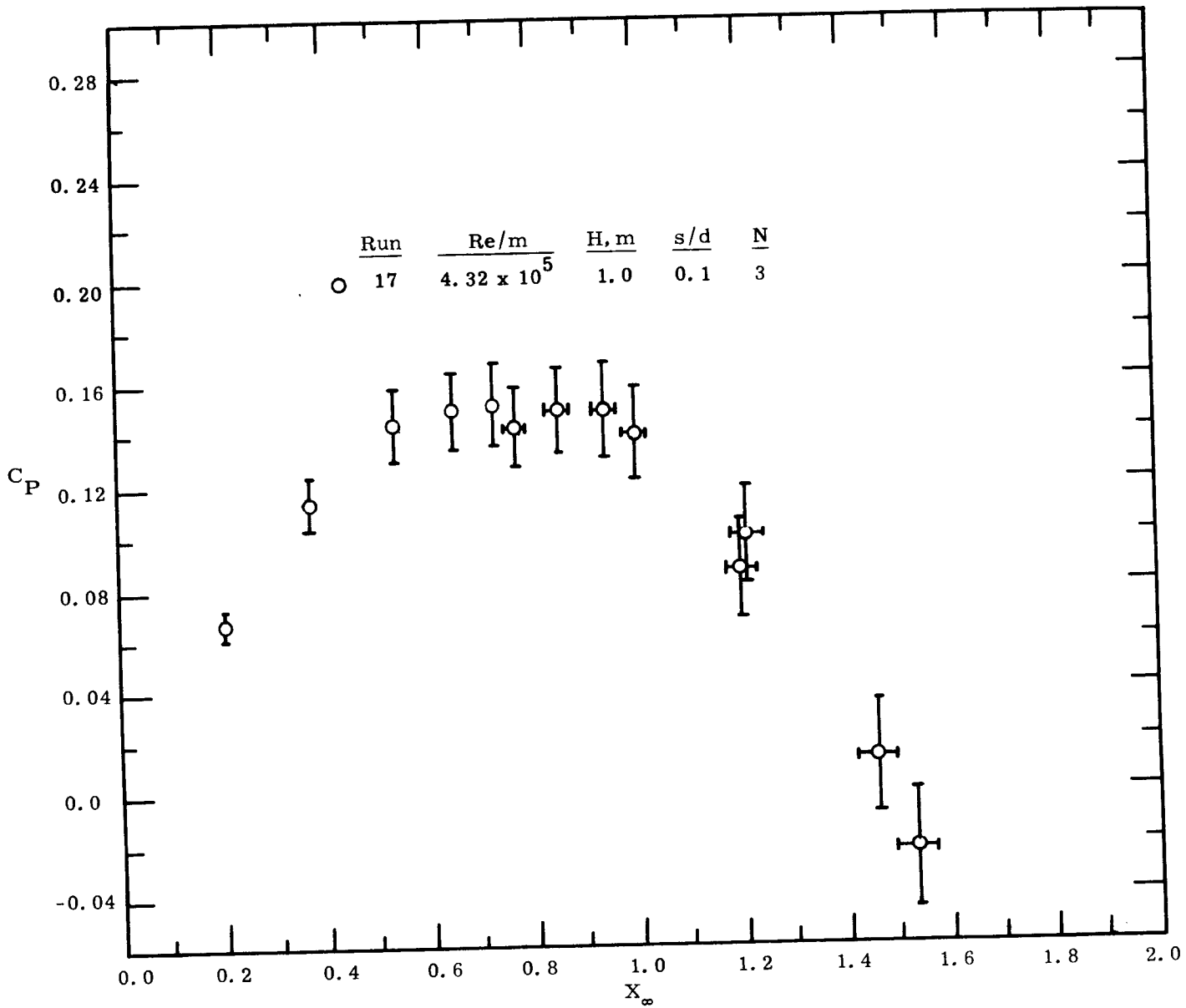
Run
Re/m
H, m
s/d
N
17
4.32 x 10^5
1.0
0.1
3
0.28
0.24
0.20
0.16
0.12
0.08
0.04
0.0
-0.04
C_P
0.0
0.2
0.4
0.6
0.8
1.0
1.2
1.4
1.6
1.8
2.0
X_∞

(a)

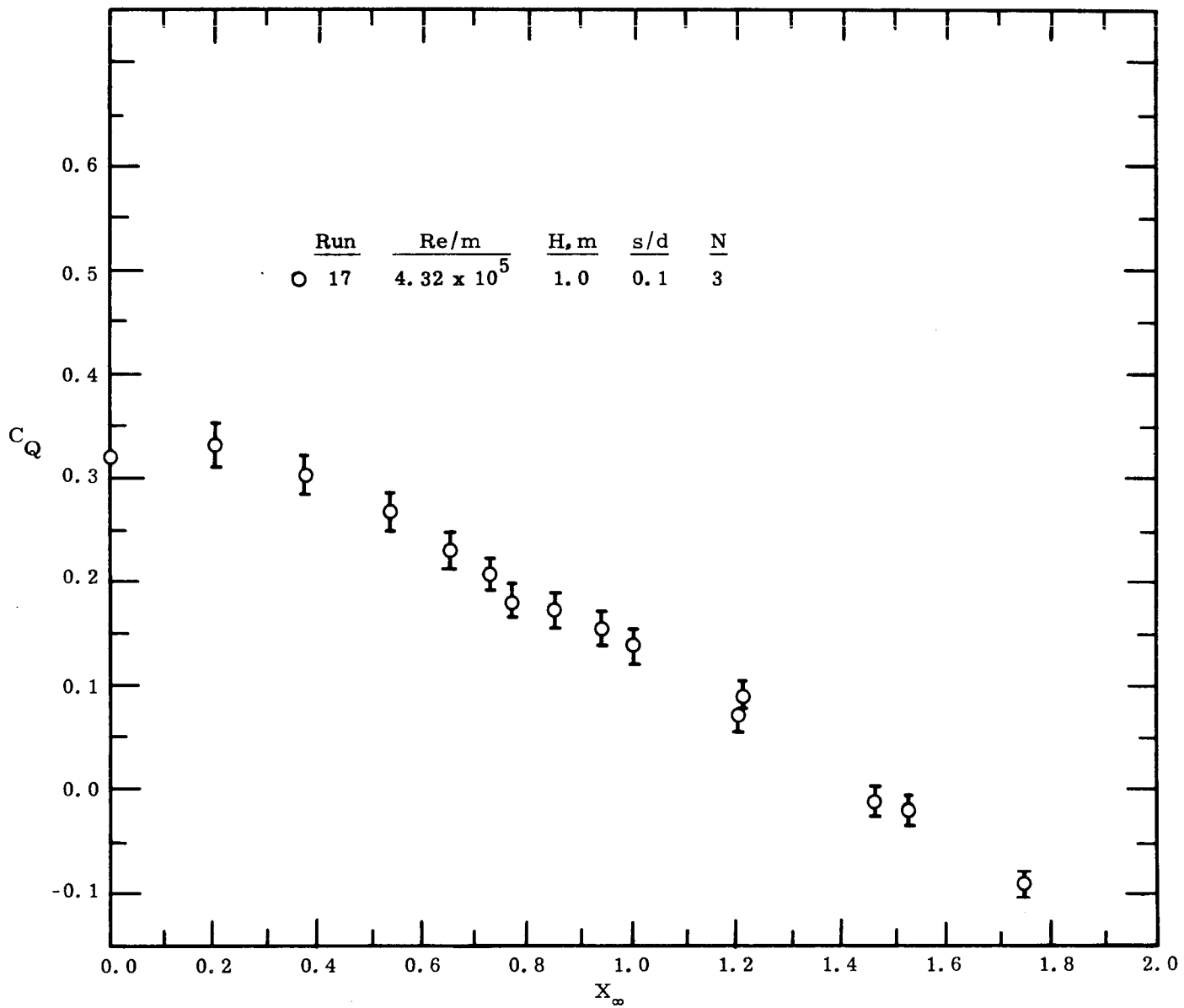

(b)

Figure A-2. Uncertainty analysis for a three-bucket Savonius rotor.

REFERENCES

1. Alexander Klemin, "The Savonius Wing Rotor," Mechanical Engineering, Vol. 47, No. 11 (November 1925).

2. S. J. Savonius, The Wing Rotor in Theory and Practice, Savonius Co., Finland (1928).

3. S. J. Savonius, "The S-Rotor and Its Applications," Mechanical Engineering, Vol. 53, No. 5 (May 1931).

4. G. vonBach, Untersuchungen uber Savonius-Rotoren und verwandte Stronungs-maschienen, Forsch. auf dem Gebiete des Ingenieurwesens, 2, pp. 218-231 (1931). (Translated to English by G. T. Ward; available from Brace Research Institute, Ste. Anne-de-Bellevue 800, Quebec, Canada HOAICO.)

5. New York University, Final Report on the Wind Turbine, Office of Production Research and Development, War Production Board, Washington, DC (January 1946).

6. R. D. Gaul, J. M. Snodgrass, and D. J. Cretzler, "Some Dynamical Properties of the Savonius Rotor Current Meter," Marine Sciences Instrumentation, Vol. 2, 1962, pp. 115-125.

7. M. H. Simonds and A. Bodek, Performance Test of a Savonius Rotor, Brace Research Institute, T. R. T10, McGill University (1964).

8. John A. Mercier, Power Generating Characteristics of Savonius Rotors, Davidson Lab., Stevens Institute of Technology, Report 1181 (1966).

9. S. K. Agrawal, Savonius Rotor as a Power Generator, MS Thesis, Department of Mechanical Engineering, Queen's University, Kingston, Ontario, Canada (1968).

10. Russell B. MacPherson, Design, Development and Testing of a Low-Head, High Efficiency Kinetic Energy Machine, Civil Engineering Department, University of Massachusetts (1972).

11. Ah Chai Lek, Experimental Investigation of the Savonius Rotor, Department of Mechanical Engineering, McGill University, Montreal, Quebec, Canada (1974).

12. J. A. C. Kentfield, "A Modified Savonius Wind Turbine with Low Velocity-Ratio Torque Characteristics," Proceedings of the University of Sherbrooke Conference on Wind Energy, University of Sherbrooke, Sherbrooke, Quebec, Canada (May 1974).

13. B. G. Newman, "Measurements on Savonius Rotor with Variable Gap," Proceedings of the University of Sherbrooke Conference on Wind Energy, University of Sherbrooke, Sherbrooke, Quebec, Canada (May 1974).

14. Charles E. Carver and Russell B. MacPherson, "Experimental Investigations of the Use of a Savonius Rotor as a Power Generation Device," Proceedings of the University of Sherbrooke Conference on Wind Energy, University of Sherbrooke, Sherbrooke, Quebec, Canada (May 1974).

15. P. N. Shankar, The Effects of Geometry and Reynolds Number on Savonius Type Rotors, National Aeronautical Laboratory, Bangalore, India, AE-TM-3-76 (February 1976).

16. B. F. Blackwell, L. V. Feltz, and R. C. Maydew, A Proposal to NSF to Sponsor a Vertical-Axis Wind Turbine Research Program, Sandia Laboratories, SAND74-0095 (July 1974).

17. B. F. Blackwell, L. V. Feltz, and E. C. Rightley, Addendum to a Proposal to NSF to Sponsor a Vertical-Axis Wind Turbine Research Program, Sandia Laboratories, SAND74-0386 (November 1974).

18. J. W. Holbrook, Low Speed Wind Tunnel Handbook, LTV Aerospace Corporation, AER-EOR-12995-B (February 1974).

19. Alan Pope and John J. Harper, Low Speed Wind Tunnel Testing, (John Wiley & Sons, Inc., New York, 1966).

20. Robert E. Wilson, Peter B. S. Lissaman, and Stel N. Walker, Aerodynamic Performance of Wind Turbines, Oregon State University (June 1976).

A-1. S. J. Kline and F. A. McClintock, "Describing Uncertainties in Single-Sample Experiments," Mechanical Engineering (January 1953), p. 3.

A-2. B. F. Blackwell, R. E. Sheldahl, and L. V. Feltz, Wind Tunnel Performance Data for the Darrieus Wind Turbine With NACA 0012 Blades, Sandia Laboratories, SAND76-0130 (May 1976), p. 51.

DISTRIBUTION:

TID-4500-R65, UC-60 (271)

R. J. Templin
Low Speed Aerodynamics Section
NRC-National Aeronautical Establishment
Ottawa 7, Ontario, Canada K1AOR6

A. Robb
Memorial Univ. of Newfoundland
Faculty of Eng. & Applied Sciences
St. John's Newfoundland
Canada A1C 5S7

H. Sevier
Rocket and Space Division
Bristol Aerospace Ltd.
P. O. Box 874
Winnipeg, Manitoba
R3C 2S4 Canada

V. A. L. Chasteau
Department of Mech. Engineering
The University of Auckland
Private Bag
Auckland, New Zealand

G. Herrera
Jet Propulsion Lab
4800 Oak Grove Drive
Pasadena, CA 91103

Langley Research Center
NASA
Hampton, VA 23665
Attn: R. Muraca, MS 317

Lewis Research Center (2)
NASA
2100 Brookpark Road
Cleveland, OH 44135
Attn: J. Savino, MS 509-201
R. L. Thomas

ERDA Headquarters (20)
Washington, DC 20545
Attn: L. Divone
Chief, Wind Energy
Conversion Branch

University of New Mexico (2)
Albuquerque, NM 87131
Attn: K. T. Feldman
Energy Research Center
V. Sloglund
ME Department

A. V. da Rosa
Stanford Electronic Laboratories
Radio Science Laboratory
Stanford, CA 94305

A. N. L. Chiu
Wind Engineering Research Digest
Spalding Hall 357
University of Hawaii
Honolulu, HI 96822

R. N. Meroney
Colorado State University
Dept. of Civil Engineering
Fort Collins, CO 80521

A. G. Vacroux
Illinois Institute of Technology
Dept. of Electrical Engineering
Chicago, IL 60616

Oklahoma State University (2)
Stillwater, OK 74074
Attn: W. L. Hughes
EE Department
D. K. McLaughlin
ME Department

Oregon State University (2)
Cornvallis, OR 97330
Attn: R. Wilson
ME Department
R. W. Thresher
ME Department

Texas Tech University (3)
Lubbock, TX 79409
Attn: K. C. Mehta, CE Dept.
J. Strickland, ME Dept.
J. Lawrence, ME Dept.

DISTRIBUTION (cont):

R. G. Watts
Tulane University
Dept. of Mechanical Engineering
New Orleans, LA 70018

Aero Engineering Department (2)
Wichita State University
Wichita, KS 67208
Attn: M. Snyder
Bill Wentz

Nevada Operations Office, ERDA (2)
P. O. Box 14100
Las Vegas, NV 89114
Attn: R. Ray, Operations
H. Mueller, ARL

Los Alamos Scientific Laboratory (7)
P. O. Box 1663
Los Alamos, NM 87544
Attn: R. R. Brownlee, J-9
J. R. Bartlit, Qu-26
J. D. Balcomb, Q-DO-T
R. G. Wagner, P-5
J. Nachamkin, T-DO-TEC
E. W. Depp, E-DO
H. Deinken, ADWP-1

ERDA/ALO (3)
Kirtland AFB East
Albuquerque, NM 87115
Attn: D. K. Knowlin
D. C. Graves
D. W. King

R. Camerero
Faculty of Applied Science
University of Sherbrooke
Sherbrooke, Quebec
Canada J1K 2R1

American Wind Energy Association
21243 Grand River
Detroit, MI 48219

E. E. Anderson
Dept. of Mechanical Engineering
South Dakota Sch. of Mines & Tech.
Rapid City, SD 57701

E. S. Takle
Climatology and Meteorology
312 Curtiss Hall
Iowa State University
Ames, IA 50011

P. B. S. Lissaman
Aeroenvironment, Inc.
660 South Arroyo Parkway
Pasadena, CA 91105

R. A. Parmelee
Department of Civil Engineering
Northwestern University
Evanston, IL 60201

J. Park
Helion
P. O. Box 4301
Sylmar, CA 91342

W. F. Foshag
Aerophysics Company
3500 Connecticut Avenue NW
Washington, DC 20008

W. L. Harris
Aero/Astro Department
MIT
Cambridge, MA 02139

K. Bergey
Aero Engineering Department
University of Oklahoma
Norman, OK 73069

J. Fischer
F. L. Smidth & Company A/S
Vigerslevalle 77
2500 Valby, Denmark

H. M Busey
DMA, Safety and Facilities A-364
ERDA Headquarters
Washington, DC 20545

P. Bailey
P. O. Box 3
Kodiak, AK 99615

DISTRIBUTION (cont):

M. E. Beecher
Solar Energy Collection
Arizona State University
University Library
Tempe, AZ 85281

U. A. Coty
Lockheed - California Co.
Box 551-63A1
Burbank, CA 91520

Lawrence Livermore Laboratory (2)
P. O. Box 808 L-340
Livermore, CA 94550
Attn: D. W. Dorn
D. Hardy

J. A. Garate
General Electric
Valley Forge Space Center
King of Prussia, PA 19406

O. Krauss
Division of Engineering Research
Michigan State University
East Lansing, MI 48823

P. Calnan
Electrical Research Associates
Cleeve Road
Leatherhead
Surrey, England

V. Nelson
Department of Physics
West Texas State University
P. O. Box 248
Canyon, TX 79016

E. Gilmore
Amarillo College
Amarillo, TX 79100

L. Liljdahl
Building 303
Agriculture Research Center
USDA
Beltsville, MD 20705

T. Wentink, Jr.
Geophysical Institute
University of Alaska
Fairbanks, AK 99701

E. J. Warchol
Bonneville Power Administration
P. O. Box 3621
Portland, OR 97225

D. Lindley
Mechanical Engineering
University of Canterbury
Christchurch, New Zealand

O. Ljungstrom
Swedish Board for Tech. Development
FACK
S-100 72 Stockholm 43, Sweden

R. Brulle
McDonnell-Douglas
P. O. Box 516
Dept. 241, Bldg. 32
St. Louis, MO 83166

R. Walters
W. Va. University
Aero Engineering
1062 Kountz Ave
Morgantown, WV 26505

A. Fritzsche
Dornier System GmbH
Postfach 1360
7990 Friedrichshafen
West Germany

P. N. Shankar
Aerodynamics Division
National Aeronautical Laboratory
Bangalore 560017
India

P. Anderson
Karstykket 42
Vvelse 3550
Slangerup, Denmark

DISTRIBUTION (cont):

O. de Vries
National Aerospace Laboratory
Anthony Fokkerweg 2
Amsterdam 1017
The Netherlands

J. P. Johnston
Mechanical Engineering
Stanford University
Stanford, CA 94305

Lt. T. Colburn
USCG R&D Center
Avory Point
Groton, CT 06340

J. Meiggs
Kaman Sciences Corp.
P. O. Box 7463
Colorado Springs, CO 80933

G. P. Hawkins
Irwin Industries
6045 West 55th Place
Arvada, CO 80002

D. Greider
Solar Central
7213 Ridge Rd.
Mechanicsburg, OH 43044

D. G. Shepherd
Sibley School of Mechanical and
Aerospace Engineering
Cornell University
Ithaca, NY 14853

B. M. Pedersen
Dept. of Fluid Mechanics
Bldg. 404,DTH
2800 Lyngby
Denmark

L. H. Soderholm
RM 213 Ag Engr.
Iowa Statue University
Ames, IA 50011

J. B. F. Scientific Corporation
2 Jewel Drive
Wilmington, MA 01887
Attn: E. E. Johanson

United Nations Environment Programme
485 Lexington Avenue
New York, NY 10017
Attn: I. H. Usmani

G. N. Monsson
Mineral Development Geologist
Dept. of Economic Planning and
Development
Barrett Building
Cheyenne, WY 82002

C. E. Anderson
Public Service Co. N. Mex.
P. O. Box 2267
Albuquerque, NM 87103

J. Lerner
State Energy Commission
Research and Development Division
1111 Howe Avenue
Sacramento, CA 95825

J. Nightingale
1735 Hunt Avenue
Richland, WA 99352

F. K. Bechtel
Assistant Professor
Department of Electrical Engineering
College of Engineering
Washington State University
Pullman, WA 99163

General Electric Co. (2)
Advanced Energy Programs
Valley Forge Space Center
P. O. Box 8661
Philadelphia, PA 19101
Attn: S. L. Macklis
J. S. Zimmerman

F. Matanzo
Dardlean Associates
15110 Frederick Road
Woodbine, MD 21797

R. Beckman
REDE
P. O. Box 212
Providence, RI 02901